

# Aspects of Nuclear Collisions of Relevance to Cosmic Ray Cascades

DISSERTATION

zur Erlangung des Grades eines Doktors  
der Naturwissenschaften

vorgelegt von

Dipl.-Phys. Stefan Roesler  
aus Leipzig

eingereicht beim Fachbereich 7  
der Universität–Gesamthochschule Siegen  
Siegen 1997

Gutachter der Dissertation:

Prof. Dr. habil. F. W. Bopp

Prof. Dr. rer. nat. habil. J. Ranft

Mitglieder der Promotionskommission:

Prof. Dr. habil. F. W. Bopp

Prof. Dr. phil. nat. habil. H. D. Dahmen

Prof. Dr. rer. nat. habil. W. Heinrich

Datum der Disputation:

28. Mai 1997

# Contents

<b>1</b>	<b>Introduction</b>	<b>1</b>
<b>2</b>	<b>Photoproduction off Nuclei</b>	<b>5</b>
2.1	Generalized Vector Dominance Model . . . . .	7
2.2	Two-Component Dual Parton Model . . . . .	9
2.3	Photon–Nucleon Interactions . . . . .	10
2.3.1	Amplitudes and Cross Sections . . . . .	11
2.3.2	Multiparticle Production . . . . .	18
2.4	Cross Sections and Nuclear Shadowing in Photon–Nucleus Collisions . . . . .	21
2.4.1	Total Photon–Nucleon Cross Sections . . . . .	22
2.4.2	Point-Like Photon Interactions . . . . .	24
2.4.3	Total Photon–Nucleus Cross Sections . . . . .	26
2.4.4	Nuclear Shadowing Behavior . . . . .	30
2.4.5	Quasi-Elastic Vector Meson Production . . . . .	34
2.5	A Model for Multiparticle Photoproduction off Nuclei . . . . .	35
2.6	Comparison of Model Predictions with Data on Particle Production . . . . .	38
2.6.1	Photon–Hadron Collisions . . . . .	38
2.6.2	Hadron–Nucleus Collisions . . . . .	39
2.6.3	Photon–Nucleus Collisions . . . . .	41
2.7	Jet Photoproduction off Nuclei at HERA-Energies . . . . .	51
<b>3</b>	<b>Aspects of Single Diffractive Interactions</b>	<b>54</b>
3.1	Single Diffractive Hadron–Nucleus Interactions . . . . .	55
3.1.1	Single Diffractive Cross Sections . . . . .	55
3.1.2	Single Diffractive Particle Production off Nuclei . . . . .	57
3.2	Single Hard Diffraction . . . . .	61
3.2.1	Hard Diffractive Processes in the Triple-Pomeron Approximation . . . . .	62
3.2.2	Parton Distributions in the Pomeron . . . . .	63
3.2.3	Particle Production . . . . .	65
<b>4</b>	<b>Projectile and Target Associated Particle Production</b>	<b>70</b>
4.1	Intranuclear Cascade . . . . .	71
4.1.1	Basic Assumptions . . . . .	71
4.1.2	The Formation Zone Intranuclear Cascade Model . . . . .	71
4.2	Calculation of Nuclear Excitation Energies . . . . .	73
4.3	Nuclear Disintegration of Spectator Prefragments . . . . .	76

4.3.1	Evaporation and High-Energy Fission . . . . .	76
4.3.2	The Fermi Break-up Model . . . . .	78
4.3.3	De-excitation by Photon Emission . . . . .	79
4.4	Comparison to Experimental Data . . . . .	81
4.4.1	Hadron–Nucleus Interactions . . . . .	81
4.4.2	Nucleus–Nucleus Interactions . . . . .	88
4.5	Applications to Cosmic Ray Cascades in the Atmosphere . . . . .	93
4.5.1	Projectile Associated Meson Production . . . . .	93
4.5.2	Residual Nuclei and De-excitation Photons from the Projectile Spectator . . . . .	96
<b>5</b>	<b>Summary and Conclusions</b>	<b>99</b>
	<b>Bibliography</b>	<b>103</b>

# Chapter 1

## Introduction

Cosmic rays enter the Earth's atmosphere with energies varying over a wide range. Their spectra approximately exhibit a power-law decrease with increasing energy [1,2]. Due to geomagnetic shielding the lower energy limit of the spectra on top of the atmosphere depends on the geographical location and direction of incidence [3,4]. The highest cosmic ray energies observed so far are of the order of  $10^{20}$  eV [5]. Below about 100 TeV cosmic rays consist mainly of hydrogen and helium nuclei. But also heavier nuclei like carbon or iron and photons contribute [1,2,6].

Depending on the interaction cross sections cosmic ray nuclei undergo inelastic collisions with air nuclei in the upper atmosphere. As a result a large number of hadrons and nuclear fragments emerge from the interaction moving approximately in the direction of the cosmic ray projectile. In subsequent collisions, decays and other energy loss processes of produced secondaries a shower of particles is built up (cosmic ray cascade, a review on this subject is given in [1]). Commonly, hadronic and electromagnetic shower components are distinguished. The latter originates from the hadronic component through electromagnetic processes initiated by secondaries (particle decays, bremsstrahlung etc.). Although existing, the production of hadrons in interactions of leptons and photons with air nuclei is much less pronounced.

Of course, not all the produced stable hadrons eventually reach the ground. Most of them are absorbed shortly after creation leading to exponentially decreasing hadron yields with increasing vertical depths in the atmosphere [7]. For a steep primary spectrum the properties of a cosmic ray shower at sea level depend strongly on those secondary particles (and the mechanisms of their production) which still possess a significant fraction of the energy of the "parent" projectile hadron or nucleus. Thus the behavior of inclusive cross sections in the forward (projectile) fragmentation region is essential.

There are many motivations for experimental and theoretical studies of cosmic ray induced showers [1]. They range from investigations of cosmic ray origin, propagation, and acceleration over fundamental particle physics to such practical applications like the estimation of the radiation level at aircraft altitudes (for the latter topic see [8,9] and references therein). Measurements are generally difficult and suffer often from technical problems like non-stationary experimental conditions in balloons and aircrafts or poor statistics due to the steep primary spectrum. For this reason theoretical studies of cosmic ray cascades are of particular importance.

Due to the complexity of physical processes in a cosmic ray cascade such theoretical

studies are mostly based on Monte Carlo (MC) formulations of models for the different interaction mechanisms [10–15]. For example, models for high-energy inelastic collisions of hadrons and nuclei can be tested against data from a wealth of measurements performed at high-energy accelerators. Collider experiments are often limited to the central rapidity region of the interaction whereas in cosmic ray cascades the forward fragmentation region is important. However, it should be expected that a model which provides a reasonable description of experimental data also gives reliable predictions for kinematic regions being experimentally less well-explored.

In this work three aspects of high-energy nuclear collisions being important in the description of cosmic ray cascades are discussed:

**1. Hadronic interactions of photons with nuclei.**

They may happen, for instance, if high-energy cosmic ray photons enter the atmosphere. In this case the calculated properties of the whole hadronic cascade depend on the description of the primary photon–nucleus interaction. As mentioned above they also constitute the link between the electromagnetic and hadronic components of a shower. Furthermore a reliable description of hadronic lepton– and photon–nucleus interactions is important for the understanding of data in cosmic ray experiments. For instance, the detected muon yields and energy spectra in deep-underground experiments have to be related to the atmospheric shower in which these muons were produced. This requires also the knowledge of the energy loss in photonuclear interactions during the passage of the muons through the rock [16].

**2. Single diffractive hadron–nucleus collisions and hard diffraction.**

There are two possibilities for a high-energy single diffractive interaction of a cosmic ray proton with an air nucleus: either the proton is quasi-elastically scattered whereas the hit air nucleus decays diffractively or, vice versa, the cosmic ray proton decays leaving a quasi-elastically deflected air nucleus. Both cases contribute to the forward fragmentation region and may influence the properties of a cosmic ray shower [17,18]. The production of particles with large transverse momenta with respect to the collision axis (particle jets) in the diffractively decaying system is called “hard diffraction”. Hard processes in diffractively decaying projectiles might also affect features of the shower.

**3. Projectile and target associated particle production.**

For example, consider the interaction of a cosmic ray iron nucleus with an air nucleus in the rest frame of the iron nucleus: In the course of the interaction a large number of hadrons (mostly nucleons, but also pions and kaons) and nuclear fragments are produced with very small energies (the so-called “projectile associated particles”). Transforming the momenta of these particles into the laboratory system of the cosmic ray interaction, i.e. the air nucleus rest frame, they appear in the very forward direction of the cascade. Their energies are comparable or even higher (due to Fermi-momenta) than the energy of the projectile nucleons. In addition, projectile associated mesons may decay giving rise, for instance, to high-energy muons. Thus it is evident that many aspects of cosmic ray cascades can only be predicted reliably if these projectile (target) associated processes are taken into account.

The choice of these three aspects of nuclear interactions of relevance to cosmic ray cascades primarily arose from a lack of MC formulations of models for these processes.

- Since the first MC description for photoproduction off nuclei by Ranft and Nelson [19], high-energy particle production in these processes has not been described in more detail on a MC basis. In view of recently obtained information, both experimentally and theoretically, on photoproduction in photon–proton and photon–nucleus collisions (recent reviews are given in [20–23]) it was tempting to combine them in a MC model. In particular, during the last years the two-component Dual Parton Model (DPM) [24] turned out to provide a successful description of many aspects of hadron–hadron [25–31], photon–hadron [32–34], photon–photon [33], hadron–nucleus and nucleus–nucleus [35,31] collisions. It allows to calculate cross sections and particle production in a consistent way. As discussed in this work, it has now also been extended to photon–nucleus interactions [36,37].
- Concerning single diffractive hadron–nucleus collisions only a few experimental data are presently available [38,39]. Theoretically these processes have been studied by several authors [40–46]. However, no detailed MC formulation as needed for cosmic ray cascade calculations was available. Again, since the two-component DPM has recently been shown to give a reliable description of single diffractive hadron–hadron collisions [28,47] it was chosen for the study [48,49] to be described further below.
- There are several models for high-energy hadron–nucleus and nucleus–nucleus collisions used in the description of cosmic ray cascades (for instance the models discussed in Refs. [12,50–53,14,31,15]). However, they either do not treat projectile and target associated particle production at all or, with respect to nuclear spectator fragmentation, in a very approximate manner only. Therefore, in this work the formation zone intranuclear cascade model is extended from hadron–nucleus [54,55] to nucleus–nucleus collisions and excitation energies of spectator prefragments are calculated [56,57]. This extension together with models for evaporation processes as well as spectator fission and fragmentation are implemented into the two-component DPM formulations of Refs. [31,37] and are applied to cosmic ray cascades calculations for the first time [56–58].

It should be emphasized that the study of these three aspects of nuclear collisions is not only of interest for cosmic ray interactions in the atmosphere. In many other applications the discussed models may help to understand experimental observations or in designing future accelerators.

For example, the experimental study of photon–nucleus collisions using the HERA-collider at DESY is presently under discussion [59]. In those experiments soft multiparticle photoproduction off nuclei (i.e. the production of particles with low transverse momenta) will constitute the main background process and has to be considered in the extraction of information on jet production. Since the photon–nucleus interaction model proposed in this work contains a description of both, soft as well as hard photoproduction, its application to these interactions might be interesting. Furthermore background radiation studies for a future muon collider at Fermilab [60,61] require a precise knowledge of photon–nucleus interactions since hadronic interactions of high-energy muons with nuclei

proceed mainly via photons emitted by the muons. Again, the discussed model may also provide valuable information for these studies.

A detailed description of projectile associated particle production is necessary in background radiation and beam dump studies for heavy-ion accelerators like the LHC at CERN or the RHIC at BNL. Calculations of radiation fields include estimations of deeply penetrating particle cascades in shielding materials, a problem similar to the calculation of cosmic ray cascades in the atmosphere. Finally, predictions on nuclear fragment production are often important for heavy-ion experiments in order to simulate the performance of detector components in the forward or backward directions like Zero Degree Calorimeters.

The thesis is organized as follows. In Chapter 2 the description of photoproduction off nuclei in the framework of the two-component DPM is discussed. The first part of this chapter covers the basic ingredients used for its extension from photon-hadron and hadron-nucleus to photon-nucleus collisions. In particular, it gives a short account on the Generalized Vector Dominance Model and sketches the fundamental ideas underlying the two-component DPM. Furthermore the treatment of photon-nucleon interactions is briefly summarized. The second part includes a detailed discussion of results on photon-nucleus cross sections and the high-energy nuclear shadowing behavior as well as the application of the two-component DPM to multiparticle photoproduction off nuclei. Model results on particle production in collisions of real and weakly virtual photons with nuclei are compared to data and predictions for jet photoproduction off nuclei at HERA-energies are presented.

Chapter 3 describes the treatment of single diffractive hadron-nucleus collisions. Both, cross sections and particle production are discussed and compared to experimental data. In addition, this chapter details a possible treatment of hard diffractive processes including a discussion on parton distributions in the pomeron and hard diffractive particle production.

Projectile and target associated particle production is subject of Chapter 4. It starts with a summary of the formation zone intranuclear cascade model for hadron-nucleus interactions and describes its extension to nucleus-nucleus collisions. Excitation energies of prefragments are calculated which serve as input for a description of their further disintegration. This disintegration is treated by applying MC models for evaporation processes, high-energy fission, and the fragmentation of light prefragments. In a detailed comparison with data it is shown that the discussed models provide an adequate description of target associated particle production. Furthermore applications to the description of cosmic ray cascades are discussed. Finally, in Chapter 5 results are summarized.

## Chapter 2

# Photoproduction off Nuclei

In this chapter the description of interactions of real and weakly virtual photons with nuclei is discussed in the framework of the two-component DPM. In particular, the *photoproduction limit*

$$x \longrightarrow 0 \quad \text{and} \quad Q^2 \longrightarrow 0 \quad \text{at fixed } \nu \quad (2.1)$$

is considered. Here  $Q^2$ ,  $\nu$  and  $x$  denote the virtuality of a photon, its energy in the nucleus rest frame and the Bjorken scaling variable ( $x = Q^2/(2m_N\nu)$ , with  $m_N$  being the nucleon mass), respectively. In order to illustrate the validity range of the model, a common classification scheme of photon–nucleus collisions is sketched first. This classification is based on different interaction mechanisms which might be responsible for the characteristic behavior of the ratio of the structure functions of nucleus  $A$  and of deuterium  $R_A = F_2^A/F_2^D$ .

As it has been first demonstrated by the EMC-Collaboration [62], the structure function of a bound nucleon differs from that of a free nucleon due to the nuclear environment. The whole kinematic region is commonly subdivided into different  $x$ -ranges (for example see [22,63] and references therein, see also Fig. 2.1):

- $x \leq 0.05$  ( $R_A < 1$ ): *Shadowing region*. One possible explanation for the behavior of  $R_A$  in this region is based on the assumption that the photon fluctuates from its point-like, “bare photon” state into a superposition of vector mesons which then interact strongly with nucleons. The multiple scattering process of the hadronic fluctuations with target nucleons is described in the framework of the Gribov–Glauber approximation [64–66].
- $0.1 \leq x \leq 0.2$  ( $R_A > 1$ ): *Anti-shadowing region*. Anti-shadowing can be described, for instance, in the framework of a Regge-model [67]. There, the enhancement is understood as due to the phase of secondary Regge-trajectories.
- $0.3 \leq x \leq 0.8$  ( $R_A < 1$ ): *EMC-effect*. This effect indicates that the valence quark distribution in bound nucleons is depleted with respect to that in a free nucleon. Several models have been proposed to explain this effect, both from a hadronic and a partonic point of view. For instance, the depletion of the valence quark distribution can be caused by an excess of virtual pions in the nucleus carrying a fraction of the nucleon momentum and, therefore, of the valence quarks. Other attempts explain

the EMC-effect by an increased quark confinement region or in terms of quark clusters.

- $0.8 \leq x \leq 1$  ( $R_A > 1$ ): *Fermi-motion*. Experimentally, the Bjorken- $x$  variable is determined assuming the nucleons to be at rest. The measured structure function is the convolution of the bare nucleon structure function with the Fermi-momentum distribution leading to an increase of the valence parton density in this region.
- $1 < x \leq A$  ( $R_A \gg 1$ ): *Cumulative effect*. It appears in rather rare events and can be ascribed to collective effects.

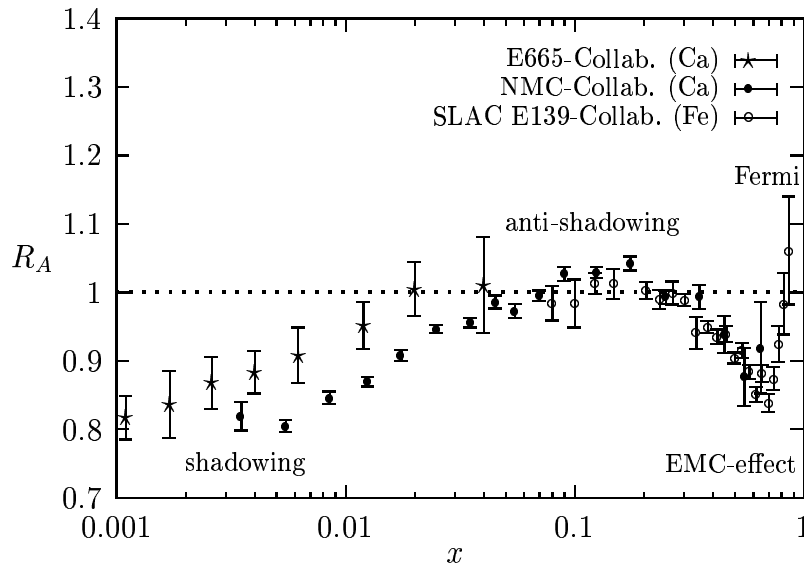


Figure 2.1: Ratio of the structure functions of calcium [68,69] and iron [70] to the deuterium structure function.

The two-component DPM model for high-energy photon–nucleus collisions discussed in this chapter is limited to the description of interactions in the shadowing region (including the photoproduction limit) which satisfy the following kinematic bounds

$$\nu \gtrsim 10 \text{ GeV}, \quad Q^2 \lesssim 9 \text{ GeV}^2 \quad \text{and} \quad Q^2 \ll 2m_N \nu. \quad (2.2)$$

It covers the majority of high-energy hadronic interactions induced by photons in particle cascades in matter (for instance the atmosphere) and is therefore well suited to be applied in the simulation of such cascades.

The organization of this chapter follows from the logical sequence in the development of the model. Whereas the basic theoretical ingredients are collected throughout Sections 2.1 to 2.3, the application to photon–nucleus collisions and the main results of this study are presented in Sections 2.4–2.7.

The photon and its hadronic properties (irrespective of the nature of the target) are subject to Sec. 2.1 where some aspects of the Generalized Vector Dominance Model are recalled. The main assumption is that the photon interacts with a certain probability via quark-antiquark fluctuations. Sec. 2.2 summarizes the basic ideas and phenomenological concepts which underlie the understanding of hadronic collisions within the two-component DPM in general. The description of photon–nucleon interactions is discussed in Sec. 2.3. Here, the main ingredients of the model and the basic formulas describing photoproduction off nucleons are collected. In particular, the calculation of total

photon–nucleon cross sections is summarized which are used to calculate cross sections for photon–nucleus interactions. They are obtained in Sec. 2.4 on the basis of the Gribov–Glauber approximation and are compared to experimental data. Particular emphasis is put on modifications of the Gribov–Glauber formalism in order to take point-like photon interactions into account. Furthermore the influence of point-like processes on the behavior of total cross sections and nuclear shadowing at high energies is studied. Sec. 2.5 details the description of multiparticle photoproduction within the two-component DPM and gives a short account on the implementation in the event generator DTUNUC 2.0. In Sec. 2.6 model predictions are compared to data on particle production in photon–hadron, hadron–nucleus and photon–nucleus collisions. In addition, the nuclear dependence of particle production is discussed. Finally, jet photoproduction off nuclei is subject to Sec. 2.7 where predictions for HERA-energies are given.

Results discussed throughout this chapter are published in [36,37].

## 2.1 Generalized Vector Dominance Model

It is a well-known feature of high-energy photon induced interactions that they bear a remarkable resemblance to purely hadronic interactions. Apart from a scale factor of the order of the fine-structure constant  $\alpha_{\text{em}}$  in the cross section, particle production processes show, for instance, almost the same energy and angular dependences. The simplest approach explaining these similarities is based on the assumption that the real or virtual photon fluctuates with a probability of the order of  $\alpha_{\text{em}}$  into one of the three vector mesons  $\rho^0$ ,  $\omega$  and  $\phi$  which subsequently undergoes a hadronic interaction (*Vector Dominance Model*, see [71] and references therein). This fact can be expressed in terms of the following relation for the amplitude of the photon–nucleon scattering process ( $s$  and  $t$  being the Mandelstam variables of this process)

$$A_{\gamma N \rightarrow X}(s, t, Q^2) = \sum_{V=\rho, \omega, \phi} \frac{e}{f_V} \frac{m_V^2}{m_V^2 + Q^2 - i\Gamma_V m_V} A_{VN \rightarrow X}(s, t) \quad (2.3)$$

where all the dependence on the photon virtuality  $Q^2$  is contained in the vector meson propagators. Here  $m_V$ ,  $\Gamma_V$  and  $e/f_V$  are the mass, decay width and coupling constant of the vector meson  $V$ , respectively.

However, it is already obvious from Eq.(2.3) that, as soon as for instance the photon-virtuality increases, vector mesons or, more generally, hadronic quark-antiquark fluctuations with higher masses have to be taken into consideration. This approach is called *Generalized Vector Dominance Model* (GVDM). Comprehensive reviews of the GVDM are given in [72,73]. Here, only a few aspects being relevant to further discussions are repeated.

Denoting the photon momentum in the rest system of the target with  $\vec{k}$ , the difference between the photon energy ( $\nu = \sqrt{-Q^2 + k^2}$ ) and the energy of the hadronic fluctuation ( $E = \sqrt{M^2 + k^2}$ ) becomes

$$\Delta E = E - \nu \approx \frac{M^2 + Q^2}{2\nu} . \quad (2.4)$$

The hadronic fluctuation will then extend over a distance (the ‘‘coherence length’’)

$$d(M^2, Q^2) = \Delta t \approx \frac{1}{\Delta E} \approx \frac{2\nu}{M^2 + Q^2} = \frac{1}{m_N x} \frac{1}{1 + M^2/Q^2}. \quad (2.5)$$

This relation implies that (i) the coherence length does not depend on the target, (ii) it increases linearly with the photon energy and (iii) at fixed photon energy it may become small for high-mass fluctuations or large photon virtualities. In order to guarantee the GVDM picture of the scattering process the coherence length has to exceed the typical interaction length (for nucleons  $r_N \approx 1$  fm).

Within the GVDM the virtual photon–nucleon cross section for transversely polarized photons reads

$$\sigma_{\gamma^* N}^{(T)}(s, Q^2) = \sum_i \left( \frac{e}{f_{V_i}} \right)^2 \left( \frac{M_{V_i}^2}{M_{V_i}^2 + Q^2} \right)^2 \sigma_{V_i N}^{(T)}(s, Q^2, M_{V_i}^2) \quad (2.6)$$

where the sum extends now over the vector mesons  $V_1, V_2, \dots, V_L$ . In the cross section (2.6) the possibility of interference between different vector states ( $VN \rightarrow V'N$  with  $V \neq V'$ ) is excluded (*diagonal* GVDM), whereas *off-diagonal* models include these interference terms.

Alternatively, the sum in Eq.(2.6) can be turned into an integral over the mass of the hadronic fluctuations ( $q\bar{q}$ -states). The total photon–nucleon cross section is defined by the nucleon structure function  $F_2^N$  using the following convention [74]

$$\sigma_{\gamma^* N}(s, Q^2) = \frac{4\pi^2 \alpha_{\text{em}}}{Q^2(1-x)} F_2^N(x, Q^2) \quad (2.7)$$

and can be expressed by a spectral relation of the form [75,23]

$$\sigma_{\gamma^* N}(s, Q^2) = 4\pi \alpha_{\text{em}} \int_{M_0^2}^{M_1^2} dM^2 D(M^2) \left( \frac{M^2}{M^2 + Q^2} \right)^2 \left( 1 + \epsilon \frac{Q^2}{M^2} \right) \sigma_{VN}(s, Q^2, M^2). \quad (2.8)$$

The factor  $D(M^2)$  incorporates the density of  $q\bar{q}$ -states per unit mass-squared interval and the mass-dependence of the coupling ( $f^2(M^2) \sim M^2$ ):

$$D(M^2) = \frac{R_{e^+e^-}(M^2)}{12\pi^2 M^2}, \quad R_{e^+e^-}(M^2) = \frac{\sigma_{e^+e^- \rightarrow \text{hadrons}}(M^2)}{\sigma_{e^+e^- \rightarrow \mu^+\mu^-}(M^2)} \approx 3 \sum_f e_f^2. \quad (2.9)$$

The sum involves the squared quark charges of all quark flavors  $f$  being energetically accessible. The quantity  $\sigma_{VN}$  is the effective cross section for the interaction of a  $q\bar{q}$ -state of mass  $M$  with a nucleon. With increasing  $M$  the virtuality of the quark and antiquark of the  $q\bar{q}$ -state increases. As a consequence the transverse size of the hadronic fluctuation and, hence,  $\sigma_{VN}$  decreases approximately like  $1/M^2$  at large  $M^2$  [73,76] (see also Sec. 2.4.1). The different  $Q^2$ -behavior of the cross sections for the scattering of transversely and longitudinally polarized photons accounts for the term  $\epsilon Q^2/M^2$  in Eq.(2.8).  $\epsilon$  is the ratio between the photon fluxes of longitudinal and transverse polarization. The lower integration limit  $M_0^2$  corresponds to the kinematical threshold. Alternatively, the contributions from  $\rho^0$ ,  $\omega$  and  $\phi$  could also be added as separate terms to the mass-continuum. In this case the integration would start at  $m_\phi^2$  [23,77]. The upper limit  $M_1^2$  is usually set at a value of the order of  $s$ . However, its actual value has practically no influence on the results at low and moderate  $Q^2$  since high  $M^2$ -values are strongly suppressed in this case.

## 2.2 Two-Component Dual Parton Model

At present Quantum Chromodynamics (QCD) appears as the accepted theory of strong interactions. Classically, it is a scale invariant theory characterized by a dimensionless coupling constant. However, due to renormalization scale invariance is broken and the coupling becomes scale-dependent. In particular, it increases with the characteristic length scale of the interaction.

Most of the particles produced in high-energy collisions have small transverse momenta with respect to the collision axis (soft processes). Soft hadron dynamics involves length scales of about 1 fm corresponding to coupling constants  $g_s$  of the order of unity. Hence perturbative QCD is not applicable to soft physics.

A new method of expansion has to be found. Generalizing QCD from a gauge group  $SU(3)$  to  $SU(N_c)$  (with  $N_c$  being the number of colors) it can be shown that in the large  $N_c$ -limit  $1/N_c$  may serve as an alternative (artificial) expansion parameter [78]. Phenomenologically, it is more appropriate to consider a limit where quarks and gluons are treated similarly. Consequently, also the number of flavors  $N_f$  should be allowed to become large (*Veneziano limit*:  $N_c \rightarrow \infty$ ,  $N_c/N_f = \text{const}$ ,  $g_s^2 N_c^2 = \text{const}$ ) [79,80]. Each diagram of the  $SU(N_c)$  gauge theory constructed in this way can be characterized by a two-dimensional surface. Regrouping the Feynman expansion according to surface topologies one obtains an expansion in topologies where subsequent terms are suppressed by an additional factor  $1/N_c^2$ . Correspondingly, for  $2 \rightarrow 2$  scattering amplitudes the leading term has a planar topology and the second term the topology of a cylinder. The topological expansion combined with constraints of unitarity and duality is called *Dual Topological Unitarization* (DTU) scheme [81–83].

Another, completely different approach to describe scattering processes originates in the work of Regge [84]. He demonstrated that for a wide class of potentials the non-relativistic potential scattering amplitude has poles in the complex angular momentum plane which characterize the scattering process. In the language of high-energy interactions this observation can be formulated in the following way (a comprehensive review is given in [85]). To be definite, let  $AB \rightarrow A'B'$  be the scattering process of particles  $A$  and  $B$  in the  $s$ -channel. Then, assuming such general properties of the scattering amplitude like analyticity (in the Mandelstam variables  $s$ ,  $t$  and  $u$ ), it can be shown that the high-energy behavior of the amplitude in the  $s$ -channel is governed by intermediate resonances (i.e. pole contributions) in the  $t$ -channel  $A\bar{A}' \rightarrow \bar{B}B'$ . Furthermore it is possible to group these resonances together to form so-called Regge-trajectories, or reggeons (with definite quantum numbers according to the resonances belonging to a trajectory). Thus, within Regge theory the  $s$ -channel scattering process is described by the exchange of reggeons. The reggeon determining the  $s$ -dependence of the amplitude in the limit of high energies is called pomeron. A systematic attempt to impose unitarity on the scattering amplitude is a multiple scattering approach (i.e. the exchange of multiple reggeons) known as *Gribov's reggeon field theory* (RFT) [86,87]. It provides a general method for the evaluation of diagrams involving multiple reggeon exchanges.

As it has been shown in [88] there exists a one-to-one correspondence between the terms in the topological expansion of QCD and the diagrams of RFT. This correspondence allows, for instance, to estimate the relative sizes of the different terms in the topological expansion by means of perturbative RFT. On this basis, the planar topology is associated

with reggeon exchange and the cylindrical topology with pomeron exchange (see Fig. 2.2). Although reggeon exchange corresponds to the leading term in the topological expansion,

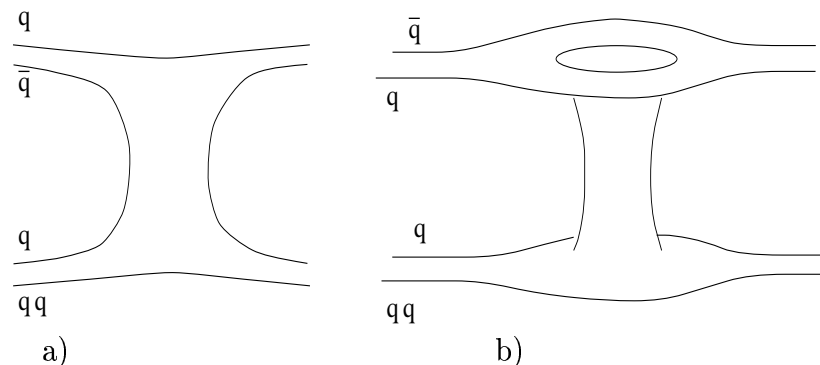


Figure 2.2: a) Graph with planar topology (reggeon exchange), b) graph with cylindrical topology (pomeron exchange).

it depends on  $s$  like  $1/\sqrt{s}$ . Therefore the dominant contribution to the elastic scattering amplitude at high energies comes from pomeron exchange.

The DPM (a review is given in [24]) incorporates these approaches and provides a complete, phenomenological description of soft scattering processes. In particular:

- It receives its basic ideas and motivation from the DTU scheme. The relative weights of each term in the topological expansion are obtained from perturbative RFT in a suitable approximate parametrization. Perturbative RFT allows to compute the cross section for a given number  $k$  of inelastic collisions and an arbitrary number of elastic rescatterings which corresponds to  $k$  “cut” pomerons (see Sec. 2.3.2). Its correspondence to a diagram in the topological expansion essentially determines the topology of such an inelastic event: a cut pomeron is associated with two “chains” of hadrons.
- It incorporates the partonic structure of hadrons. Each event (for instance an event with  $k$  cut pomerons) is treated in two steps: (i) separation of color in the collision (a baryon/meson is assumed to consist of a valence quark and a valence diquark/antiquark and a certain number of sea  $q\bar{q}$ -pairs) and (ii) fragmentation of colored objects into chains of hadrons (often called “hadronization”). As an example, for an event with  $k$  cut pomerons one would end up with  $2k$  chains of hadrons.

A formulation of the DPM which distinguishes particle production with low and high transverse momentum (the first described by Regge-arguments, the latter within the QCD-improved Parton Model) is usually called two-component DPM [25–32].

## 2.3 Photon–Nucleon Interactions

A model for multiparticle photoproduction off nuclei which is based on the Gribov–Glauber approximation [64–66] describes the scattering process in terms of individual interactions of the photon or its hadronic fluctuations with weakly bound nucleons. Therefore the description of photon–nucleon interactions within the two-component DPM constitutes the basic ingredient of an extension of the model to photon–nucleus collisions. In fact, at not too high energies and photon virtualities above  $2 \text{ GeV}^2$  the photon mostly

interacts with only one or two nucleons. Thus, many characteristic features of photon–nucleon interactions can be expected to be present also in photon–nucleus interactions, although modified by the nuclear environment.

In this section, a short account on the two-component DPM for photon–nucleon collisions as implemented in the MC event generator PHOJET [32,33] is given. Instead of discussing all aspects or focusing on calculational details, only the main ideas and formulas being important for the description of photoproduction off nuclei are summarized. Detailed discussions can be found in Refs. [32–34].

### 2.3.1 Amplitudes and Cross Sections

The physical photon state is approximated as a superposition of a *bare photon* and of virtual *hadronic states*

$$|\gamma\rangle = \sqrt{Z_3}|\gamma_{\text{bare}}\rangle + |\gamma_{\text{had}}\rangle. \quad (2.10)$$

The latter correspond to the Generalized Vector Dominance picture sketched in Sec. 2.1 and possess photon quantum numbers. In general, a wide range of masses has to be treated (see Eq.(2.8)). However, for the description of photon–hadron interactions within the two-component DPM it turned out to be reasonable to consider only two “generic” hadronic states [32]

$$|\gamma_{\text{had}}\rangle = \frac{e}{f_{q\bar{q}}}|q\bar{q}\rangle + \frac{e}{f_{q\bar{q}^*}}|q\bar{q}^*\rangle. \quad (2.11)$$

The  $q\bar{q}$ -state combines the  $\rho^0$ ,  $\omega$  and  $\phi$  vector mesons and  $\pi^+\pi^-$ -states up to the  $\phi$ -mass. Resonances with higher masses ( $\rho'$ ,  $\omega'$ ,  $\rho''$ , ...) are lumped together as  $q\bar{q}^*$ -state. Thus, the normalization constant  $Z_3$  follows from the two VDM couplings of the generic states to the photon as  $Z_3 = 1 - e^2/f_{q\bar{q}}^2 - e^2/f_{q\bar{q}^*}^2$ .

Since the bare photon enters the scattering process as a gauge boson, its interactions are classified as **direct** processes. In contrast, the hadronic part of the physical photon state interacts via hadronic fluctuations. Therefore these interactions are frequently called **resolved** processes. Denoting the corresponding amplitudes in impact parameter ( $\vec{B}$ ) space with  $a_{\gamma N}^{\text{dir}}$  and  $a_{\gamma N}^{\text{res}}$  the total and elastic real photon–nucleon cross sections and the cross section for quasi-elastic vector meson production are obtained from

$$\sigma_{\gamma N}^{\text{tot}}(s) = 4 \int d^2\vec{B} \Im m \left\{ Z_3 a_{\gamma N}^{\text{dir}}(s, \vec{B}) + \langle \gamma_{\text{had}}, N | a_{\gamma N}^{\text{res}}(s, \vec{B}) | \gamma_{\text{had}}, N \rangle \right\}, \quad (2.12)$$

$$\sigma_{\gamma N}^{\text{el}}(s) = 4 \int d^2\vec{B} \left| Z_3 a_{\gamma N}^{\text{dir}}(s, \vec{B}) + \langle \gamma_{\text{had}}, N | a_{\gamma N}^{\text{res}}(s, \vec{B}) | \gamma_{\text{had}}, N \rangle \right|^2, \quad (2.13)$$

$$\sigma_{\gamma N}^{\text{qel}}(s) = 4 \int d^2\vec{B} \left| \langle q\bar{q}, N | a_{\gamma N}^{\text{res}}(s, \vec{B}) | \gamma_{\text{had}}, N \rangle \right|^2. \quad (2.14)$$

In the following the calculation of the amplitudes  $a_{\gamma N}^{\text{res}}$  and  $a_{\gamma N}^{\text{dir}}$  is briefly summarized.

#### Resolved processes

The interactions of the quark-antiquark fluctuations of the photon are described within the perturbative reggeon calculus in terms of multiple pomeron exchange. The exchange of more than one pomeron is required to ensure  $s$ -channel unitarity of the amplitude.

The scattering amplitude  $a_{\gamma N}^{\text{res}}$  is approximated by summing up  $n$ -pomeron exchange amplitudes  $a^{(n)}$  and can be conveniently written introducing an eikonal function  $\chi$

$$a_{\gamma N}^{\text{res}}(s, \vec{B}) = \sum_{n=1}^{\infty} a^{(n)}(s, \vec{B}) = \frac{i}{2} \left( 1 - e^{-\chi(s, \vec{B})} \right). \quad (2.15)$$

It is possible to express the eikonal function in terms of Born-graph impact parameter amplitudes. Therefore in the following the Born-graph amplitudes are discussed.

A single pomeron exchange graph can be related to graphs with multiperipheral kinematics [87]. The calculation of cross sections involves the sum over all possible intermediate states of such graphs and the integration over their momenta. In order to be able to apply perturbative QCD the integration is commonly split into two parts: one part where at least one parton has a sufficiently large transverse momentum  $q_{\perp}$  satisfying the condition  $q_{\perp} \geq p_{\perp}^{\text{cut}} \gg \Lambda_{\text{QCD}}$  and a second part including all other integrations. This results in an artificial subdivision into those graphs where at least one large transverse momentum is involved (*hard* processes) and into graphs containing only low transverse momenta (*soft* processes). In the following the soft and hard parts of a one-pomeron exchange are called “soft pomeron” and “hard pomeron”. Their eikonal functions are denoted by  $\chi_{\text{S}}$  and  $\chi_{\text{H}}$ .

Within perturbative RFT, the evaluation of  $n$ -pomeron exchange diagrams involves the integration over  $2(n-1)$  masses of intermediate states, i.e. states between two exchanged pomerons (see for example the two-pomeron exchange graph in Fig. 2.3). In the

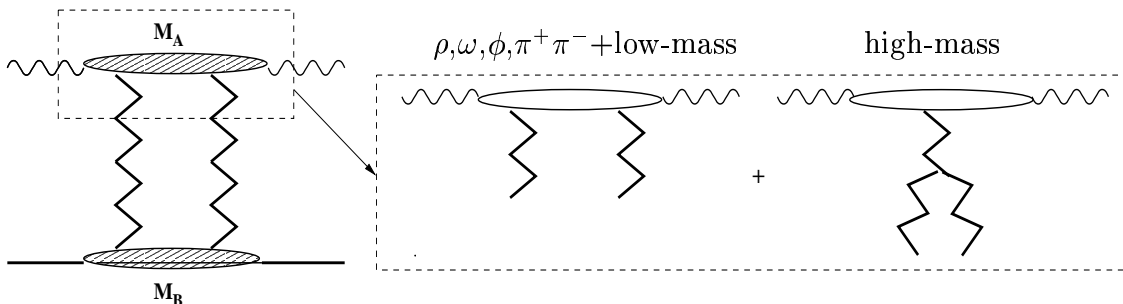


Figure 2.3: Two-pomeron exchange graph. The calculation of its contribution to the scattering amplitude involves the integration over the masses  $M_A$  and  $M_B$ . The subdivision into an elastic+low-mass component and a high-mass component is shown for the upper vertex.

approximation discussed here, these intermediate states are subdivided into (Fig. 2.3)

- *elastic* intermediate states which correspond to the generic state  $|q\bar{q}\rangle$ , i.e.  $\rho$ ,  $\omega$ ,  $\phi$  and  $\pi^+\pi^-$ -states with  $m_{\pi^+\pi^-} \leq m_{\phi}$ ,
- *low-mass* intermediate states with masses  $M$  ( $m_{\phi}^2 < M^2 \leq M_L^2$ ,  $M_L^2 = 5 \text{ GeV}^2$ ) which correspond to the generic state  $|q\bar{q}^*\rangle$ ,
- *high-mass* intermediate states with masses  $M$  ( $M_L^2 < M^2 \leq M_U^2$ ,  $M_U^2 = 0.4s$ ).

Elastic and low-mass intermediate states are taken into account within a two-channel eikonal formalism (see further below). High-mass intermediate states are treated by explicitly considering pomeron exchange graphs which involve the coupling of three pomerons

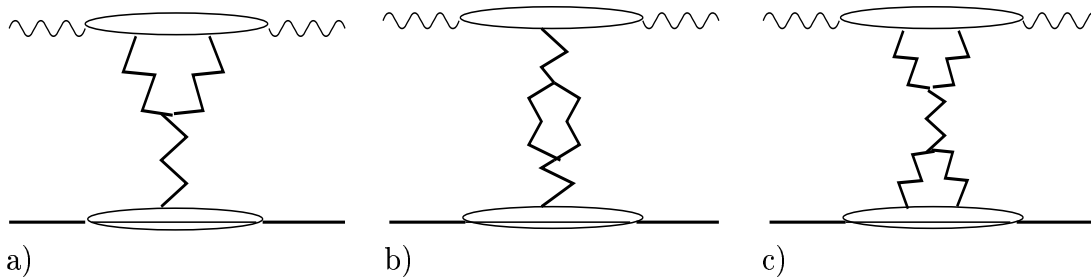


Figure 2.4: a) *Triple-pomeron graph*, b) *loop-pomeron graph* and c) *double-pomeron graph*.

(so-called enhanced graphs). In particular, these are the triple-pomeron (TP) and loop-pomeron (LP) graphs (see Fig. 2.4a,b). In order to describe central diffraction the double-pomeron graph (Fig. 2.4c) is taken into account additionally. This graph can be considered as an iterated TP graph. The eikonal functions associated with these three enhanced graphs are  $\chi_{\text{TP}}$ ,  $\chi_{\text{LP}}$  and  $\chi_{\text{DP}}$ .

Consequently, the function  $\chi$  entering the expression for the amplitude of resolved processes (Eq.(2.15)) is composed of the eikonal functions of the different contributions

$$\chi(s, \vec{B}) = \chi_{\text{S}}(s, \vec{B}) + \chi_{\text{H}}(s, \vec{B}) + \chi_{\text{TP}}(s, \vec{B}) + \chi_{\text{LP}}(s, \vec{B}) + \chi_{\text{DP}}(s, \vec{B}) . \quad (2.16)$$

Assuming that only elastic intermediate states are important, the  $n$ -pomeron-particle coupling function can be written as a product of one-pomeron-particle couplings. Then it follows from Eq.(2.15) that the eikonal functions  $\chi_j$  are related to the Born-graph amplitudes  $a_j$  by

$$\chi_j(s, \vec{B}) = -2ia_j(s, \vec{B}), \quad j = \text{S, H, TP, LP, DP} . \quad (2.17)$$

Furthermore all Born-graph impact parameter amplitudes  $a_j(s, \vec{B})$  are related to the corresponding amplitudes in momentum space  $A_j(s, t)$  by Fourier-transformation ( $t \approx -\vec{q}_{\perp}^2$ ):

$$a_j(s, \vec{B}) = \frac{1}{4s} \int \frac{d^2\vec{q}_{\perp}}{(2\pi)^2} A_j(s, t) e^{-i\vec{q}_{\perp} \vec{B}} . \quad (2.18)$$

Inspired by experimental observations, an exponential  $t$ -dependence of the Born-graph amplitudes  $A_j$  is assumed and the real parts are neglected

$$A_j(s, t) = is \sigma_j(s) e^{b_j(s)t} \quad (2.19)$$

where  $\sigma_j$  and  $b_j$  are the Born-graph cross sections and slopes. This leads, together with Eq.(2.18), to impact parameter amplitudes (and eikonal functions) with Gaussian shape

$$a_j(s, \vec{B}) = \frac{i}{2} \chi_j(s, \vec{B}) = i \frac{\sigma_j(s)}{16\pi b_j(s)} e^{-\vec{B}^2/(4b_j(s))} . \quad (2.20)$$

In the following the Born-graph cross sections  $\sigma_j$  and slopes  $b_j$  are discussed. Low-mass excited intermediate states of the colliding particles between different pomeron exchanges are omitted for simplicity. A generalization will be given separately at the end of this section.

Soft non-diffractive processes: At high energies soft non-diffractive processes are well described within Regge theory by the exchange of supercritical soft pomerons ( $\mathbb{P}$ ). The amplitude corresponding to the exchange of a supercritical soft pomeron can be written in momentum space as a product of  $t$ -dependent pomeron-particle couplings together with a power-law dependence on the scattering energy

$$A_S^{\mathbb{P}}(s, t) = i s_0 g_{q\bar{q}\mathbb{P}}(t) g_{N\mathbb{P}}(t) \left( \frac{s}{s_0} \right)^{\alpha_{\mathbb{P}}(t)}. \quad (2.21)$$

Here,  $\alpha_{\mathbb{P}}(t) = 1 + \Delta_{\mathbb{P}} + \alpha'_{\mathbb{P}}(0)t$  is the pomeron trajectory and  $s_0 = 1 \text{ GeV}^2$ . The quantity  $\alpha_{\mathbb{P}}(0)$  is usually called ‘‘intercept’’. The terminology ‘‘supercritical’’ means that  $\Delta_{\mathbb{P}} > 0$  (in contrast to pomerons with  $\Delta_{\mathbb{P}} = 0$  which are called ‘‘critical’’) and will be omitted for simplicity hereafter. For the couplings an exponential  $t$ -dependence is assumed

$$g_{k\mathbb{P}}(t) = g_{k\mathbb{P}}^0 e^{b_{k\mathbb{P}}^0 t/2}, \quad k = q\bar{q}, N. \quad (2.22)$$

According to Eq.(2.19) one may write

$$A_S^{\mathbb{P}}(s, t) = i s \sigma_S^{\mathbb{P}}(s) e^{b_S^{\mathbb{P}}(s)t} \quad (2.23)$$

with

$$\sigma_S^{\mathbb{P}}(s) = g_{q\bar{q}\mathbb{P}}^0 g_{N\mathbb{P}}^0 \left( \frac{s}{s_0} \right)^{\Delta_{\mathbb{P}}}, \quad b_S^{\mathbb{P}}(s) = \frac{1}{2} \left( b_{q\bar{q}\mathbb{P}}^0 + b_{N\mathbb{P}}^0 + 2\alpha'_{\mathbb{P}}(0) \ln \left( \frac{s}{s_0} \right) \right). \quad (2.24)$$

Inserting the expressions (2.24) into Eq.(2.20) the eikonal function for soft pomeron exchange  $\chi_S^{\mathbb{P}}$  follows directly. At low energies reggeon ( $\mathbb{R}$ ) exchange dominates the description of soft processes. In analogy to  $\chi_S^{\mathbb{P}}$  the eikonal function  $\chi_S^{\mathbb{R}}$  is calculated from

$$\sigma_S^{\mathbb{R}}(s) = g_{q\bar{q}\mathbb{R}}^0 g_{h\mathbb{R}}^0 \left( \frac{s}{s_0} \right)^{\Delta_{\mathbb{R}}}, \quad b_S^{\mathbb{R}}(s) = \frac{1}{2} \left( b_{q\bar{q}\mathbb{R}}^0 + b_{h\mathbb{R}}^0 + 2\alpha'_{\mathbb{R}}(0) \ln \left( \frac{s}{s_0} \right) \right). \quad (2.25)$$

Finally, the eikonal function for soft non-diffractive processes is defined as the sum of both contributions

$$\chi_S(s, \vec{B}) = \chi_S^{\mathbb{P}}(s, \vec{B}) + \chi_S^{\mathbb{R}}(s, \vec{B}). \quad (2.26)$$

Hard resolved processes: For the estimation of the cross section of hard resolved processes the QCD-improved Parton Model can be employed:

$$\sigma_H(s, p_{\perp}^{\text{cut}}) = \int dx_1 dx_2 d\hat{t} \sum_{i,j,k,l} \frac{1}{1 + \delta_{k,l}} f_{i|q\bar{q}}(x_1, \mu^2) f_{j|N}(x_2, \mu^2) \frac{d\hat{\sigma}_{i,j \rightarrow k,l}}{d\hat{t}} \Theta(p_{\perp} - p_{\perp}^{\text{cut}}). \quad (2.27)$$

$f_{i|q\bar{q}}$  and  $f_{j|N}$  denote the parton distribution functions (PDFs) for partons of type  $i$  and  $j$  of the  $q\bar{q}$ -state and the nucleon, respectively. The Mandelstam variables  $\hat{s}$  and  $\hat{t}$  characterize the partonic subprocess  $i, j \rightarrow k, l$ . The short distance cross section  $\hat{\sigma}_{i,j \rightarrow k,l}$  is calculated within lowest order perturbative QCD. The sum runs over all possible parton configurations  $(i, j, k, l)$ . The momentum transfer in the hard subprocess approximately determines the factorization scale  $\mu^2$  which is taken to be  $\mu^2 = p_{\perp}^2/4$ . The transverse momentum cutoff  $p_{\perp}^{\text{cut}}$  restricts the integration to the validity range of perturbation theory.

The PDFs of the  $q\bar{q}$ -state are obtained by appropriately dividing the PDFs of the photon by the VDM couplings [32].

In contrast to the slope of soft processes (c.f. Eq.(2.24)), QCD calculations within the leading-log approximation predict an energy-independent slope for hard interactions [89]. Therefore a constant slope is used [90,25]

$$b_H = \frac{1}{2} (b_{q\bar{q}P}^0 + b_{NP}^0) . \quad (2.28)$$

High-mass diffractive processes: Before giving expressions for cross sections and slopes the following comment is in order. For a description of high- $p_\perp$  particle production in diffractive interactions each of the ‘‘pomeron’’ which build up an enhanced graph (see Fig. 2.4) can itself be considered as being composed of multiple soft and hard pomeron exchanges (Fig. 2.5) [91,46]. Therefore all ‘‘pomeron’’ drawn in the graphs of Fig. 2.4

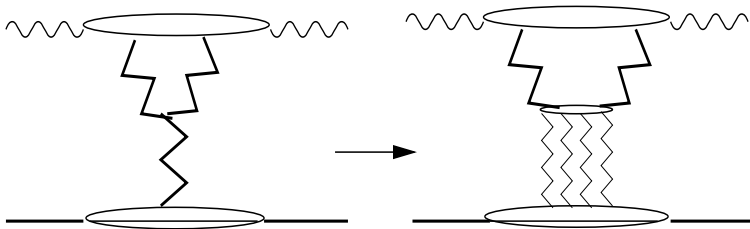


Figure 2.5: Each of the three renormalized pomerons of the TP graph represents multiple pomeron exchange. Here it is shown for the lower part of the TP diagram.

represent more elementary multiple pomeron exchange graphs. In the following they are called *renormalized* pomerons ( $\tilde{P}$ ). The parameters of a renormalized pomeron (couplings, trajectory) are assumed to differ from the ones of the soft pomeron only by the intercept ( $\alpha_{\tilde{P}}(t) = 1 + \Delta_{\tilde{P}} + \alpha'_{\tilde{P}}(0)t$ ) [92]. For the couplings the notation ‘‘ $P$ ’’ is therefore kept.

As examples, only the expressions needed to calculate  $\chi_{TP}$  are given. The formulas for the loop- and double-pomeron graphs as well as details of their calculation can be found in [32,34,46].

Two of the renormalized pomerons of the TP graph are either connected to the  $q\bar{q}$ -state or to the nucleon. The diffractive cut of these graphs (see further below) corresponds to nucleon- or  $q\bar{q}$ -single diffractive dissociation, respectively. Both configurations contribute to the eikonal function:  $\chi_{TP} = \chi_{TP,N} + \chi_{TP,q\bar{q}}$ . Introducing a TP coupling  $g_{3P}$  by ( $t_1$ ,  $t_2$  and  $t_3$  are the squared 4-momenta of the pomerons)

$$g_{3P}(t_1, t_2, t_3) = g_{3P}^0 e^{b_{3P}^0(t_1+t_2+t_3)/2} \quad (2.29)$$

the TP cross section corresponding to nucleon diffraction dissociation can be calculated within Regge theory. One obtains

$$\sigma_{TP,N}(s) = \frac{(g_{q\bar{q}P}^0)^2 g_{NP}^0 g_{3P}^0}{16\pi s_0 2\alpha'_{\tilde{P}}(0)} \left(\frac{s}{s_0}\right)^{\Delta_{\tilde{P}}} [\text{Ei}(c \cdot c_L(s)) - \text{Ei}(c \cdot c_U(s))] e^{-c} \quad (2.30)$$

with the following factors in the exponential-integral functions

$$c_L(s) = 1 - \frac{\Delta_{\tilde{P}}}{c} \ln \frac{M_L^2}{s}, \quad c_U(s) = 1 - \frac{\Delta_{\tilde{P}}}{c} \ln \frac{M_U^2}{s}, \quad c = \Delta_{\tilde{P}} \frac{b_{q\bar{q}P}^0 + b_{3P}^0}{2\alpha'_{\tilde{P}}(0)} \quad (2.31)$$

where  $M_L$  and  $M_U$  are energy independent lower and upper limits restricting the total energy of the lower part of the graph in Fig. 2.4a (the diffractive mass). The effective<sup>1</sup> slope parameter  $b_{TP,N}$  is given by

$$b_{TP,N}(s) = \frac{1}{2} (b_{q\bar{q}P}^0 + b_{NP}^0) + b_{3P}^0 + \alpha'_{IP}(0) \left\{ \ln \frac{s}{s_0} + \frac{\ln(M_L/M_U)}{\ln(c_L(s)/c_U(s))} \right\}. \quad (2.32)$$

The cross section and slope for  $q\bar{q}$ -diffraction dissociation,  $\sigma_{TP,q\bar{q}}$  and  $b_{TP,q\bar{q}}$ , can formally be obtained by interchanging  $q\bar{q}$  and  $N$  in Eqs.(2.30)-(2.32).

**Two-channel eikonal formalism:** So far, the excitation of the scattering particles to resonance states ( $q\bar{q} \rightarrow q\bar{q}^*$  and/or  $N \rightarrow N^*$  and vice versa) by pomeron exchange has been omitted. In the model, these processes are taken into account employing a two-channel eikonal formalism. Within this formalism it is assumed that the amplitudes are modified by introducing coupling constants and slopes which depend on the masses of the quasi-elastically scattering particles in the initial and final state. For example, for the amplitude of the process  $(q\bar{q}, N) \rightarrow (q\bar{q}^*, N^*)$  it corresponds to the substitutions

$$g_{kP}(t) \longrightarrow \tilde{g}_{kP}(t) = \lambda_k g_{kP}^0 \exp \left( \frac{1}{2} b_{kP}^0 e^{-c(m_k - m_{k^*})^2 t} \right), \quad (2.33)$$

$$\left( \frac{s}{s_0} \right)^{\alpha'_{IP}(0)t} \longrightarrow \left( \frac{ss_0}{(m_{q\bar{q}}^2 + m_{q\bar{q}^*}^2)(m_N^2 + m_{N^*}^2)} \right)^{\alpha'_{IP}(0)t}, \quad (2.34)$$

$$\sigma_H \longrightarrow \tilde{\sigma}_H = \lambda_{q\bar{q}} \lambda_N \sigma_H, \quad 0 \leq \lambda_k \leq 1. \quad (2.35)$$

The subscript  $k$  stands for  $q\bar{q}$  and  $N$ , respectively. In addition, the substitutions (2.33) and (2.34) have to be done for the reggeon amplitude. The constant  $c$  is fixed at  $3 \text{ GeV}^{-2}$ .

Introducing four generic hadronic states

$$|q\bar{q}, N\rangle \sim \begin{pmatrix} 1 \\ 0 \\ 0 \\ 0 \end{pmatrix} \quad |q\bar{q}^*, N\rangle \sim \begin{pmatrix} 0 \\ 1 \\ 0 \\ 0 \end{pmatrix} \quad |q\bar{q}, N^*\rangle \sim \begin{pmatrix} 0 \\ 0 \\ 1 \\ 0 \end{pmatrix} \quad |q\bar{q}^*, N^*\rangle \sim \begin{pmatrix} 0 \\ 0 \\ 0 \\ 1 \end{pmatrix} \quad (2.36)$$

the eikonal function entering the expression (2.15) for the impact parameter amplitude of resolved processes can be written as a symmetrical  $4 \times 4$  matrix  $\chi(s, \vec{B}) = (\chi_{kl}(s, \vec{B}))$ . The four eikonal functions for the processes  $(q\bar{q}, N) \rightarrow (q\bar{q}, N)$ ,  $(q\bar{q}, N) \rightarrow (q\bar{q}^*, N)$ ,  $(q\bar{q}, N) \rightarrow (q\bar{q}, N^*)$  and  $(q\bar{q}, N) \rightarrow (q\bar{q}^*, N^*)$  constitute the elements of this matrix. Thus, also the amplitude Eq.(2.15) becomes a symmetrical  $4 \times 4$  matrix  $a_{\gamma N}^{\text{res}}(s, \vec{B}) = (a_{\gamma N, kl}^{\text{res}}(s, \vec{B}))$ . For practical calculations it is convenient to diagonalize the eikonal matrix:  $\chi^{\text{diag}} = U^T \chi U$ . Then the scattering amplitude reads

$$a_{\gamma N}^{\text{res}}(s, \vec{B}) = (a_{\gamma N, kl}^{\text{res}}(s, \vec{B}))_{\substack{k=1\dots 4 \\ l=1\dots 4}} = \frac{i}{2} U \left( 1 - e^{-\chi^{\text{diag}}(s, \vec{B})} \right) U^T. \quad (2.37)$$

<sup>1</sup>As emphasized in [93], the calculation of the enhanced graphs within Regge theory does not result in impact parameter amplitudes with Gaussian shape. However, they might be approximated with Gaussian functions using effective slope parameters

The formalism allows to calculate cross sections for low-mass diffraction. For example, for the cross section of low-mass photon diffractive dissociation (LMSD, $\gamma$ ) one obtains

$$\begin{aligned}\sigma_{\gamma N}^{\text{LMSD},\gamma}(s) &= 4 \int d^2 \vec{B} \left| \langle q\bar{q}^*, N | a_{\gamma N}^{\text{res}}(s, \vec{B}) | \gamma_{\text{had}}, N \rangle \right|^2 \\ &= 4 \int d^2 \vec{B} \left| \frac{e}{f_{q\bar{q}}} a_{\gamma N,12}^{\text{res}}(s, \vec{B}) + \frac{e}{f_{q\bar{q}^*}} a_{\gamma N,22}^{\text{res}}(s, \vec{B}) \right|^2.\end{aligned}\quad (2.38)$$

### Direct processes

Examples for direct photon–nucleon interactions are shown in Fig. 2.6. Again, the short distance cross section  $\hat{\sigma}_{\gamma,i \rightarrow k,l}$  for the partonic scattering process can be estimated within lowest order perturbative QCD. Hence the cross section for the direct process reads

$$\sigma_{\gamma N}^{\text{dir}}(s, p_{\perp}^{\text{cut}}) = \int dx d\hat{t} \sum_{i,k,l} f_{i|N}(x, \mu^2) \frac{d\hat{\sigma}_{\gamma,i \rightarrow k,l}}{d\hat{t}} \Theta(p_{\perp} - p_{\perp}^{\text{cut}}). \quad (2.39)$$

In contrast to resolved processes, absorptive corrections to direct photon interactions

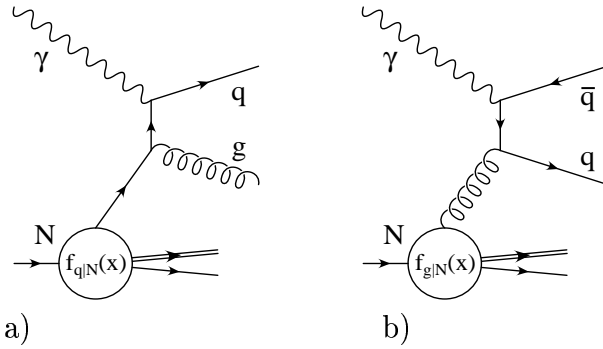


Figure 2.6: *Direct photon–nucleon interactions: a) gluon–Compton scattering and b) photon–gluon fusion.*

are suppressed by one order of  $\alpha_{\text{em}}$  and are therefore neglected. With a slope  $b_{\gamma N}^{\text{dir}} = b_{\text{H}}$  (Eq.(2.28)) the impact parameter amplitude for direct processes is given by

$$a_{\gamma N}^{\text{dir}}(s, \vec{B}) = i \frac{\sigma_{\gamma N}^{\text{dir}}(s)}{16\pi b_{\gamma N}^{\text{dir}}} e^{-\vec{B}^2/(4b_{\gamma N}^{\text{dir}})}. \quad (2.40)$$

### Free parameters of the model

The formalism sketched so far contains a certain number of free parameters which have to be fixed before cross sections can be predicted. In particular, these are

- the intercept and slope parameters of the pomeron ( $\alpha_{\text{IP}}(0), \alpha'_{\text{IP}}(0)$ ) and reggeon trajectories ( $\alpha_{\text{IR}}(0), \alpha'_{\text{IR}}(0)$ ),
- the intercept of the renormalized pomeron trajectory ( $\alpha_{\tilde{\text{IP}}}(0)$ ),
- the parameters entering the nucleon–pomeron(reggeon) ( $g_{N\text{IP}(\text{IR})}^0, b_{N\text{IP}(\text{IR})}^0$ ),  $q\bar{q}(q\bar{q}^*)$ –pomeron(reggeon) ( $g_{q\bar{q}\text{IP}(\text{IR})}^0, b_{q\bar{q}\text{IP}(\text{IR})}^0$ ) and triple-pomeron couplings ( $g_{3\text{IP}}^0, b_{3\text{IP}}^0$ ),
- the coupling constants of the  $q\bar{q}$ – and  $q\bar{q}^*$ –photon vertices ( $e/f_{q\bar{q}}, e/f_{q\bar{q}^*}$ ),

- the transverse momentum cutoff ( $p_{\perp}^{\text{cut}}$ ) and
- the parameters  $\lambda_N$  and  $\lambda_{q\bar{q}}$  modifying the couplings in case of low-mass excitations by pomeron or reggeon exchange.

Out of them some parameters are either taken from the literature ( $\alpha'_{IP}(0)$ ,  $\alpha'_{IR}(0)$ ,  $\alpha'_{IR}(0)$ ,  $\alpha'_{\tilde{IP}}(0)$ ,  $b_{3IP}^0$ ,  $\lambda_N$ ) or are fixed using suitable assumptions ( $\lambda_{q\bar{q}}$  by applying finite mass sum rules and  $p_{\perp}^{\text{cut}} = 3 \text{ GeV}/c$ ). The remaining parameters are determined by fitting cross sections and slope parameters calculated within the model to data:  $\alpha_{IP}(0)$ ,  $g_{NIP(IR)}^0$ ,  $b_{NIP(IR)}^0$ , and  $g_{3IP}^0$  follow from fits to data on hadron–hadron scattering only. The parameters  $e/f_{q\bar{q}}$ ,  $g_{q\bar{q}IP(IR)}^0$ ,  $b_{q\bar{q}IP(IR)}^0$  (and those for  $q\bar{q}^*$ ) are obtained from fits to data on photon–hadron scattering. Numerical values and further details can be found in [32,34].

### 2.3.2 Multiparticle Production

#### The optical theorem

According to the optical theorem the total cross section is related to the discontinuity of the forward scattering amplitude

$$\sigma_{\gamma N}^{\text{tot}}(s) \approx \frac{1}{2s} \text{disc}_s(A_{\gamma N}(s, t = 0)) = \frac{1}{s} \Im m(A_{\gamma N}(s, t = 0)) . \quad (2.41)$$

Since pomeron exchange can be represented by graphs with multiperipheral kinematics, it is possible to consider the discontinuity as an unitarity cut of these graphs moving particles of the intermediate state on their mass shell (see Fig. 2.7). As previously dis-

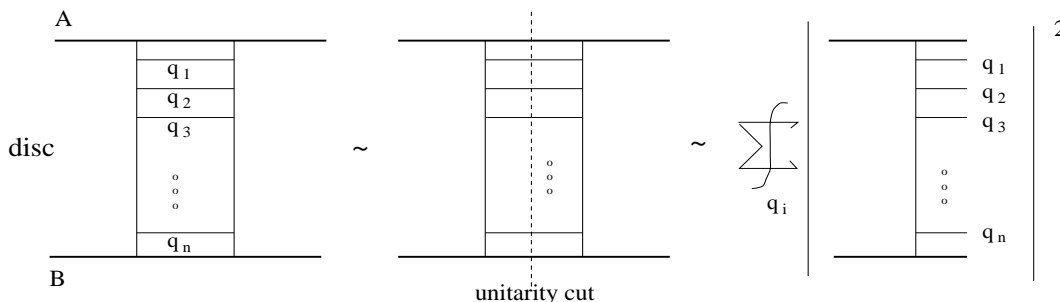


Figure 2.7: *Graphical representation of the optical theorem for the one-pomeron exchange graph*

cussed, the amplitude for resolved photon–nucleon interactions is built up of contributions corresponding to multiple pomeron exchange. This would imply that a large number of different cuts has to be taken into account. It can be however shown that the dominant contributions to the cross section are given by those cuts which involve all intermediate particle states of a pomeron [94].

#### AGK-cutting rules

In the limit of high energies a prescription for the summation of the different cut contributions is provided by the Abramovski–Gribov–Kancheli (AGK) cutting rules [94]. According to these rules the contribution of a  $n$ -pomeron exchange graph (see Eq.(2.15))

to the total cross section can be decomposed into a sum over  $\nu$  terms ( $\nu = 0 \dots n$ ) with weight-factors  $B_\nu^n$ . Each of these terms corresponds to  $\nu$  cut pomerons. Resummation yields for the amplitude a sum over contributions representing certain numbers of cut pomerons

$$a_{\gamma N}^{\text{res}}(s, \vec{B}) = \sum_{n=1}^{\infty} a^{(n)}(s, \vec{B}) = \sum_{n=1}^{\infty} \sum_{\nu=0}^n B_\nu^n a^{(n)}(s, \vec{B}) = \sum_{\nu=0}^{\infty} a(\nu, s, \vec{B}) . \quad (2.42)$$

Thus, the partial cross section coming from all diagrams with  $j_c$  cut soft pomerons,  $k_c$  cut hard pomerons,  $l_c$  cut triple-pomeron graphs,  $m_c$  cut loop-pomeron graphs,  $n_c$  cut double-pomeron graphs and an arbitrary number of uncut ones is given by

$$\sigma_{j_c, k_c, l_c, m_c, n_c} = \langle \gamma_{\text{had}}, N | \left( \frac{(2\chi_S)^{j_c}}{j_c!} \frac{(2\chi_H)^{k_c}}{k_c!} \frac{(2\chi_{\text{TP}})^{l_c}}{l_c!} \frac{(2\chi_{\text{LP}})^{m_c}}{m_c!} \frac{(2\chi_{\text{DP}})^{n_c}}{n_c!} e^{-2\chi} \right) | \gamma_{\text{had}}, N \rangle \quad (2.43)$$

where according to Eqs.(2.12) and (2.13)

$$\frac{1}{4} \sum_{j_c+k_c+l_c+m_c+n_c \geq 1} \sigma_{j_c, k_c, l_c, m_c, n_c}(s, \vec{B}) = \Im m \langle \gamma_{\text{had}}, N | a_{\gamma N}^{\text{res}}(s, \vec{B}) | \gamma_{\text{had}}, N \rangle - \left| \langle \gamma_{\text{had}}, N | a_{\gamma N}^{\text{res}}(s, \vec{B}) | \gamma_{\text{had}}, N \rangle \right|^2 . \quad (2.44)$$

It should be noted that not all of the partial cross sections are positive quantities. The reason is that a cut of an enhanced graph can be further decomposed into one-, two-, or three-pomeron cuts. Taking this fact into consideration the resulting  $n$ -pomeron cut contributions are all positive.

### Color flow topologies

In order to relate the partial cross sections defined by Eq.(2.43) to final state parton configurations, the equivalence between reggeon and pomeron exchange amplitudes and certain color flow topologies is used [95]. In Fig. 2.8 the color flows of single reggeon and pomeron exchange are shown together with the corresponding cuts. Whereas a cut reggeon

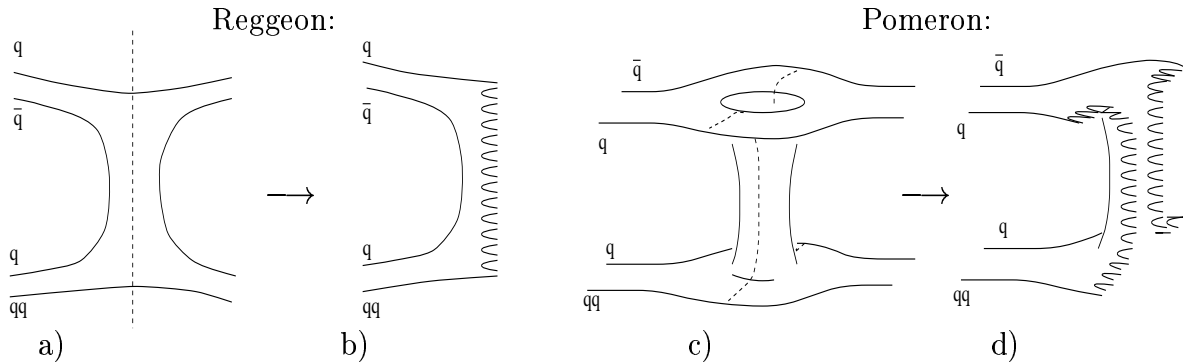


Figure 2.8: *Color flow picture of a single reggeon exchange graph (a) and the corresponding unitarity cut (b). In (c) and (d) the same is shown for a single pomeron exchange graph.*

yields one color-field string, a cut pomeron results in two strings which are assumed to fragment independently into hadrons. In the large- $N_c$  limit of QCD the same color flow picture of the pomeron is also found in hard interactions.

## Final state partons and hadronization

Low- $p_\perp$  final state: In case of reggeon cuts and those pomeron cuts which do not involve large momentum transfer, the partonic interpretation of the DPM is assumed: Hadronic fluctuations of the photon and mesons are split into a (valence) quark-antiquark pair whereas baryons are approximated by a (valence) quark-diquark pair. The longitudinal momentum fractions of the partons are given by Regge-asymptotics [96–99]. The momentum fractions  $x$  of valence quarks in a non-strange meson (or hadronic photon fluctuation) or in a baryon are obtained from

$$\text{meson : } \rho(x) \sim x^{-0.5}(1-x)^{-0.5}, \quad \text{baryon : } \rho(x) \sim x^{-0.5}(1-x)^{1.5}. \quad (2.45)$$

For strange valence quarks the corresponding exponent of  $x$  is modified to  $-0.3$ . In multiple interaction events (i.e. multiple cut pomerons), the sea quark momenta are sampled using a  $\rho(x) \sim 1/x$  behavior. Transverse momenta of soft partons are not predicted by the DPM. Here, an exponential distribution is assumed

$$\frac{d^2 N_s}{dp_\perp^2} \sim e^{-\beta p_\perp}. \quad (2.46)$$

The energy-dependent slope parameter  $\beta$  is obtained requiring a smooth transition between the transverse momentum distributions of the soft constituents and the hard scattered partons. Flavors of sea partons are sampled according to [100].

High- $p_\perp$  final state: For pomeron cuts involving a hard scattering, the parton kinematics as well as the flavors and colors are sampled according to the QCD-improved Parton Model using leading-order matrix elements [101,102]. For the calculations discussed further below leading-order Glück-Reya-Vogt (GRV) PDF parametrizations are used for photons [103,104] and nucleons [105]. Both, initial and final state parton showers are treated.

Hadronization: Color neutral strings hadronize according to the JETSET-realization of the Lund-model [106,107].

## Small photon virtualities

So far, the model has been discussed in the limit of real photon–nucleon interactions. Small photon virtualities  $Q^2$  are treated in the following way:

- According to the GVDM (see Sec. 2.1) the total cross section approximately factorizes into a  $Q^2$ -independent cross section and a factor  $F(Q^2)$  containing the dependence on the photon virtuality

$$\sigma_{\gamma N}^{\text{tot}}(s, Q^2) = F(Q^2) \sigma_{\gamma N}^{\text{tot}}(s). \quad (2.47)$$

For  $F$  the parametrization given in [108] is used

$$F(Q^2) = \sum_{V=\rho,\omega,\phi} r_V \left( \frac{m_V^2}{m_V^2 + Q^2} \right)^2 \left( 1 + \frac{Q^2}{4m_V^2} \right) + r_{\text{eff}} \left( \frac{M_{\text{eff}}^2}{M_{\text{eff}}^2 + Q^2} \right). \quad (2.48)$$

- The PDFs of the photon are assumed to be suppressed by weak photon virtualities according to the parametrizations [109–111]

$$f_{q|\gamma}(x, \mu^2, Q^2) = K f_{q|\gamma}(x, \mu^2), \quad f_{g|\gamma}(x, \mu^2, Q^2) = K^2 f_{g|\gamma}(x, \mu^2) \quad (2.49)$$

with

$$K = \ln \left( \frac{\mu^2}{m_\rho^2 + Q^2} \right) / \ln \left( \frac{\mu^2}{m_\rho^2} \right). \quad (2.50)$$

- Events with  $n$  cut soft pomerons ( $n \geq 2$ , multiple interactions) are suppressed by a factor  $(m_\rho^2/(m_\rho^2 + Q^2))^{n-1}$ .

## 2.4 Cross Sections and Nuclear Shadowing in Photon–Nucleus Collisions

Similar to the scattering off free nucleons many features of high-energy interactions of real and weakly virtual photons with nuclei are well described in the framework of the GVDM [71,76]. A spectral relation like Eq.(2.8) for  $\sigma_{\gamma^*N}$  provides also a reasonable approximation for photon–nucleus cross sections  $\sigma_{\gamma^*A}$  (see [23] and references therein)

$$\sigma_{\gamma^*A}(s, Q^2) = 4\pi\alpha_{\text{em}} \int_{M_0^2}^{M_1^2} dM^2 D(M^2) \left( \frac{M^2}{M^2 + Q^2} \right)^2 \left( 1 + \epsilon \frac{Q^2}{M^2} \right) \sigma_{VA}(s, Q^2, M^2). \quad (2.51)$$

Here, all properties of the interactions of the  $q\bar{q}$ -states with the nuclear target of mass number  $A$  are contained in the effective cross section  $\sigma_{VA}$ . In the following a detailed model for the calculation of  $\sigma_{VA}$  is developed.

In the kinematic limit of photoproduction, interactions of  $q\bar{q}$ -states with nuclei show similar properties as those of hadrons. In hadron–nucleus collisions shadowing is well described within the Gribov–Glauber multiple scattering formalism [64–66]. Therefore the two-component DPM which incorporates the Gribov–Glauber formalism should also be able to describe the  $q\bar{q}$ -nucleus interactions and, especially, the shadowing behavior. However, there are two important differences between interactions induced by hadrons and those by hadronic fluctuations:

- At low energies and/or large  $Q^2$  and  $M^2$  the coherence length of the hadronic fluctuation (Eq.(2.5)) may become comparable or even smaller than the nuclear radius [76].
- At very high energies the photon interacts with a certain probability (increasing with energy) as a point-like object which can be associated with states of large  $M^2$ .

Both effects may lead to a suppression of shadowing and have to be introduced explicitly into the Gribov–Glauber formalism. In particular, the second effect will be studied in detail throughout the following sections.

### 2.4.1 Total Photon–Nucleon Cross Sections

Turning again to photon–nucleon interactions the dependence of the cross sections on the mass  $M$  of the hadronic fluctuation is studied for the following reasons.

If low- $Q^2$  photon–nucleon scattering is considered only, a detailed model for the  $M^2$ - and  $Q^2$ -dependence of the process is not needed. This is due to the fact that at high collision energies the coherence length of the hadronic fluctuation almost always exceeds the typical hadronic interaction length  $d_{\text{int}}$  (for nucleons  $d_{\text{int}} \sim r_N \approx 1$  fm). As shown in [32,33] and also summarized in the previous sections a good description can already be obtained by introducing two generic states instead of incorporating a mass-dependence explicitly. For the reasons outlined above, in photon–nucleus interactions the situation is different. Furthermore since the Gribov–Glauber approximation describes the scattering process in terms of individual  $q\bar{q}$ -nucleon interactions suitable assumptions for the dependence also of the latter processes on  $M$  are required. In particular, the effective  $q\bar{q}$ -nucleon cross section  $\sigma_{VN}$  (c.f. Eq.(2.8)) has to be calculated which will enter directly the calculation of  $\sigma_{VA}$  to be described further below.

Consider the kinematics at the  $\gamma \rightarrow q\bar{q}$  vertex of the photon–nucleon interaction in the nucleon rest frame: The 4-momenta of the photon, the quark and the antiquark are given by

$$q = (\nu, \vec{0}, k), \quad p_q = (E_q, \vec{p}_\perp, zk), \quad p_{\bar{q}} = (E_{\bar{q}}, -\vec{p}_\perp, (1-z)k) \quad (2.52)$$

where  $z$  is the fraction of the longitudinal momentum of the photon carried by the quark. Assuming the coupling of a real photon to massless quarks and considering the kinematic limit  $zk, (1-z)k \gg p_\perp = |\vec{p}_\perp|$ , the mass  $M$  of the  $q\bar{q}$ -pair is proportional to the transverse momentum of the quarks

$$M^2 = (E_q + E_{\bar{q}})^2 - k^2 \approx \frac{p_\perp^2}{z(1-z)}. \quad (2.53)$$

Furthermore with  $\Delta t \approx 2\nu/M^2$  being the coherence time of the  $q\bar{q}$ -fluctuation (Eq.(2.5)), the transverse separation of the quarks reads

$$r_\perp = \frac{1}{2}\Delta t \left( \frac{p_\perp}{E_q} - \frac{-p_\perp}{E_{\bar{q}}} \right) \approx \frac{1}{p_\perp} \sim \frac{1}{M}. \quad (2.54)$$

As a consequence, it can be expected that  $\sigma_{VN}$  decreases like  $1/M^2$  at large  $M^2$  [72,73]. Following Ref. [72] this effect is approximated by parametrizing  $\sigma_{VN}$  as

$$\sigma_{VN}(s, Q^2, M^2) = \frac{\tilde{\sigma}_{VN}(s, Q^2)}{M^2 + Q^2 + C^2}. \quad (2.55)$$

Here,  $C$  is a model-dependent parameter [72] and taken to be  $C^2 = 2 \text{ GeV}^2$ . With Eq.(2.55) the  $M^2$ -dependence of the integrand in Eq.(2.8) is explicitly known and the integration over  $M^2$  between  $M_0^2 = 4m_\pi^2$  and  $M_1^2 = s$  can be performed:

$$\sigma_{\gamma^*N}(s, Q^2) = 4\pi\alpha_{\text{em}} I(s, Q^2) \tilde{\sigma}_{VN}(s, Q^2) \quad (2.56)$$

with

$$I(s, Q^2) = \int_{4m_\pi^2}^s dM^2 D(M^2) \frac{M^4}{(M^2 + Q^2)^2 (M^2 + Q^2 + C^2)} \left( 1 + \epsilon \frac{Q^2}{M^2} \right). \quad (2.57)$$

It is not attempted to model the effective cross section  $\sigma_{VN}$  from basic concepts. Eqs.(2.55) and (2.56) allow the calculation of  $\sigma_{VN}$  provided that  $\sigma_{\gamma^*N}$  is known

$$\sigma_{VN}(s, Q^2, M^2) = \frac{\sigma_{\gamma^*N}(s, Q^2)}{4\pi\alpha_{\text{em}}I(s, Q^2)(M^2 + Q^2 + C^2)}. \quad (2.58)$$

For our purposes, there are two possibilities to obtain  $\sigma_{\gamma^*N}$ :

1. The cross sections calculated in the framework of the two-component DPM together with the assumptions for treating low photon virtualities (Sec. 2.3.2) can be used. The advantage is that in this case a detailed model for inelastic final states exists. However, the drawback of this choice would be its limitation to rather low  $Q^2$ -values.
2. Alternatively, a parametrization of the structure function  $F_2^N$  can be applied (see Eq.(2.7)). Suitable parametrizations are provided by the model of Capella *et al.* [112] (CKMT-model) or are those of Abramowicz *et al.* [113] and (in the low  $Q^2$ -range) of Badelek and Kwiciński [114].

Since multiparticle photoproduction off nuclei shall also be described, the first option provides the most consistent way to calculate  $\sigma_{VN}$ . It will therefore be used for the description of particle production discussed further below. However, for the moment the latter possibility, in particular the CKMT-model, is taken into consideration. This enables us to discuss photon–nucleus cross sections and the shadowing behavior in both, the  $Q^2$ -region of photoproduction and the transition region to Deep Inelastic Scattering (DIS).

The CKMT-model provides a simple analytical parametrization of  $F_2^N$  valid for  $0 \leq Q^2 \lesssim 5 \text{ GeV}^2$ . Using the ansatz for the gluon distribution as given in [112] the structure function  $F_2^N$  is calculated for higher virtualities from a QCD evolution in leading logarithmic approximation. Inserting the resulting cross section  $\sigma_{\gamma^*N}$  into Eq.(2.58)  $\sigma_{VN}$  follows for all values of  $s$ ,  $Q^2$  and  $M^2$ .

In Fig. 2.9 the photoproduction cross sections  $\sigma_{\gamma p}^{\text{tot}}$  obtained from the CKMT-model

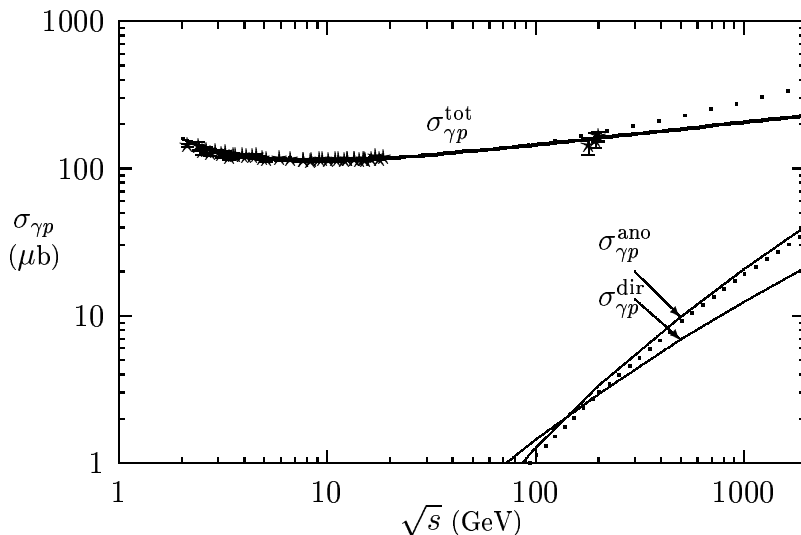


Figure 2.9: Total photon–proton cross sections ( $Q^2 = 0$ ) as calculated with the CKMT-model [112] (thick solid line) and the two-component DPM (dotted line) are shown together with data [115–117]. In addition, the contribution from direct processes and the cross section of the anomalous component of the photon-PDFs are given.

(thick solid line) and calculated within the two-component DPM [32] (dotted line) are

compared to data [115–117]. In the experimentally studied energy region, both models give almost identical results. Differences in the high-energy extrapolations reflect the typical size of the theoretical uncertainties. Also shown are the contributions from point-like processes which will be explained below.

In Fig. 2.10a the energy dependence of the effective cross section  $\sigma_{VN}$  is shown for

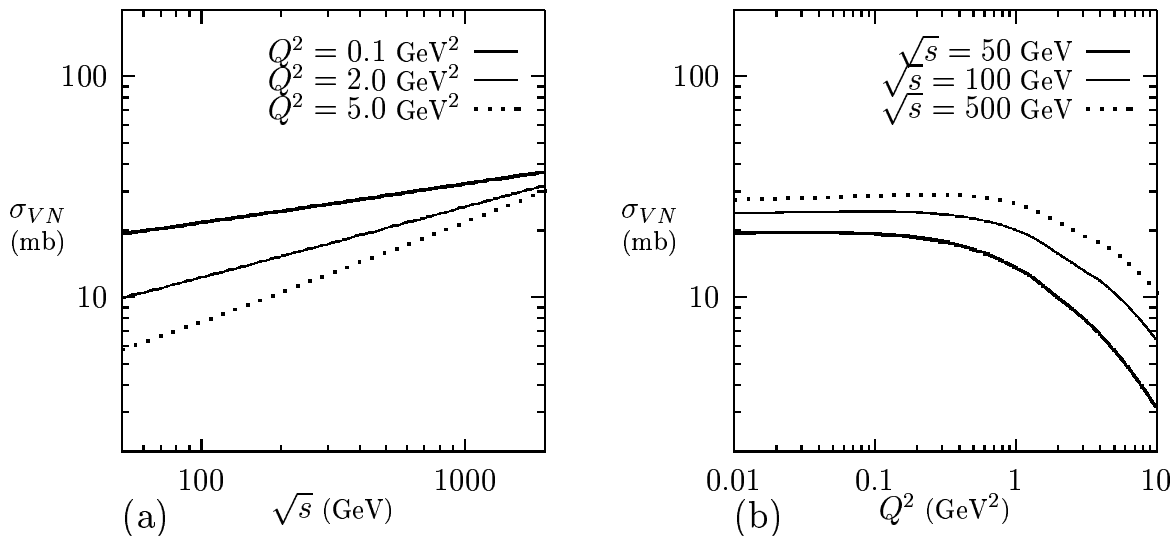


Figure 2.10: *Effective  $q\bar{q}$ -nucleon cross sections at the  $\rho$ -mass. In a) the dependence on the center of mass (c.m.) energy is given for three different photon virtualities. In b) the  $Q^2$ -behavior is shown for three different energies.*

$M^2 = m_\rho^2$  and different photon virtualities. As observed in  $\gamma^*p$  collisions, the rise of the cross section with energy becomes steeper with increasing photon virtuality. In Fig. 2.10b  $\sigma_{VN}$  is given as function of  $Q^2$  for different energies and shows the expected weak  $Q^2$ -dependence for  $Q^2 < m_\rho^2 + C^2$ .

## 2.4.2 Point-Like Photon Interactions

The integral in Eq.(2.8) receives also contributions from hadronic fluctuations with large mass  $M$  which might be formed, according to Eq.(2.53), by partons with large transverse momenta. In terms of the QCD-improved Parton Model, hadronic interactions of these  $q\bar{q}$ -states correspond to point-like photon interactions. On this basis, direct and resolved photon interactions are included in Eq.(2.8).

Of course, a sharp distinction between direct and resolved interactions is not possible. In direct interactions, the photon couples directly to a parton of the nucleon which determines the highest virtuality of the scattering process (Fig. 2.11a). On the other hand, in resolved interactions the photon may fluctuate into a  $q\bar{q}$ -pair with high virtuality. As depicted in Fig. 2.11b, this  $q\bar{q}$ -pair can, for example, emit a gluon leading to a further increase of the virtuality of the emitting quark. The virtuality of this quark eventually determines the highest virtuality of the hard scattering process. Formally, this resolved process differs from the (direct) photon-gluon fusion process (Fig. 2.11a) only by the

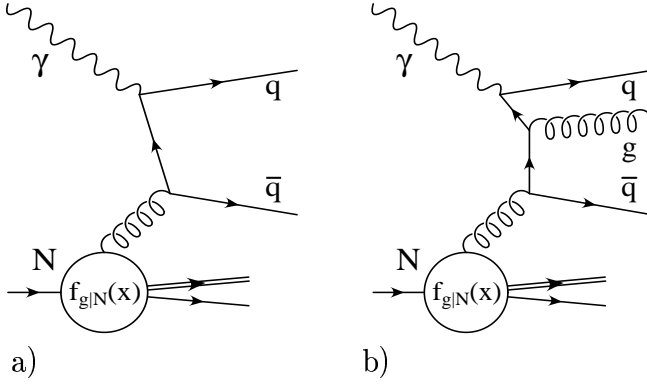


Figure 2.11: *Examples for point-like photon–nucleon interactions. In (a) a direct process and in (b) an anomalous photon interaction are shown.*

additionally emitted gluon illustrating the steady transition between direct and resolved processes.

In order to characterize a hard photon–nucleon scattering it is therefore necessary to distinguish two scales:

- (i) the virtuality  $M$  of the hadronic  $q\bar{q}$ -fluctuation and
- (ii) the scale of the hard scattering  $\mu$  which is approximately given by the momentum transfer in the hard scattering process.

Then an interaction can be classified as “direct process” if  $\mu$  and  $M$  fulfill the condition  $\mu^2 \approx M^2$  and as “resolved process” if  $\mu^2 \gg M^2$ . In resolved processes of high-mass fluctuations ( $M^2 \gg \Lambda_{\text{QCD}}^2$ ) not only the hard parton–parton scattering but also the  $\gamma \rightarrow q\bar{q}$  splitting can be calculated within perturbation theory. These interactions are responsible for the rise of the photon structure function with  $\mu^2$  like  $\ln(\mu^2)$  [118] and are frequently called *anomalous* processes (anomalous contribution to the photon structure function [119]). Direct and anomalous photon interactions are point-like processes.

In direct and anomalous processes either  $M^2$  or the squared transverse momentum of the hard scattering  $p_{\perp}^2$  acts as “hard scale” permitting the application of perturbative QCD. The calculation of the cross section for direct processes  $\sigma_{\gamma N}^{\text{dir}}$  has been discussed in Sec. 2.3.1 (Eq.(2.39)). In the following the estimation of the cross section  $\sigma_{\gamma N}^{\text{ano}}$  for the fluctuation of a photon into a  $q\bar{q}$ -system with a large mass  $M$  (i.e. highly virtual quarks) and the interaction of this system with a nucleon is described.

The anomalous cross section is calculated on the basis of MC methods. In particular, the event generator PHOJET [32,33] is applied to sample hard resolved photon–nucleon interactions according to the cross section

$$\sigma_{\gamma N}^{\text{H}}(s, p_{\perp}^{\text{cut}}) = \int dx_1 dx_2 d\hat{t} \sum_{i,j,k,l} \frac{1}{1 + \delta_{k,l}} f_{i|\gamma}(x_1, \mu^2) f_{j|N}(x_2, \mu^2) \frac{d\hat{\sigma}_{i,j \rightarrow k,l}}{d\hat{t}} \Theta(p_{\perp} - p_{\perp}^{\text{cut}}). \quad (2.59)$$

This cross section receives contributions from low- and high-mass  $q\bar{q}$ -states, the latter interacting predominantly in anomalous processes. In order to determine the ratio of anomalous to all hard resolved interactions, initial state parton showers are generated for each sampled hard process. The implementation of initial state radiation in PHOJET is based on a backwards evolution algorithm using the parton transverse momentum as evolution variable. During the shower evolution also hard  $\gamma \rightarrow q\bar{q}$  processes are considered.

In each step of the backwards evolution the parton shower may break down with a certain probability due to a point-like splitting. This probability is approximated by the ratio of the  $\gamma \rightarrow q\bar{q}$  contribution to the quark density in the photon

$$q(x, \mu^2) = \frac{3\alpha_{\text{em}} e_q^2}{2\pi} \left[ (x^2 + (1-x)^2) \ln \left( \frac{1-x}{x} \frac{\mu^2}{(p_{\perp}^{\text{cut}})^2} \right) + 8x(1-x) - 1 \right] \quad (2.60)$$

and the quark density of the full photon PDF. Since only  $\gamma \rightarrow q\bar{q}$  splittings with a remnant quark with  $p_{\perp} > p_{\perp}^{\text{cut}}$  are of interest, the lowest quark virtuality considered in Eq.(2.60) coincides with the transverse momentum cutoff  $p_{\perp}^{\text{cut}}$ . Finally, the ratio of the anomalous cross section to the hard resolved photon–nucleon cross section is given by the fraction of events where an anomalous splitting with  $p_{\perp} > p_{\perp}^{\text{cut}}$  has been sampled.

Uncertainties in the estimation of  $\sigma_{\gamma N}^{\text{ano}}$  arise mainly from the PDFs and the transverse momentum cutoff which both enter the calculation of  $\sigma_{\gamma N}^{\text{H}}$ . In the following parton densities in the nucleon are approximated by parametrizations of Glück, Reya and Vogt (GRV) [105]. These parametrizations turned out to provide a reasonable description of recent measurements on the proton structure function at low  $x$  [120,121]. Alternatively, also the CTEQ4 [122] or the MRS(R) [123] PDFs could be used since within the considered energy range the differences between all these parametrizations are of minor importance for our purpose. Concerning the photon structure function much less experimental information is available. Again, a GRV-parametrization is employed [103,104] which was successfully applied to reproduce HERA-data on photon PDFs [20,124]. In order to estimate uncertainties due to this particular choice, the calculation has been repeated with the SaS-2D parametrization of the photon PDFs [125]. The transverse momentum cutoff is set to 3 GeV/c in both, the calculation of direct and hard resolved processes, for the following reason. A model which should give a reasonable description of photoproduction off nuclei (concerning cross sections *and* particle production) has to be able to describe also the main features of photon–proton interactions. This is an obvious requirement ensuring the consistency of the model. Studying photon–proton collisions at 200 GeV c.m. energy, it was found by the H1-Collaboration [126] that the PHOJET event generator provides a reasonable description of their data if the transverse momentum cutoff is fixed at 3 GeV/c. Therefore this value is used consistently for the calculation of cross sections and of particle production in photon–proton and in photon–nucleus interactions. The choice of a much lower transverse momentum cutoff could spoil the strong parton virtuality ordering assumed in the Parton Model expression (2.59) since very small  $x$ -values would enter this equation [127]. It should be emphasized that the formalism presented here is only applicable for photons with low virtualities, i.e.  $Q^2 \ll 4p_{\perp}^2$ .

In Fig. 2.9 the cross sections  $\sigma_{\gamma p}^{\text{dir}}$  and  $\sigma_{\gamma p}^{\text{ano}}$  calculated using GRV PDFs are shown (solid lines). In addition, results from a calculation using the above mentioned SaS-2D PDFs for the photon are plotted (dotted line). The differences between the results obtained with the two photon PDFs appear to be small and do not change any qualitative conclusion drawn from this investigation.

### 2.4.3 Total Photon–Nucleus Cross Sections

With the effective  $q\bar{q}$ –nucleon cross section  $\sigma_{VN}$  and the cross sections for point-like photon interactions  $\sigma_{\gamma^*p}^{\text{dir}}$  and  $\sigma_{\gamma^*p}^{\text{ano}}$ , now all ingredients for the calculation of  $\sigma_{\gamma A}$  from the GVDM-

expression (2.51) are available.

In analogy to the photon–nucleon cross sections Eqs.(2.12,2.13), the total, elastic and inelastic  $q\bar{q}$ –nucleus cross sections  $\sigma_{VA}^{\text{tot}}$ ,  $\sigma_{VA}^{\text{el}}$ , and  $\sigma_{VA}^{\text{inel}}$  are related to the corresponding impact parameter amplitude  $a_{VA}$  by the following equations

$$\sigma_{VA}^{\text{tot}}(s, Q^2, M^2) = 4 \int d^2\vec{B} \Im m \left\{ a_{VA}(s, Q^2, M^2, \vec{B}) \right\}, \quad (2.61)$$

$$\sigma_{VA}^{\text{el}}(s, Q^2, M^2) = 4 \int d^2\vec{B} \left| a_{VA}(s, Q^2, M^2, \vec{B}) \right|^2, \quad (2.62)$$

$$\begin{aligned} \sigma_{VA}^{\text{inel}}(s, Q^2, M^2) &= \sigma_{VA}^{\text{tot}}(s, Q^2, M^2) - \sigma_{VA}^{\text{el}}(s, Q^2, M^2) \\ &= \int d^2\vec{B} \left( 1 - \left| 1 + 2ia_{VA}(s, Q^2, M^2, \vec{B}) \right|^2 \right). \end{aligned} \quad (2.63)$$

The amplitude  $a_{VA}$ , as it enters Eqs.(2.61–2.63), is averaged over coordinate space using nuclear ground state wave functions  $\psi_A$

$$a_{VA}(s, Q^2, M^2, \vec{B}) = \int \prod_{j=1}^A d^3r_j \psi_A^*(\vec{r}_1, \dots, \vec{r}_A) a_{VA}(s, Q^2, M^2, \vec{B}, \vec{r}_1, \dots, \vec{r}_A) \psi_A(\vec{r}_1, \dots, \vec{r}_A) \quad (2.64)$$

where  $\vec{r}_1, \dots, \vec{r}_A$  are the nucleon coordinates. The origin of the coordinate frame is chosen to be in the center of the nucleus, the  $q\bar{q}$ –fluctuations moving into positive  $z$ -direction. Neglecting correlations between nucleons,  $|\psi_A|^2$  is approximated by a product over one-particle Woods-Saxon density distributions

$$|\psi_A(\vec{r}_1, \dots, \vec{r}_A)|^2 = \prod_{j=1}^A \rho_A(\vec{r}_j) = \prod_{j=1}^A \frac{K}{1 + \exp[(|\vec{r}_j| - R_A)/c]} \quad (2.65)$$

with the parameters  $c = 0.545$  fm and  $R_A = 1.12A^{1/3}$  fm [128].

In order to calculate  $a_{VA}$  the MC formulation of the Gribov–Glauber approximation for hadron–nucleus and nucleus–nucleus collisions by Shmakov *et al.* [129] is extended to photon projectiles. In analogy to the formalism for photon–nucleon scattering (see Eq.(2.15))  $a_{VA}$  is expressed in terms of an eikonal function  $\chi_{VA}$

$$a_{VA}(s, Q^2, M^2, \vec{B}, \vec{r}_1, \dots, \vec{r}_A) = \frac{i}{2} \left( 1 - e^{-\chi_{VA}(s, Q^2, M^2, \vec{B}, \vec{r}_1, \dots, \vec{r}_A)} \right). \quad (2.66)$$

In the following excited intermediate states between interactions of the  $q\bar{q}$ –fluctuations with different target nucleons are neglected (Fig. 2.12). The basic assumption of the Glauber model is that the total phase shift for the particle scattered off a nucleus is equal to the sum of the phase shifts for this particle scattered off individual nucleons (see [130] and references therein). Hence  $\chi_{VA}$  can be written as

$$\chi_{VA}(s, Q^2, M^2, \vec{B}, \vec{r}_1, \dots, \vec{r}_A) = \sum_{\nu=1}^A \chi_{VN}(s, Q^2, M^2, \vec{B}_\nu) \quad (2.67)$$

where  $\vec{r}_\nu = (\vec{s}_\nu, z_\nu)$  and  $\vec{B}_\nu = \vec{B} - \vec{s}_\nu$ . With the impact parameter amplitude  $a_{VN}$  of the  $q\bar{q}$ –nucleon interaction

$$a_{VN}(s, Q^2, M^2, \vec{B}_\nu) = \frac{i}{2} \left( 1 - e^{-\chi_{VN}(s, Q^2, M^2, \vec{B}_\nu)} \right) \quad (2.68)$$

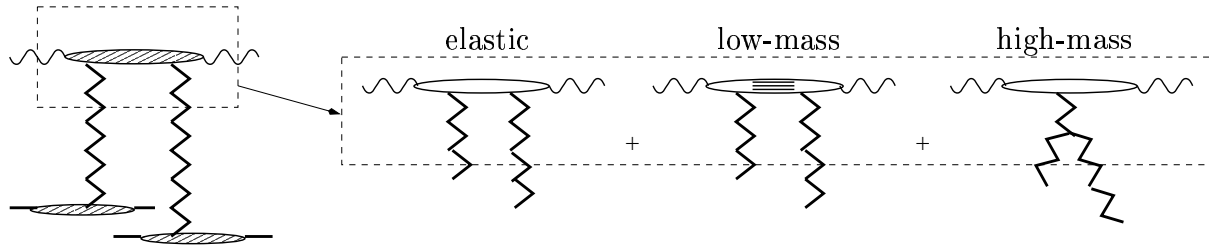


Figure 2.12: Example of a two-pomeron exchange graph in photon–nucleus collisions. The two exchanged pomerons couple to different nucleons. In general, the scattering amplitude includes contributions from elastic, low-mass, and high-mass intermediate states. In the present formulation of the model only elastic intermediate states are taken into consideration.

Eq.(2.66) becomes

$$\begin{aligned} a_{VA}(s, Q^2, M^2, \vec{B}_1, \dots, \vec{B}_A) &= \frac{i}{2} \left( 1 - \prod_{\nu=1}^A e^{-\chi_{VN}(s, Q^2, M^2, \vec{B}_\nu)} \right) \\ &= \frac{i}{2} \left( 1 - \prod_{\nu=1}^A [1 + 2ia_{VN}(s, Q^2, M^2, \vec{B}_\nu)] \right). \end{aligned} \quad (2.69)$$

Similar to the amplitudes (2.20), the following Gaussian parametrization is assumed for  $a_{VN}$

$$a_{VN}(s, Q^2, M^2, \vec{B}_\nu) = i \frac{\sigma_{VN}(s, Q^2, M^2)}{16\pi b_{VN}(s, Q^2, M^2)} (1 - i\rho_{VN}) e^{-\vec{B}_\nu^2 / (4b_{VN}(s, Q^2, M^2))}. \quad (2.70)$$

The calculation of the effective  $q\bar{q}$ -nucleon cross section  $\sigma_{VN}$  has been discussed in Sec. 2.4.1 (Eq.(2.58)). For the slope  $b_{VN}$  the parametrization given in [131] is adopted

$$b_{VN}(s, Q^2, M^2) = b_{VN}^0 + \alpha'_{IP}(0) \ln \left( \frac{s}{M^2 + Q^2} \right), \quad b_{VN}^0 = \left( 2 + \frac{M_\rho^2}{M^2 + Q^2} \right) \text{ GeV}^{-2}. \quad (2.71)$$

The ratio of the real to the imaginary part of the forward scattering amplitude  $\rho_{VN}$  is fixed at a constant value of 0.1 .

Inserting the  $q\bar{q}$ -nucleon amplitude (2.70) into the Gribov–Glauber expression (2.69) the  $q\bar{q}$ -nucleus scattering amplitude is obtained, however, implicitly assuming that the fluctuation length exceeds the characteristic diameter of the nucleus sufficiently. As outlined initially, this picture does not hold at low and very high photon energies due to a limited coherence length and due to possible point-like processes, respectively. Both effects are taken into account in the following way.

Coherence length: The integration over coordinate space in Eq.(2.64) is performed on a MC basis by averaging  $a_{VA}(\dots, \vec{r}_1, \dots, \vec{r}_A)$  over a large number of spatial nucleon configurations. The latter are sampled from Woods-Saxon density distributions (Eq.(2.65)). In order to introduce coherence length effects, for a fixed nucleon configuration the product in Eq.(2.69) is taken only over as many nucleons as their longitudinal separation does not exceed the coherence length  $d$ . In the non-shadowing limit, i.e. if  $d$  is smaller than any internucleon distance, this results in  $a_{VA} = Aa_{VN}$ .

Point-like processes: In direct photon interactions the multiple scattering process inside the nucleus is completely suppressed since the photon couples directly to a parton in a nucleon in a very localized interaction. In contrast, in anomalous photon interactions there is in general (even at large  $M^2$ ) a leading-twist soft contribution to the hard process which might influence the shadowing behavior [132]. However, in order to estimate the maximum possible effect caused by point-like processes it is assumed that also in anomalous photon interactions the Glauber–cascade is reduced to one  $q\bar{q}$ –nucleon scattering and any shadowing contributions are disregarded. With  $\xi$  being the ratio between the point-like and the total photon–nucleon cross sections (see also Fig. 2.9)

$$\xi(s, Q^2) = \frac{\sigma_{\gamma^*N}^{\text{pl}}(s, Q^2)}{\sigma_{\gamma^*N}^{\text{tot}}(s, Q^2)}, \quad \sigma_{\gamma^*N}^{\text{pl}}(s, Q^2) = \sigma_{\gamma^*N}^{\text{dir}}(s, Q^2) + \sigma_{\gamma^*N}^{\text{ano}}(s, Q^2) \quad (2.72)$$

the total photon–nucleus cross section becomes

$$\sigma_{\gamma^*A}^{\text{tot}}(s, Q^2) = \sigma_{\gamma^*A}^{\text{sha}}(s, Q^2) + A\sigma_{\gamma^*N}^{\text{pl}}(s, Q^2). \quad (2.73)$$

The cross section  $\sigma_{\gamma^*A}^{\text{sha}}$  is calculated within the Gribov–Glauber approximation as discussed above, however, now using  $(1 - \xi)\sigma_{VN}$  instead of  $\sigma_{VN}$  in Eq.(2.70).

In Fig. 2.13 results on  $\sigma_{\gamma^*A}^{\text{tot}}$  in the photoproduction limit ( $Q^2 = 0$ ) for carbon, copper

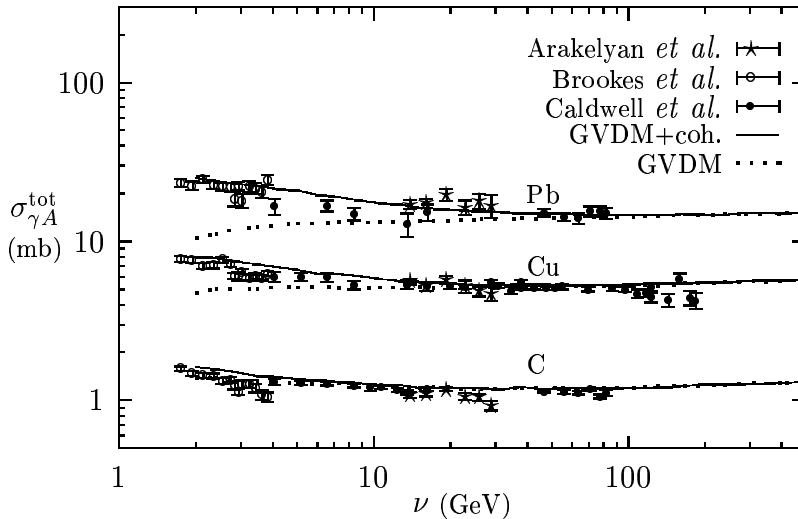


Figure 2.13: Dependence of the total cross sections for interactions of real photons with carbon, copper and lead on the laboratory photon energy. Model results (full lines) are compared to data [133–136]. Dotted lines show the cross sections obtained if coherence length effects would be disregarded.

and lead targets (solid lines) are compared to data [133–136]. The agreement is reasonable except for photon–carbon interactions at low energies where the model predicts slightly less shadowing. However, at  $\nu \approx 2\text{--}3$  GeV the lower energy limit for the applicability of the model is reached. In addition, dotted lines indicate the cross sections which would be obtained if the limited coherence length at low energies were neglected. Whereas this effect is less significant for light targets, it is responsible for the increase of the cross sections towards lower energies observed in interactions of real photons with copper and lead nuclei.

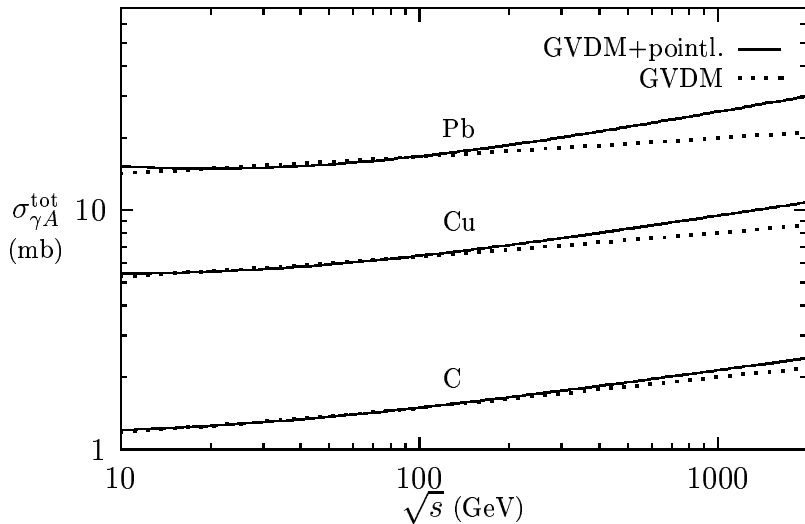


Figure 2.14: *Extrapolation of total cross sections for photoproduction off carbon-, copper- and lead-nuclei.  $\sqrt{s}$  is the photon-nucleon c.m. energy.*

Extrapolating these cross sections to very high energies the effect of point-like interactions should become visible. As shown in Fig. 2.14, they cause a stronger increase of the cross section (solid lines) than obtained if this effect of shadowing suppression would be neglected (dotted lines). The onset at an energy of around 100 GeV clearly coincides with the energy where the contribution of the point-like to the total cross section exceeds the one-percent level (c.f. Fig 2.9).

#### 2.4.4 Nuclear Shadowing Behavior

The per-nucleon ratio of the total photon-nucleus to the total photon-nucleon cross section

$$R_{\gamma^*A} = \frac{\sigma_{\gamma^*A}}{A\sigma_{\gamma^*N}} \quad (2.74)$$

provides a useful measure of nuclear shadowing. Values of  $R_{\gamma^*A}$  well below unity are correlated with strong shadowing whereas  $R_{\gamma^*A}$  approaches unity if shadowing becomes negligible.

Studying first the photoproduction limit we compare in Fig. 2.15 data on the dependence of  $R_{\gamma A}$  on the laboratory energy for carbon, copper and lead targets [133–136] with results of the model. Though it seems that the calculated values follow the trend seen in the data reasonably well (such as increasing shadowing with energy for the two heavier targets), considerable uncertainties within the measurements do not allow to draw further conclusions.

In Fig. 2.16 extrapolations of  $R_{\gamma A}$  in energy are shown up to 2 TeV in the photon-nucleon c.m. frame. As this plot clearly demonstrates, point-like photon interactions may lead to a decrease of nuclear shadowing at high energies (solid lines). In contrast, if point-like interactions are not taken into consideration (dotted lines) the ratios decrease throughout the whole energy range considered.

The shadowing behavior of cross sections in lepton-nucleus interactions has been studied by the E665- [68] and NMC-Collaborations [137,138]. In these experiments photons were produced by bremsstrahlung of 470 GeV and 200 GeV muon beams, respectively. In order to compare experimental data to results of the model, the flux  $g$  of virtual photons has to be calculated. In the limit of high energies and low photon virtualities the flux of

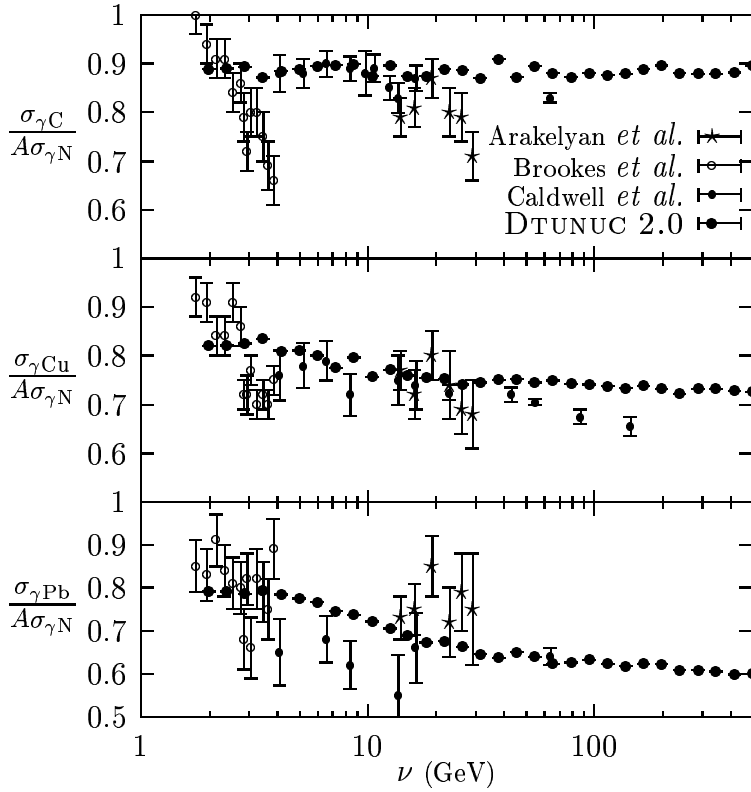


Figure 2.15: Dependence of nuclear shadowing on the photon energy in interactions of real photons with carbon, copper and lead nuclei. Model results are shown together with measurements [133–136].

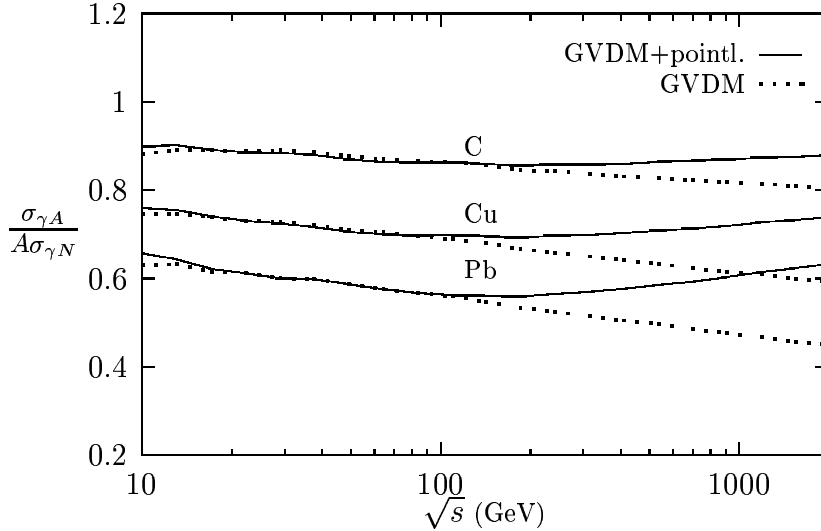


Figure 2.16: Extrapolation in energy of per-nucleon cross section ratios for photoproduction off carbon-, copper- and lead-nuclei (solid lines). The pure GVDM-predictions are shown as dotted lines.

transversely polarized photons per incident muon is estimated according to the equivalent photon approximation (EPA) [74]

$$g(y, Q^2) = \frac{\alpha_{\text{em}}}{2\pi Q^2} \left( \frac{1 + (1-y)^2}{y} - \frac{2m_\mu^2 y}{Q^2} \right) \quad (2.75)$$

where  $y$  denotes the fraction of the lepton energy transferred to the photon. In order to calculate the values of the kinematic variables this flux approximation has to be folded with the  $Q^2$ -dependent cross section  $\sigma_{\gamma^* A}$ . In addition, the experimental trigger conditions are taken into account within the calculation. In Fig. 2.17, the  $x$ -dependence of calculated shadowing ratios is compared to data [68,137,138]. The average  $Q^2$ -values range from

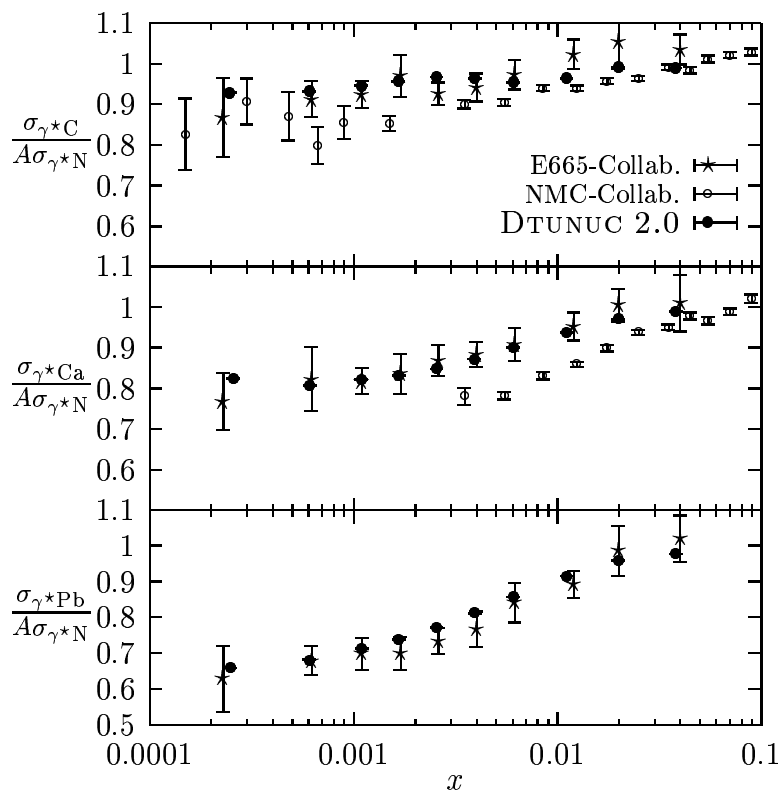


Figure 2.17: *Dependence of the per-nucleon cross section ratios of photon-carbon, -calcium and -lead interactions on Bjorken- $x$ . Model predictions are compared to data of the E665- [68] and NMC-Collaborations [137,138].*

0.15 GeV<sup>2</sup> in the lowest  $x$ -bin up to 7.9 GeV<sup>2</sup> in the highest bin. The calculations for the three target nuclei carbon, calcium and lead are in good agreement with the E665-data but overestimate the NMC-data slightly.

The  $Q^2$ -dependence of the cross section ratios at fixed  $x$  is often studied by parametrizing  $R_{\gamma^*A}$  as

$$R_{\gamma^*A}(Q^2) = a + b \cdot \log(Q^2/\text{GeV}^2) . \quad (2.76)$$

In Fig. 2.18, the slope  $b$  is plotted as function of  $x$  together with E665-data [68] on photon-calcium scattering. The results of the model are consistent with experimental observations [68], i.e. with a very weak  $Q^2$ -dependence of the shadowing effect within the considered  $x$ -range.

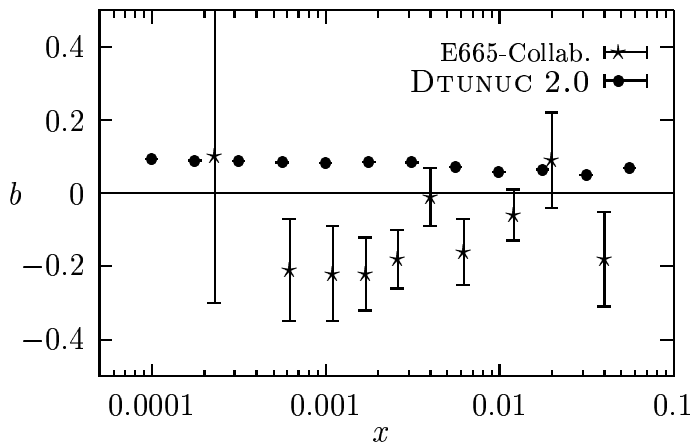


Figure 2.18: *The calculated slope of  $R_{\gamma^*Ca}$  is compared to results of the E665-Collab. [68].*

The dependence of nuclear shadowing on the target mass number  $A$  is usually inves-

tigated by parametrizing the per-nucleon cross section ratios as  $R_{\gamma^*A} \propto A^{\alpha-1}$ . Simple geometrical considerations yield  $\alpha = 2/3$  for absorption on a black disk corresponding to complete shadowing. Hence actual values for  $\alpha$  can be expected to be in the range between  $2/3$  and 1 (no shadowing). In Fig. 2.19 model results on the  $x$ -dependence of  $\alpha$

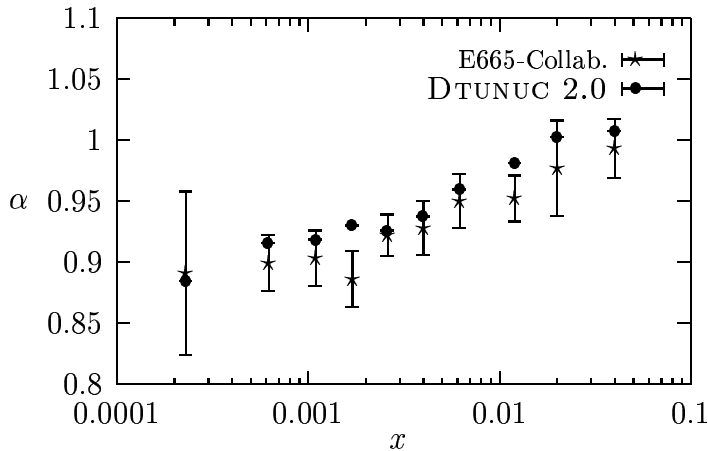


Figure 2.19: The calculated  $A$ -dependence of the per-nucleon cross section ratios is shown as function of the Bjorken- $x$  together with E665-data [68]. The  $\alpha$ -values are obtained from fits to results for carbon, calcium and lead nuclei.

are compared to E665-data [68]. Though the calculated values are systematically larger than the measured averages the  $x$ -dependence is qualitatively well understood within the model.

Finally, it is important to note that with rising energy but at fixed photon virtuality (corresponding to the limit  $x \rightarrow 0$ ) the model predicts a decrease of shadowing. This feature is shown in Fig. 2.20 for carbon and lead targets and different  $Q^2$ -values. Within

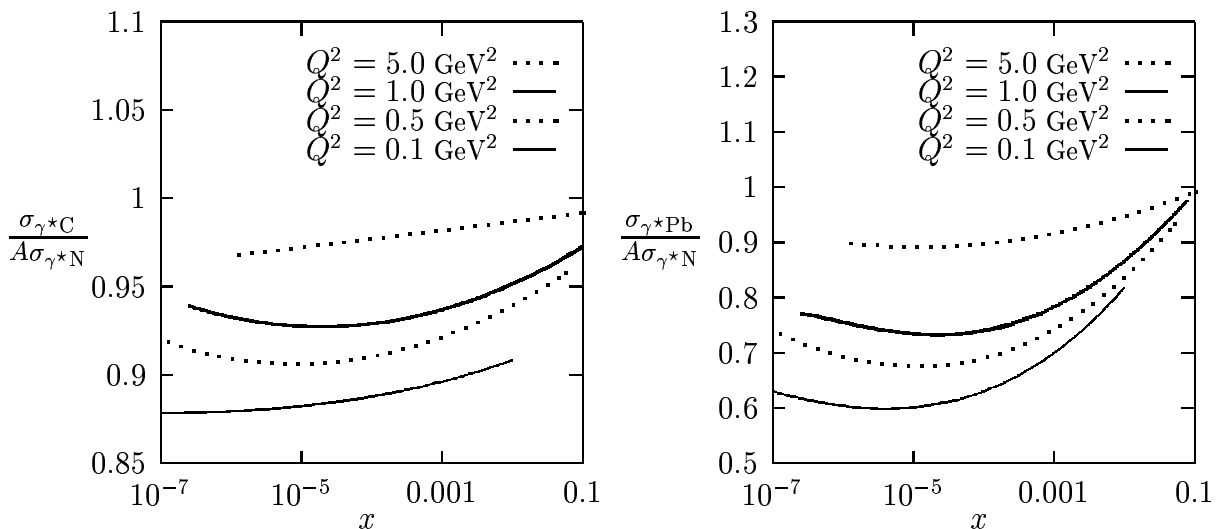


Figure 2.20: Dependence of the per-nucleon cross section ratios for carbon and lead targets on the Bjorken- $x$ . Each line corresponds to a calculation for a certain, fixed photon virtuality (from the bottom to the top:  $Q^2 = 0.1, 0.5, 1.0, 5.0 \text{ GeV}^2$ ).

the model it arises from the fact that soft contributions to the cross section are stronger suppressed with  $Q^2$  than point-like contributions. These qualitative results do not change

even if an energy-dependent transverse momentum cutoff  $p_{\perp}^{\text{cut}}(s)$  is used in the estimation of the point-like cross sections. A transverse momentum cutoff slowly rising with energy is suggested [30,139] in order to ensure that calculations in the TeV-c.m. energy range are restricted to a kinematic region where lowest order perturbative QCD estimates are sufficient. However, the energy dependence of  $p_{\perp}^{\text{cut}}$  is too weak to cause any change in the shadowing behavior shown in Fig. 2.20. Similar results for the shadowing ratios at high energies and fixed large photon virtualities were also reported by Kopeliovich and Povh [140], however, obtained within a different approach.

### 2.4.5 Quasi-Elastic Vector Meson Production

The dependence of quasi-elastic vector meson production on the photon virtuality provides a further test of the assumptions underlying the model. For example, the cross section for the quasi-elastic  $\rho^0$ -production off a nucleus with mass number  $A$  depends on  $Q^2$  like

$$\sigma_{\gamma^* A \rightarrow \rho^0 A}(s, Q^2) \sim \left( \frac{m_{\rho}^2}{m_{\rho}^2 + Q^2} \right)^2 \left( 1 + \epsilon \frac{Q^2}{m_{\rho}^2} \right) \sigma_{\rho^0 A}^{\text{el}}(s, Q^2) \quad (2.77)$$

where the elastic  $\rho^0$ -nucleus cross section  $\sigma_{\rho^0 A}^{\text{el}}$  is obtained from Eq.(2.62) with  $V = \rho^0$ . In Fig. 2.21 results are shown together with data of the NMC-Collab. [141]. For each

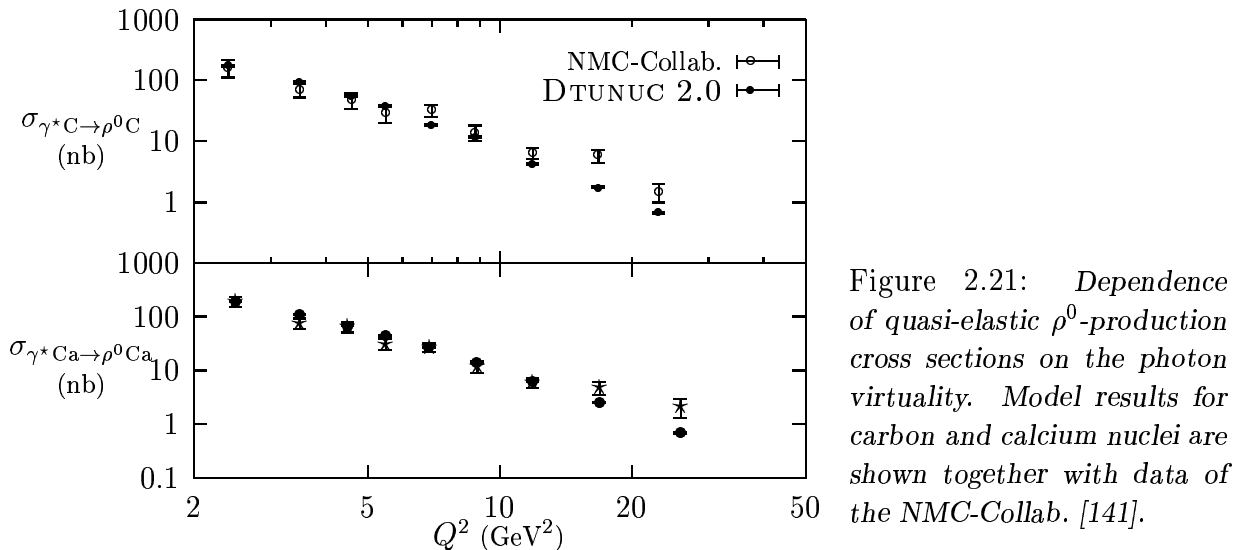


Figure 2.21: Dependence of quasi-elastic  $\rho^0$ -production cross sections on the photon virtuality. Model results for carbon and calcium nuclei are shown together with data of the NMC-Collab. [141].

$Q^2$ -value the cross section has been calculated for the experimentally determined average photon energy and polarization  $\epsilon$ . In order to compare shapes, the model results are normalized to the data. Parametrizing  $\sigma_{\rho^0 A}^{\text{el}}$  by

$$\sigma_{\rho^0 A}^{\text{el}}(Q^2) = \sigma_0 \left( \frac{Q_0^2}{Q^2} \right)^\beta \quad (2.78)$$

fits to the calculated cross sections yield  $\beta$ -values of 2.5 for carbon and 2.4 for calcium. Since the calculated  $Q^2$ -dependence slightly deviates from a power-law behavior uncertainties are estimated by excluding either the cross sections at the two lowest or the two highest photon virtualities from the fit. This results in an estimated uncertainty of  $\pm 0.2$

for both  $\beta$ -values. The  $Q^2$ -dependence obtained within the model has to be compared to the result from a combined fit to the data giving  $\beta = 2.02 \pm 0.07$  [141]. Reasons for the deviation of the calculated from the measured  $Q^2$ -dependence might be the following: In the model  $\rho$ ,  $\omega$  and  $\phi$  vector mesons are not explicitly treated but instead are included into the mass continuum (Eq.(2.51)). If they were considered separately, a better agreement between data and model results could be expected. However, in this case new parameters would have to be introduced into the model which are not needed within the description of multiparticle photoproduction discussed further below. Furthermore it should be noted that the values of the kinematic variables  $s$  and  $Q^2$  in the NMC-experiment partially exceed the region  $Q^2 \ll s$  where this approach is expected to be reliable.

## 2.5 A Model for Multiparticle Photoproduction off Nuclei

According to the Gribov–Glauber approximation, photon–nucleus collisions are described in terms of individual photon–nucleon interactions. Multiparticle production in photon–nucleon interactions within the two-component DPM has been discussed in Sec. 2.3. Therefore in this section emphasis is put on additional ingredients which are necessary for the extension to nuclear targets and on the main steps of inelastic event generation.

With Eqs.(2.51), (2.63), (2.72) and the treatment of point-like processes, the inelastic photon–nucleus cross section can be written as

$$\sigma_{\gamma^*A}^{\text{inel}}(s, Q^2) = \int d^2\vec{B} T_{\gamma^*A}(s, Q^2, \vec{B}) + A \sigma_{\gamma^*N}^{\text{pl}}(s, Q^2) \quad (2.79)$$

where the profile function  $T_{\gamma^*A}$  reads

$$T_{\gamma^*A}(s, Q^2, \vec{B}) = 4\pi\alpha_{\text{em}} \int_{M_0^2}^{M_1^2} dM^2 D(M^2) \left( \frac{M^2}{M^2 + Q^2} \right)^2 \left( 1 + \epsilon \frac{Q^2}{M^2} \right) \sigma_{VA}^{\text{inel}}(s, Q^2, M^2, \vec{B}) . \quad (2.80)$$

The effective inelastic  $q\bar{q}$ -nucleus cross section at impact parameter  $\vec{B}$  follows from Eq.(2.63) by inserting Eqs.(2.64) and (2.69)

$$\sigma_{VA}^{\text{inel}}(s, Q^2, M^2, \vec{B}) = \int \prod_{j=1}^A d^3r_j \rho_A(\vec{r}_j) \left( 1 - \left| \prod_{\nu=1}^A \left( 1 + 2ia_{VN}(s, Q^2, M^2, \vec{B}_\nu) \right) \right|^2 \right) . \quad (2.81)$$

Note that  $T_{\gamma^*A}$  does not include point-like processes which is accounted for by the additional factor  $1 - \xi$  contained in the  $q\bar{q}$ -nucleon amplitude  $a_{VN}$ .

Alternatively,  $\sigma_{VA}^{\text{inel}}$  might be expressed in terms of eikonal functions. Writing  $\sigma_{VA}^{\text{inel}}$  in the form

$$\sigma_{VA}^{\text{inel}}(s, Q^2, M^2, \vec{B}) = \int \prod_{j=1}^A d^3r_j \rho_A(\vec{r}_j) \sum_{k_1+\dots+k_A \geq 1} \sigma_{k_1, \dots, k_A}(s, Q^2, M^2, \vec{B}_1, \dots, \vec{B}_A) \quad (2.82)$$

the quantities  $\sigma_{k_1, \dots, k_A}$  can be interpreted as the partial cross section for processes with  $k_\nu$  inelastic collisions with nucleon  $\nu$  ( $\nu = 1 \dots A$ )

$$\sigma_{k_1, \dots, k_A}(s, Q^2, M^2, \vec{B}_1, \dots, \vec{B}_A) =$$

$$\prod_{\nu=1}^A \frac{(2\Re \chi_{VN}(s, Q^2, M^2, \vec{B}_\nu))^{k_\nu}}{k_\nu!} \exp[-2\Re \chi_{VA}(s, Q^2, M^2, \vec{B}_1, \dots, \vec{B}_A)] . \quad (2.83)$$

Here, the eikonal function  $\chi_{VN}$  includes the factor  $(1 - \xi)$  (see also Eq.(2.67)).

In order to keep the expressions short low-energy coherence length effects have been omitted in Eqs.(2.79–2.83). However, in actual event generation they are considered as described in Sec. 2.4.3 and also further below.

The generation of a photon–nucleus particle production event proceeds as follows:

1. The treatment of each event starts with sampling of an initial spatial configuration of nucleons according to nuclear densities (for example, for  $A > 4$  from the Woods-Saxon density distributions Eq.(2.65) [129]) and of Fermi-momenta of nucleons (see Eq.(4.8) further below).
2. The impact parameter  $\vec{B}$  of the photon–nucleus collision is sampled from the pre-tabulated distribution  $T_{\gamma^*A}$ .
3. A mass  $M$  is assigned to the hadronic fluctuation according to the mass-dependent part of the integrand in Eq.(2.80).
4. The photon interacts with a probability  $A\sigma_{\gamma^*N}^{\text{pl}}/\sigma_{\gamma^*A}^{\text{tot}}$  as a point-like object. Hence in this fraction of all photon–nucleus interactions and corresponding to the cross sections  $\sigma_{\gamma^*N}^{\text{dir}}$  and  $\sigma_{\gamma^*N}^{\text{ano}}$ , either a direct process or an anomalous (hard resolved) scattering with one nucleon is generated.
5. The probability for the interaction of the hadronic fluctuation with the  $\nu$ th nucleon ( $\nu = 1 \dots A$ ) follows from the profile function  $T_{VN}$  of the  $q\bar{q}$ –nucleon interaction

$$\begin{aligned} \sigma_{VN}^{\text{inel}}(s, Q^2, M^2) &= \int d^2\vec{B} T_{VN}(s, Q^2, M^2, \vec{B}) \\ &= \int d^2\vec{B} \left(1 - |1 + 2ia_{VN}(s, Q^2, M^2, \vec{B})|^2\right) . \end{aligned} \quad (2.84)$$

The hadronic fluctuation of mass  $M$  undergoes an inelastic scattering with nucleon  $\nu$  (at a transverse distance  $|\vec{B}_\nu|$ ) according to the probability  $P_\nu = T_{VN}(\dots, \vec{B}_\nu)$ . Here, only inelastic events are of interest. Therefore at least one nucleon is selected. As a result, the number of so-called “wounded” nucleons is obtained.

6. It is checked that the coherence length of the hadronic fluctuation (Eq.(2.5)) allows the sampled Gribov–Glauber cascade. If the longitudinal distance between any of the previously determined nucleons exceeds the coherence length a subset of wounded nucleons is selected for the further event generation which fulfills this condition.
7. Particle production in direct processes or in inelastic  $q\bar{q}$ –nucleon interactions is treated according to the PHOJET-realization of the two-component DPM described in Sec. 2.3. In the present approximation, low- and high-mass single and double diffractive processes are considered for one wounded nucleon only. In all other cases only non-diffractive multiple soft and hard pomeron cuts are allowed. For example,

for any of the non-diffractive  $q\bar{q}$ -nucleon scatterings the numbers of cut soft and hard pomerons is sampled as discussed in Sec. 2.3.2. They might be considered as the maximum numbers of cut pomerons in the particular event since the actual contributing numbers are biased by energy-momentum conservation. In general, first it is tried to generate as many of the sampled number of hard scatterings as kinematically possible. The remaining phase space is then used by the soft interactions, i.e. by strings between valence partons (if they were not involved in hard scatterings) and sea partons. For example, if  $n_h$  hard interactions have been generated in total (say, non of them involving valence quarks), the momentum fractions of the  $n_s$  sea and valence partons of the  $q\bar{q}$ -fluctuation (belonging to hard scattering remnants and to cut soft pomerons) are sampled from the distribution (c.f. Eq.(2.45))

$$\rho(x_1, \dots, x_{n_s}) \sim \frac{1}{\sqrt{x_1 x_2}} \prod_{i=3}^{n_s} \frac{1}{x_i} \delta \left( \sum_{i=1}^{n_s} x_i + \sum_{j=n_s+1}^{n_s+n_h} x_j - 1 \right). \quad (2.85)$$

Here,  $x_{n_s+1}, \dots, x_{n_s+n_h}$  are the fractions of the momentum of the  $q\bar{q}$ -system going into the hard scatterings. Additionally, further constraints are imposed. For instance, the invariant mass of a string has to be larger than the lowest mass of a hadronic state to which the quantum numbers of the quarks at the string ends correspond. All color neutral strings are finally hadronized by means of the JETSET-code [106,107] which is based on the Lund-model.

8. The inelastic event generation is followed by a formation zone intranuclear cascade and a subsequent treatment of prefragments as described in Chapter 4.

It should be noted that only the main steps of inelastic event generation are listed. Further mechanisms, such as multiple scattering of partons at string ends in the nuclear medium (Cronin effect [142]), are implemented [143–145].

The formulation of the two-component DPM for photon–nucleus collisions as discussed so far is realized in form of the MC event generator DTUNUC 2.0. This event generator for hadron–, photon– and nucleus–nucleus collisions is based on its previous version 1.04 [145,146,48]. DTUNUC 2.0 includes the event generator PHOJET [32,33] for the description of individual photon–nucleon or hadron–nucleon scatterings. In comparison to DTUNUC 1.04 the following new features are incorporated:

- The model allows the description of cross sections and multiparticle production in high-energy collisions of real and weakly virtual photons with nuclei [36,37].
- Particle production in each photon–, hadron– and nucleon–nucleon interaction is based on the two-component DPM, i.e. it includes multiple soft and hard pomeron exchanges.
- A formation zone intranuclear cascade is performed in both, the projectile and target spectators in a consistent way (see Chapter 4). Excitation energies of prefragments are calculated and their further disintegration is treated. This disintegration includes evaporation of nucleons and light nuclei from excited spectators, spectator de-excitation via photon-emission, high-energy fission and fragmentation of light spectator nuclei [56,57].

## 2.6 Comparison of Model Predictions with Data on Particle Production

One of the basic assumptions underlying the application of the two-component DPM to photon–nucleus collisions is that the mechanisms of soft hadronic multiparticle production exhibit universal features irrespective of the nature of the colliding particles. This fact was already emphasized before, for example by Engel and Ranft in [32,33] where the description of high-energy hadron–hadron interactions based on the two-component DPM was extended to photon–hadron and photon–photon interactions.

The same assumptions are applied in DTUNUC. As demonstrated in [32–34] hadron–hadron and photon–hadron collisions are well understood within the model. From the comparisons with data shown in [33,37] a few ones have been selected and are discussed in the following. Furthermore the model is also able to reproduce most features of final states in hadron–nucleus collisions (see for example [55,143,24,31,37]). Again, only a few comparisons between DTUNUC results and data on inclusive particle cross sections are chosen and discussed in this section. Relying on the predictive power of the model it is then applied to multiparticle photoproduction off nuclei where the experimental information is still sparse.

### 2.6.1 Photon–Hadron Collisions

Transverse momentum distributions of charged hadrons in photon–proton interactions have been measured by the OMEGA-Collab. [147]. The data were obtained with a tagged photon beam in the energy band 110–170 GeV. In Fig. 2.22 model results using the average photon laboratory energy of 140 GeV are compared to these data in four different Feynman- $x$  bins (from the top to the bottom:  $0.0 < x_F < 0.2$ ,  $0.2 < x_F < 0.4$ ,  $0.4 < x_F < 0.6$  and  $0.6 < x_F < 0.8$ ). The figure demonstrates that the data are very well described up to  $x_F = 0.6$  whereas at higher  $x_F$ -values ( $0.6 < x_F < 0.8$ ) the calculation overestimates

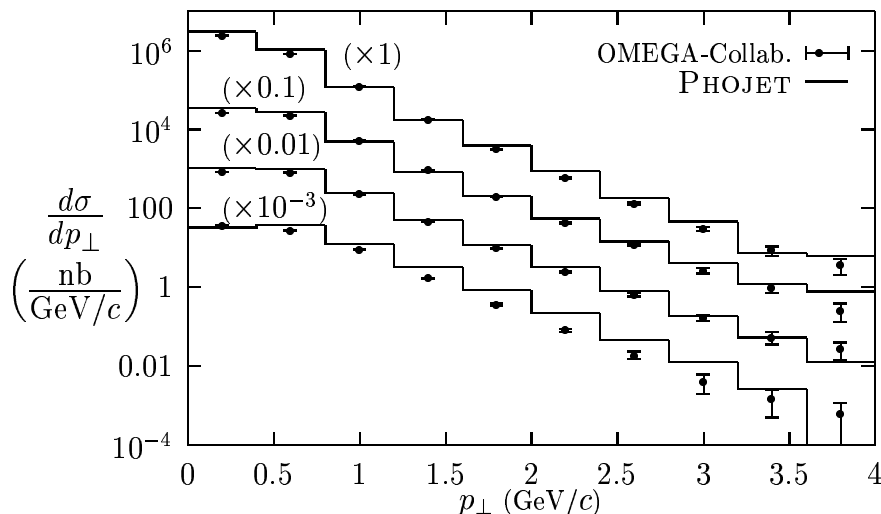


Figure 2.22: *Transverse momentum distributions of charged hadrons calculated for photon–proton collisions at an average photon laboratory energy of 140 GeV are compared to data [147]. Results are shown for different  $x_F$ -bins (see text).*

the data slightly. However, in this  $x_F$ -bin the distribution might be biased by the method applied in the experimental analysis to subtract the forward-scattered  $\rho^0$  mesons [147].

Feynman- $x$  distributions are usually studied in terms of the one-particle inclusive variable  $F(x_F)$  defined as

$$F(x_F) = \frac{1}{\sigma_{\gamma p}^{\text{tot}}} \frac{2E}{\pi W} \frac{d\sigma}{dx_F}, \quad x_F = \frac{2p_{\parallel}}{W}. \quad (2.86)$$

$E$ ,  $p_{\parallel}$  and  $W = \sqrt{s}$  denote the energy and longitudinal momentum of the final state

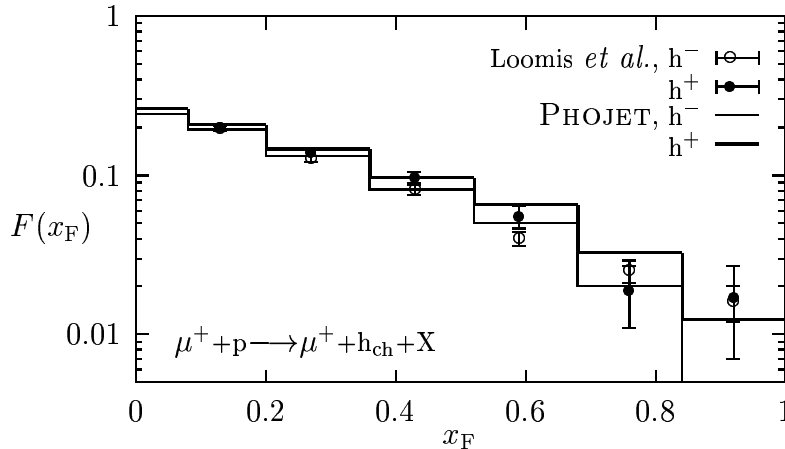


Figure 2.23: Invariant Feynman- $x$  distributions of charged hadrons from muon-proton interactions at  $E_{\mu} = 147$  GeV. Model results are shown together with data [148].

particle in the photon-proton c.m. system and the c.m. energy, respectively. In Fig. 2.23 the distribution  $F(x_F)$  is plotted for positively and negatively charged hadrons from interactions of 147 GeV muons with a proton target. The calculated distributions are compared to data [148]. Within the calculations the flux of virtual photons radiated by the muons is approximated based on the EPA (Eq.(2.75)) folded with  $Q^2$ -dependent photon-proton cross sections. According to the kinematic limits imposed on the data the photon virtuality is restricted to  $0.5 < Q^2 < 3$  GeV<sup>2</sup> and the c.m. energy of the virtual photon-proton system has to exceed 10 GeV. There is again a reasonable agreement of model results and experimental data.

## 2.6.2 Hadron-Nucleus Collisions

Average multiplicities of singly charged particles (Lorentz- $\beta > 0.7$ , so-called shower particles) produced in interactions of pions and protons with carbon, copper and lead targets are given in Table 2.1. For all configurations and studied energies a reasonable agreement between calculated and measured values [149] is found.

In addition to the average values, also their distributions in hadron-nucleus collisions are well described. For example, we shown in Fig. 2.24 the distribution of charged hadron multiplicities in interactions of 525 GeV pions in nuclear emulsion together with data [150]. Here, the common chemical composition is used: about 28.6% light nuclei (H,C,N,O) and 71.4% heavy nuclei (Ag, Br).

Pseudorapidity distributions of shower particles have been calculated again for pion-emulsion interactions, now for the two laboratory energies of 60 GeV and 525 GeV and for pion-lead collisions at 50 GeV. The results are given in Fig. 2.25 together with measured distributions [150,149]. In all cases, the data are well reproduced by the model.

Data on invariant  $\pi^0$ -production cross sections as function of the transverse momentum have been published by the WA80-Collab. [151] for proton-gold collisions at 200 GeV.

	$E_{\text{Lab}}=50$ GeV		$E_{\text{Lab}}=100$ GeV		$E_{\text{Lab}}=150$ GeV	
	DTUNUC	Exp.	DTUNUC	Exp.	DTUNUC	Exp.
$\pi^+$ -C	7.3	$7.62 \pm 0.14$	9.0	$9.19 \pm 0.17$	9.9	$10.01 \pm 0.18$
$\pi^+$ -Cu	8.6	$8.81 \pm 0.23$	10.5	$10.41 \pm 0.27$	11.8	$11.57 \pm 0.30$
$\pi^+$ -Pb	10.1	$10.11 \pm 0.38$	12.2	$11.54 \pm 0.44$	14.3	$13.08 \pm 0.50$
p-C	7.7	$7.88 \pm 0.15$	9.2	$9.25 \pm 0.18$	10.3	$10.58 \pm 0.19$
p-Cu	9.8	$9.52 \pm 0.24$	11.9	$11.40 \pm 0.29$	13.3	$12.93 \pm 0.33$
p-Pb	11.1	$11.31 \pm 0.43$	13.8		15.9	$14.95 \pm 0.57$

Table 2.1: Multiplicities of shower particles ( $\beta > 0.7$ ) in interactions of pions and protons with carbon-, copper- and lead-nuclei are compared to measurements [149].

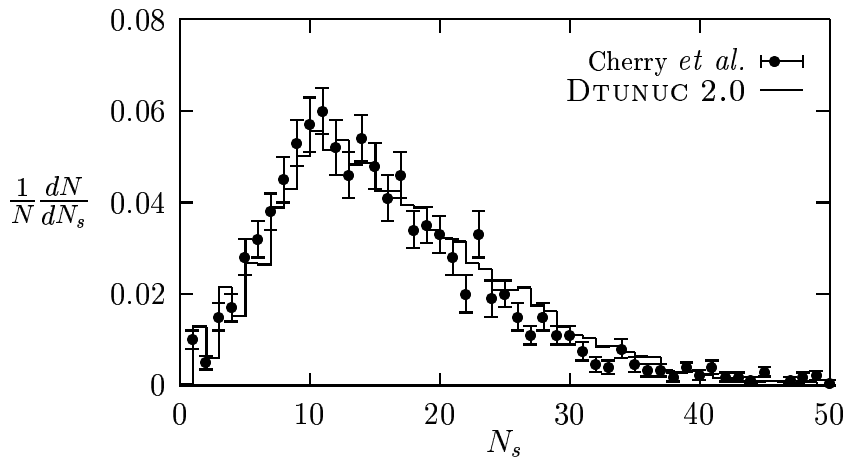


Figure 2.24: Multiplicity distribution of shower particles in pion-emulsion interactions at  $E_{\text{Lab}} = 525$  GeV. Results from DTUNUC are compared to experimental data [150].

In Fig. 2.26a calculation results are compared to these data. Corresponding to the experimental trigger conditions only neutral pions in the pseudorapidity range  $1.5 \leq \eta \leq 2.1$  are included in the plot. The transverse momentum distribution of negatively charged hadrons from proton-tungsten collisions at 200 GeV is studied in Fig. 2.26b. Here, particles with rapidities between 1.0 and 1.9 are considered. In order to compare the shape with experimental results [152] and because of the particular normalization of these data, they were normalized to the calculated value at 0.16 GeV/c. As these comparisons demonstrate also transverse momentum distributions are understood within the model.

Finally, in Fig. 2.27 we compare calculated inclusive cross sections for the production of negative pions (a) and of positive kaons (b) as function of  $x_F$  to data from proton-carbon and proton-copper interactions at 100 GeV [153]. The measured cross sections include only particles with transverse momenta of 0.3 GeV/c. From the calculated final state, pions and kaons with  $0.25 < p_{\perp} < 0.35$  GeV/c were taken into consideration. In most of the studied  $x_F$ -range the agreement is satisfactorily. At large  $x_F$ -values ( $x_F > 0.7$ ) significant statistical uncertainties within both, the data and the calculations, do not allow to draw any conclusions.

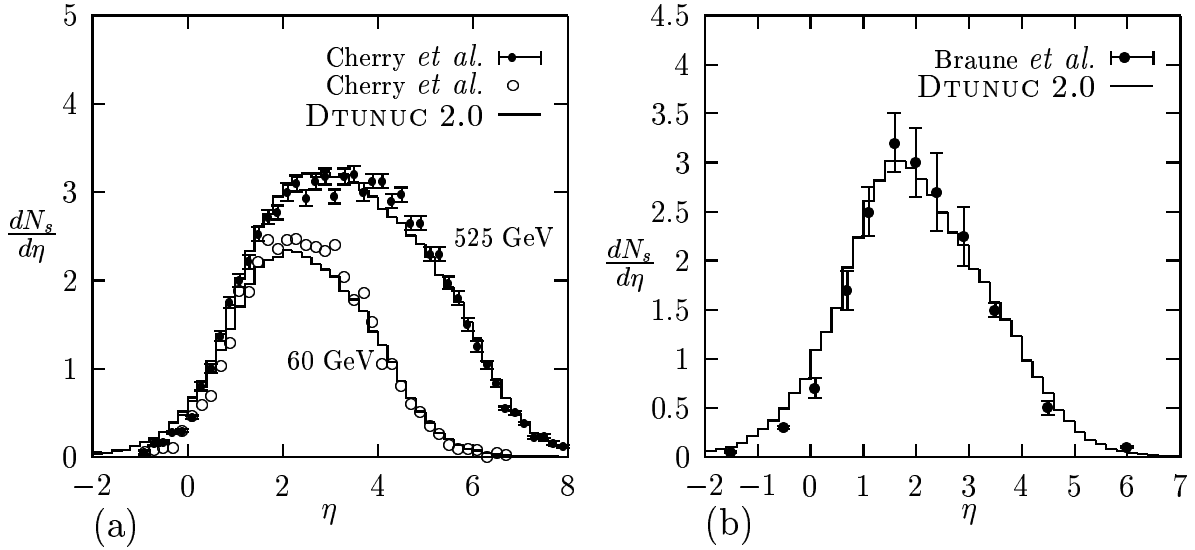


Figure 2.25: Pseudorapidity distributions of shower particles in pion–nucleus interactions: In a) the model results are given for pion–emulsion interactions at  $E_{Lab} = 60$  GeV and  $525$  GeV and are compared to measurements [150]. In b) they are shown for pion–lead interactions at  $50$  GeV together with data [149].

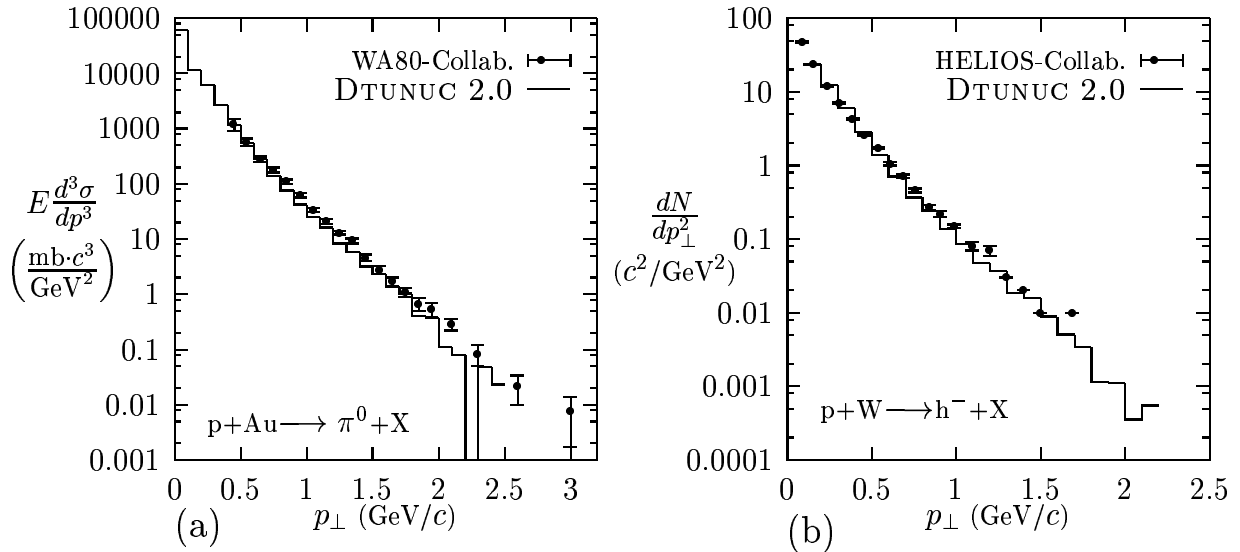


Figure 2.26: Transverse momentum distributions in proton–nucleus interactions at  $200$  GeV: In a) results of the model are shown together with data [151] on neutral pions from proton–gold collisions. In b) the transverse momentum distribution of negatively charged particles from proton–tungsten collisions is compared to data [152].

### 2.6.3 Photon–Nucleus Collisions

#### Average multiplicities

Experimental information on multiplicities in the kinematic range under investigation in this chapter is available from lepton–nucleus interactions. Of course, the energy and

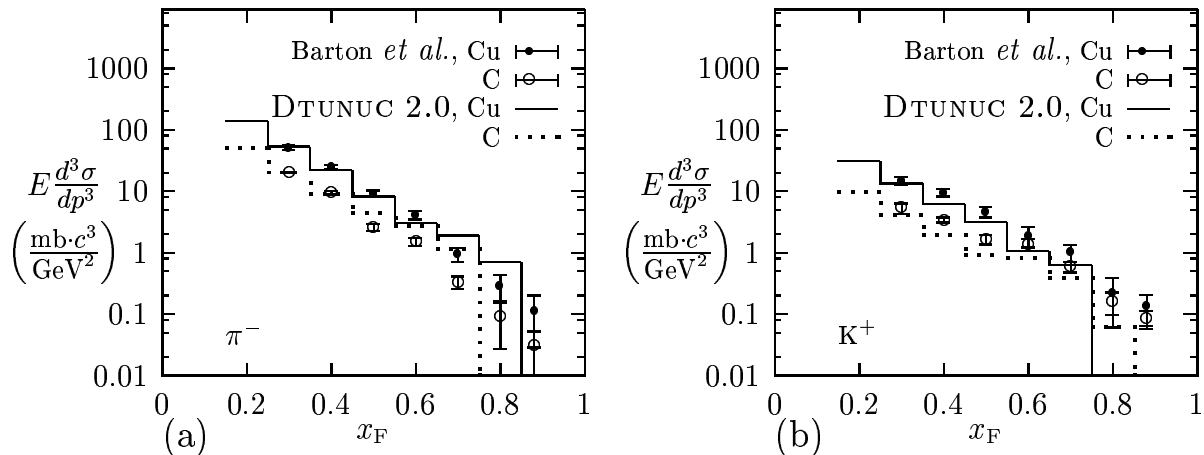


Figure 2.27: Model results on Feynman- $x$  distributions of negatively charged pions (a) and positively charged kaons (b) from proton-carbon and proton-copper interactions at  $E_{\text{Lab}} = 100$  GeV are compared to data [153].

virtuality of the photon radiated by the lepton varies within the limits imposed by the trigger conditions and the data represent multiplicities of photon-nucleus collisions which are weighted with the photon flux and integrated over energy. Before testing the model against these data it might be, however, interesting to study differences in the particle production mechanisms between photon- and hadron-nucleus collisions, both at the same projectile energy.

In Fig. 2.28 average numbers of target nucleons interacting with the projectile  $\langle\nu_t\rangle$  as

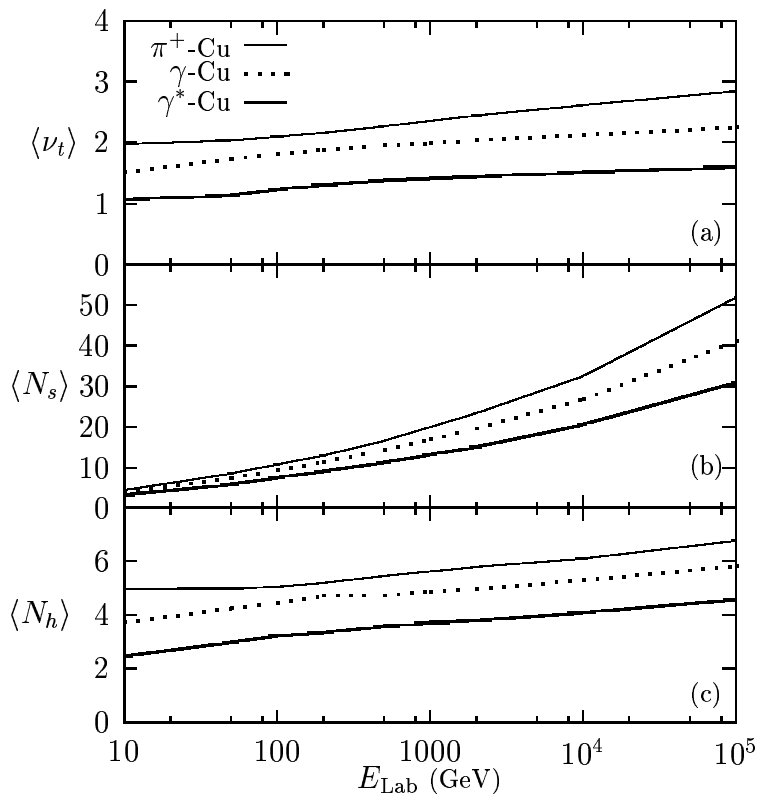


Figure 2.28: Average numbers of copper nucleons  $\langle\nu_t\rangle$  struck by pions, real photons and virtual photons ( $Q^2 = 2$  GeV $^2$ ) are given as function of the projectile laboratory energy (a). In b) and c) average multiplicities of shower  $\langle N_s\rangle$  and heavy particles  $\langle N_h\rangle$  are shown.

well as multiplicities of shower  $\langle N_s \rangle$  and heavy particles  $\langle N_h \rangle$  are given for pion-, real photon- and weakly virtual photon-copper interactions as a function of the projectile energy in the nucleus rest frame. Again, shower particles are defined as singly charged hadrons satisfying the condition  $\beta > 0.7$ . All other charged particles and light fragments (except residual copper nuclei) are grouped together as heavy particles. Differences between the  $\langle \nu_t \rangle$ -values for pion and photon projectiles at fixed energy arise from differences between the pion-nucleon cross section and the  $q\bar{q}$ -nucleon cross section  $\sigma_{VN}$  (Eq.(2.58), averaged over all masses  $M$ ). Since the latter is slightly smaller, the real photon interacts on average with less nucleons than the pion. As it will be discussed in Chapter 4,  $\langle N_h \rangle$  includes the nucleons interacting with the projectile ( $\langle \nu_t \rangle$ ) and with secondary particles as well as nucleons and fragments from the disintegrating spectator. The number of these particles is strongly correlated with  $\langle \nu_t \rangle$ . Therefore  $\langle N_h \rangle$  shows a similar (weak) energy dependence as  $\langle \nu_t \rangle$  whereas  $\langle N_s \rangle$  rises rapidly with energy. Furthermore due to the approximate  $1/Q^2$ -dependence of  $\sigma_{VN}$ ,  $\langle \nu_t \rangle$  decreases with  $Q^2$  at fixed energy. For example, this is shown in Fig. 2.29a for photon-copper interactions at a photon-nucleon

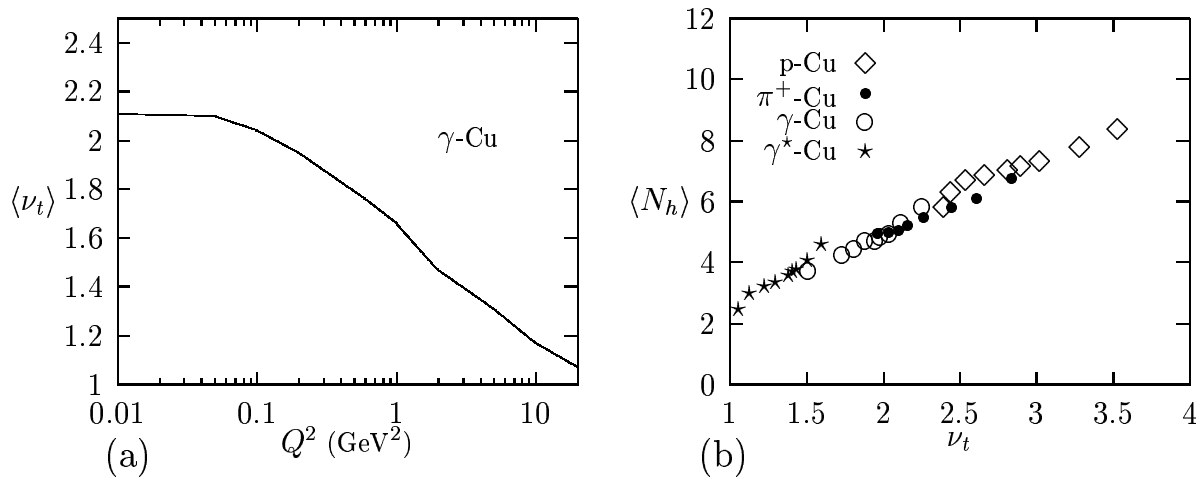


Figure 2.29: In a) the  $Q^2$ -dependence of the average number of copper nucleons interacting with the photon  $\langle \nu_t \rangle$  is given for a photon-nucleon c.m. energy of 150 GeV. In b) the dependence of the average heavy particle multiplicity on  $\nu_t$  is shown for proton, pion, real photon and weakly virtual photon ( $Q^2 = 2 \text{ GeV}^2$ ) projectiles.

c.m. energy of 150 GeV, an energy which could be possibly available in the future for photon-nucleus collisions at HERA [59]. In the model, the average heavy particle multiplicity is approximately proportional to  $\nu_t$ , irrespectively of the nature of the projectile. This dependence is shown in Fig. 2.29b for protons, pions, real and weakly virtual photons ( $Q^2 = 2 \text{ GeV}^2$ ) interacting with copper nuclei. Again, it reflects the fact that the number of heavy particles depends only on the number of nucleons “knocked out” of the target by the projectile and by subsequent intranuclear cascade processes (see Sec. 4.1.2) and not on particular properties of the interactions of the projectile with single nucleons [56,57].

Calculated average shower particle multiplicities in interactions of 150 GeV muons in emulsions are compared to data [154] in Fig. 2.30. Corresponding to the experimental conditions, the calculated values contain only multiplicities of events with at least three heavy particles in the final state. The photon flux is again approximated according to

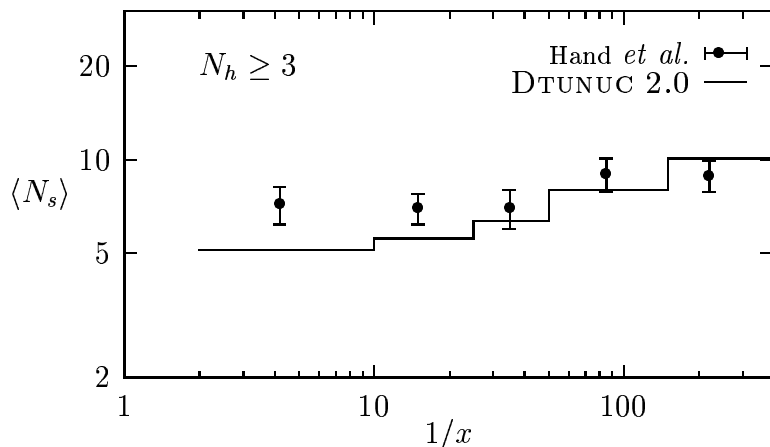


Figure 2.30: Average multiplicities of charged hadrons ( $\beta > 0.7$ ) in muon-emulsion interaction events at 150 GeV. Model results are compared to data [154].

the EPA folded with the  $Q^2$ -dependent photon-nucleus cross sections. The multiplicities are plotted as function of the inverse of the Bjorken- $x$  variable. In this representation the average photon virtuality decreases from about 8 GeV<sup>2</sup> in the lowest bin ( $1/x < 10$ ) to about 0.9 GeV<sup>2</sup> in the highest bin [154]. The calculated values agree with data in the kinematic region of photoproduction ( $Q^2 \lesssim 4$  GeV<sup>2</sup>,  $1/x > 25$ ), but underestimate the data for higher virtualities. This fact indicates that the model may fail in describing particle production in interactions with photons of relatively high virtualities at low energies, i.e. where the condition  $Q^2 \ll 2m_N\nu$  (Eq.(2.2)) is not fulfilled. However, it has to be noted that whereas the calculations are based on 50000 simulated events in total, the data include only about 17 events in each  $1/x$ -bin [154]. For this reason and taking into consideration that the emulsion is composed of 6 elements and that the kinematics at the muon-photon vertex is different in each event, the statistical significance of the data is limited.

Finally, in Fig. 2.31 calculated multiplicities from interactions of 490 GeV muons with xenon nuclei are compared to data of the E665-Collab. [155]. The limits  $Q^2 > 1$  GeV<sup>2</sup>,  $8 < W < 30$  GeV,  $x > 0.002$  and  $0.1 < \nu/E_\mu < 0.85$  (with  $\nu$  being the photon energy in the laboratory) define the considered kinematic region. Only those charged particles are included which have laboratory momenta exceeding 200 MeV/ $c$ . Note that despite of the rapidly decreasing distribution of photon virtualities towards high  $Q^2$ -values, still a considerable fraction of events falls outside of the  $Q^2$ -region where the model can be expected to be reliable. In Fig. 2.31a the energy dependence of multiplicities is shown for all and for positively and negatively charged hadrons. The measured values are well reproduced by the model. In Fig. 2.31b the multiplicities of all charged hadrons are given separately for the forward and backward direction of the photon-nucleon c.m. frame. In the xenon hemisphere (backward direction) the values are affected by target associated particle production and depend strongly on the laboratory momentum cut applied to the final state hadrons. Multiplicities averaged over all energies of the photon-nucleus interaction are compared to data [155] in Table 2.2. In addition to the results for xenon target those for deuterium are given.

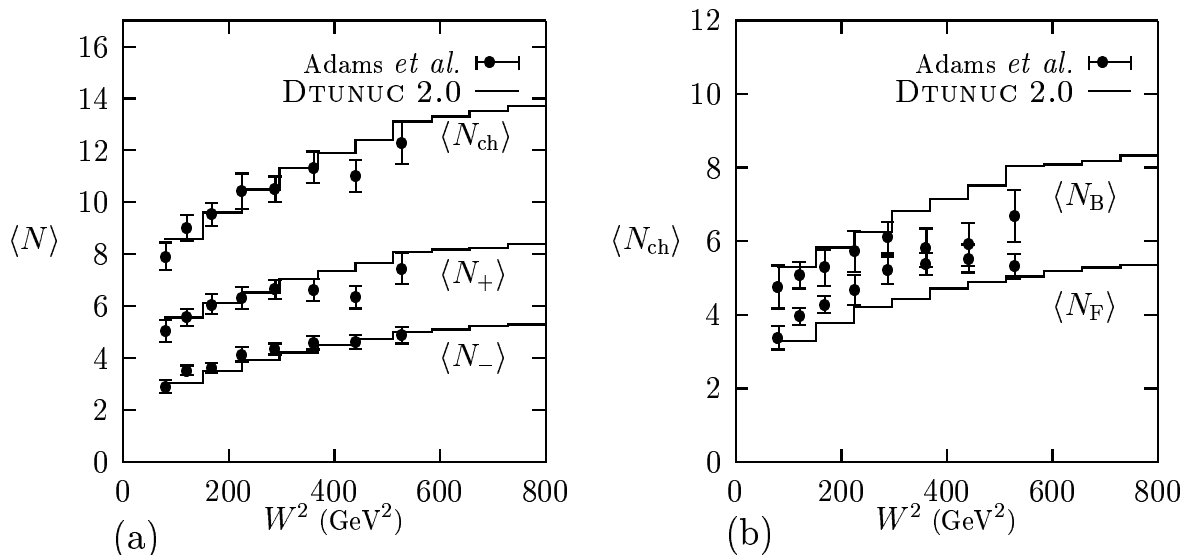


Figure 2.31: Dependence of average multiplicities of charged hadrons on the squared energy of the photon-nucleon c.m. system in muon-xenon interactions: In a) average multiplicities of all  $\langle N_{\text{ch}} \rangle$ , of positively  $\langle N_+ \rangle$  and of negatively charged hadrons  $\langle N_- \rangle$  are shown. In b) the multiplicities are given for positive  $\langle N_{\text{F}} \rangle$  and negative c.m. rapidities  $\langle N_{\text{B}} \rangle$ . Calculated multiplicities are compared to data [155].

	$\mu^+ \text{-D}_2$		$\mu^+ \text{-Xe}$	
	DTUNUC 2.0	Exp.	DTUNUC 2.0	Exp.
$\langle N_{\text{ch}} \rangle$	7.7	$7.83 \pm 0.07$	10.8	$9.99 \pm 0.13$
$\langle N_+ \rangle$	4.1	$4.16 \pm 0.05$	6.8	$6.00 \pm 0.11$
$\langle N_- \rangle$	3.6	$3.67 \pm 0.05$	4.0	$3.99 \pm 0.06$
$\langle N_{\text{F}} \rangle$	4.1	$4.60 \pm 0.05$	4.2	$4.70 \pm 0.07$
$\langle N_{\text{B}} \rangle$	3.6	$3.23 \pm 0.04$	6.6	$5.29 \pm 0.11$

Table 2.2: Average multiplicities in muon-deuterium and muon-xenon interactions at 490 GeV. Values obtained within the model are compared to data of the E665-Collab. [155].

### Inclusive particle distributions

In Fig. 2.32 pseudorapidity distributions of shower particles calculated for muon-emulsion interactions at 150 GeV are compared to data, again taken from Ref. [154]. According to the experimental conditions the kinematic limits imposed on the calculated events are  $0.6 < Q^2 < 21$  GeV<sup>2</sup> and  $9 < W \leq 16.5$  GeV. The distributions shown in a) and b) cover different but overlapping  $W$ -ranges: in a) both, data and model results, are restricted to the energy range  $9 < W < 14$  GeV and in b) to the range  $W > 10$  GeV ( $\langle Q^2 \rangle = 2.7$  GeV<sup>2</sup>). Comparing first the two data-sets, which include 43 events in a) and 47 events in b) [154], one may draw the following conclusion: In a) the measured

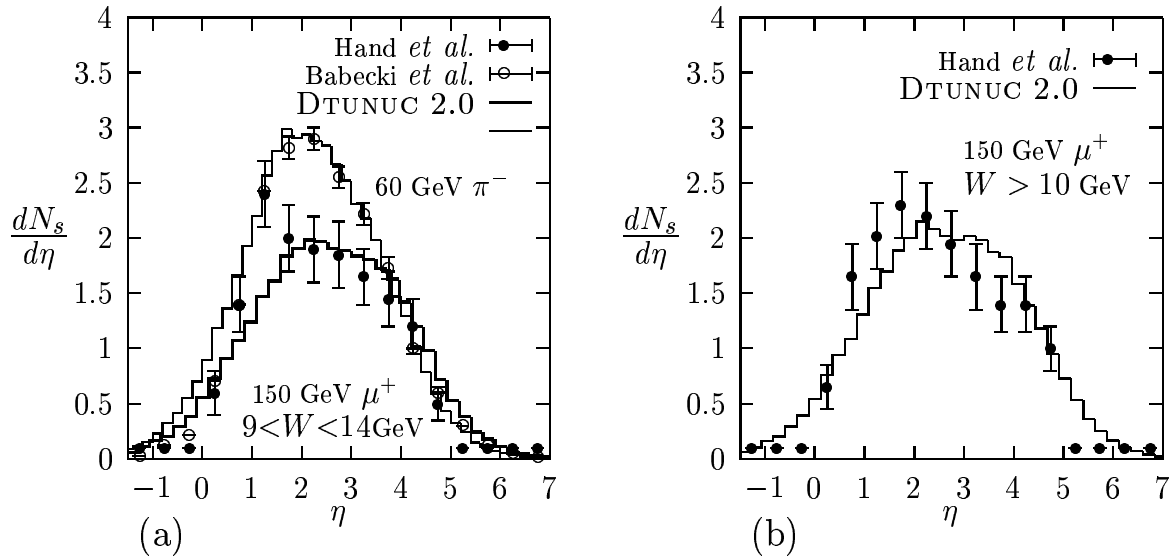


Figure 2.32: Model results on pseudorapidity distributions of charged hadrons ( $\beta > 0.7$ ) from muon–emulsion interactions at 150 GeV are shown together with data [154]. In a) the photon–nucleon c.m. energy range is restricted to  $9 < W < 14 \text{ GeV}$  (filled dots, thick histogram). In addition, the pseudorapidity distribution of charged hadrons from pion–emulsion interactions at 60 GeV is plotted (thin histogram) and compared to data [156] (open dots). In b) the results for  $W > 10 \text{ GeV}$  are given. In both distributions only events with  $N_h \geq 3$  are included.

distribution is peaked at about  $\eta = 1.25$ , an enhancement which is not present in b). On the other hand, the kinematic region of both data-sets does not overlap only in the interval  $9 < W < 10 \text{ GeV}$ . For this reason, the “peak” in a) possibly reflects statistical fluctuations within the data (c.f. also the discussion to the comparison with data from Hand *et al.* [154] in the previous section). For  $\eta > 2$  the agreement between model results and data is reasonable. Furthermore the comparison suggests that both agree in normalization (i.e. in the average multiplicity of shower particles), whereas the maximum of the calculated distribution appears at a somewhat higher pseudorapidity than the one of the data. In order to understand this discrepancy an additional comparison is shown in Fig. 2.32a. It demonstrates that for pion–emulsion interactions at 60 GeV [156] the pseudorapidity distribution is well reproduced by the model, both, in shape and in the position of the maximum. The energy of 60 GeV corresponds to the average photon laboratory energy in the muon–emulsion data-set shown in this figure. Also the cuts on both data-samples are similar: only events with at least three heavy particles in the final state are considered and the definitions of “shower particle” are identical. Therefore and with respect to conclusions drawn from comparisons with data further below we attribute the discrepancy in the position of the maximum to the statistical uncertainties of the experiment.

In Figs. 2.33 and 2.34 c.m. rapidity distributions of positively (a) and negatively charged hadrons (b) are shown for interactions of 490 GeV muons with deuterium and xenon. The model allows a satisfactory description of the data [155] except for the production of positively charged particles in the target fragmentation region of the muon–xenon interaction (Fig. 2.34a,  $y \approx -3$ ). The peak present in the calculated distribution clearly

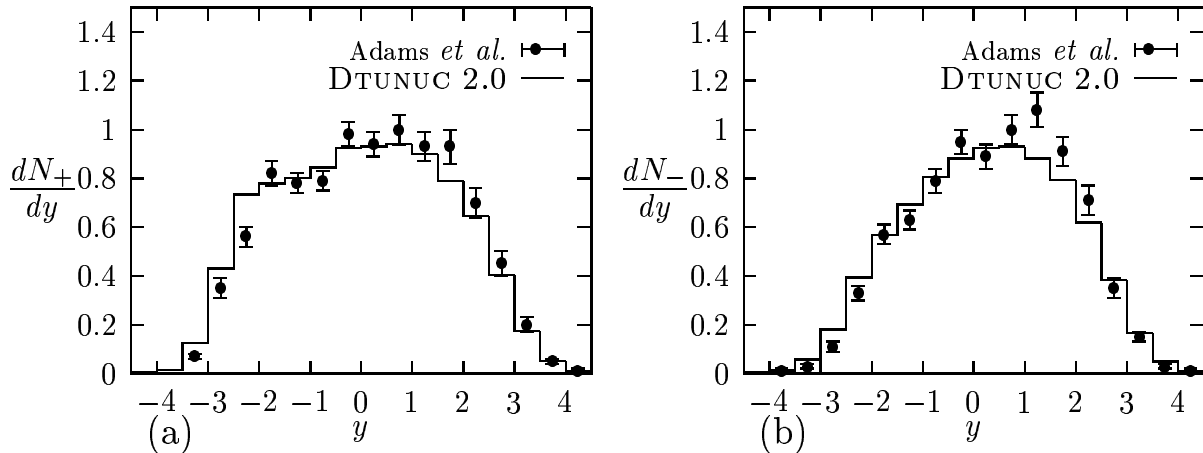


Figure 2.33: Rapidity distributions of positive (a) and negative hadrons (b) from muon-deuterium interactions at 490 GeV. Model results are compared to data in the energy range  $20 < W < 30$  GeV.

reflects the production of target associated particles by intranuclear cascade processes which, of course, appears if a momentum cut as low as 200 MeV/c in the laboratory frame is applied to the results. In general, the multiplicity seen in the target fragmentation region depends strongly on this cutoff. For the following reasons we assume that

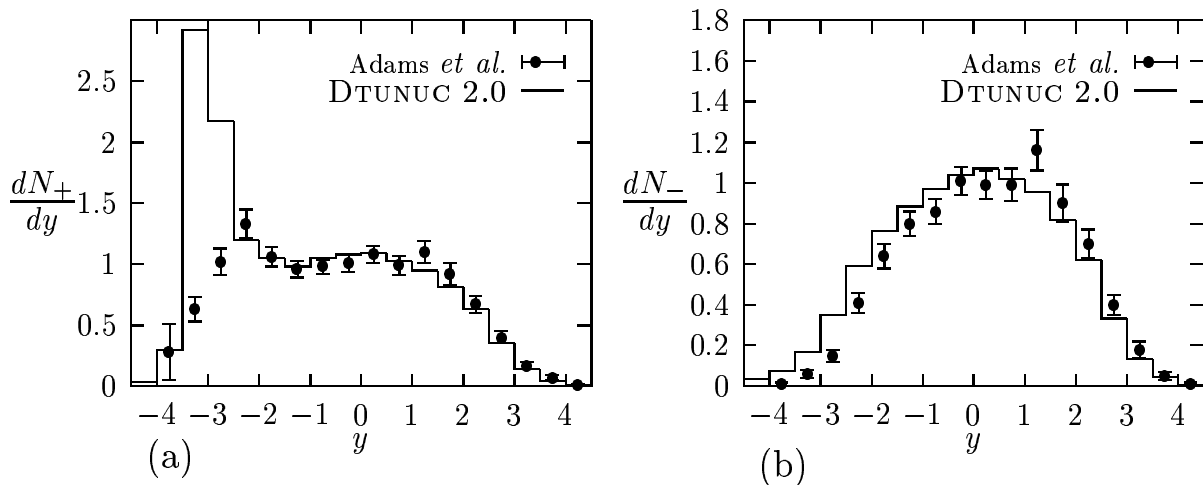


Figure 2.34: As in Fig. 2.33, here for muon-xenon interactions.

the differences might be due to additional kinematic cuts applied to the data or due to experimental uncertainties (with respect to the momentum cutoff): (i) the models for slow particle production implemented in DTUNUC 2.0 are in good agreement with data from hadron-nucleus as well as nucleus-nucleus collisions [56,57] (see Chapter 4), (ii) the dependence of shadowing on the photon virtuality and energy is qualitatively understood within our model and describes corresponding data of the E665-Collab. reasonably well [36] (see Sec. 2.4) and (iii) the rapidity distributions of negatively charged particles and of positively charged particles outside of the target fragmentation region in muon-xenon interactions and of charged particles in muon-deuterium interactions agree well

with E665-data.

The distribution of charged hadrons in the observable  $z = E/\nu$  ( $E$  and  $\nu$  being the secondary hadron energy and the photon energy in the target rest frame, resp.) was experimentally studied by Adams *et al.* [157] in muon–xenon interactions at 490 GeV. In Fig. 2.35a this distribution is compared to model results. The kinematic boundaries for this comparison are given by  $x < 0.005$ ,  $Q^2 < 1 \text{ GeV}^2$  and  $\nu > 100 \text{ GeV}$ . A good agreement within the whole  $z$ -range is found. Furthermore experimental information

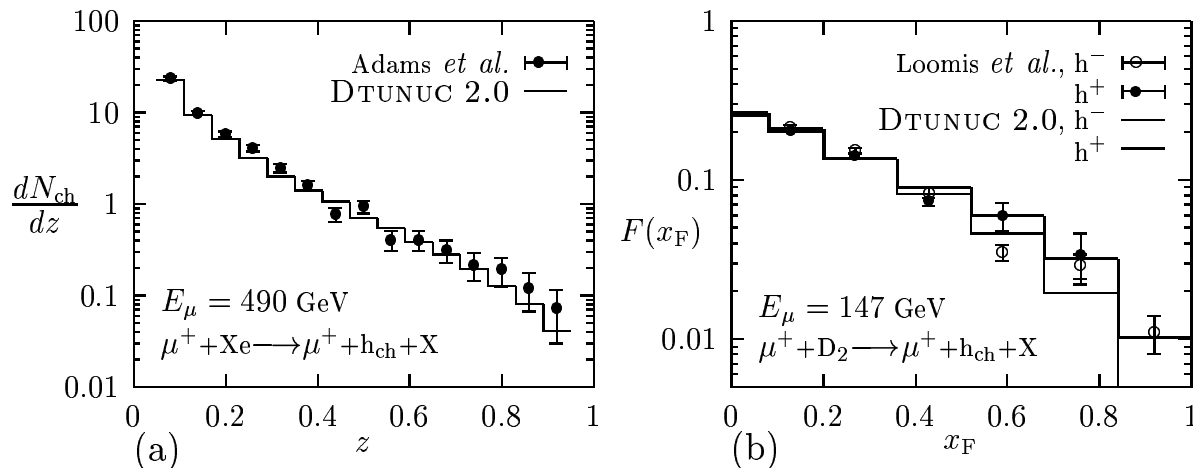


Figure 2.35: In a) calculated energy-distributions of charged hadrons from muon–xenon interactions at 490 GeV are compared to data of the E665-Collab. [157]. In b) calculated Feynman- $x$  distributions of charged hadrons from muon–deuterium interactions at  $E_{\text{Lab}} = 147 \text{ GeV}$  are shown together with data [148].

exists with respect to Feynman- $x$  distributions (see Eq.(2.86)) of charged hadrons [148]. A corresponding comparison of model results and data from muon–deuterium interactions at 147 GeV is shown in Fig. 2.35b. In agreement with the experimental trigger conditions the analysis has been restricted to photon virtualities in the range  $0.5 < Q^2 < 3 \text{ GeV}^2$  and to photon–nucleon c.m. energies exceeding 10 GeV.

Finally, we turn to transverse momenta of charged particles produced in muon–deuterium interactions and compare in Fig. 2.36 the transverse momentum distributions of positively and negatively charged hadrons in different  $x_F$ -ranges to data [148]. The DTUNUC results are presented as histograms whereas curves show fits to measured  $p_\perp$ -distributions. The experimental uncertainties are increasing with  $p_\perp$  and are at least of the order of the differences between the fits for positive and negative particles [148]. Taking them into consideration it follows that a satisfactory agreement between data and calculations exists. It is a well-known feature of minimum-bias particle production that the average transverse momenta of produced charged particles are correlated with their longitudinal momenta (*seagull effect*). In Fig. 2.37 this is shown for interactions of photons radiated off 147 GeV muons with deuterium. At large  $x_F$ -values the model results slightly deviate from the data. However, the considerable statistical uncertainties within the data at large  $x_F$  do not allow to draw further conclusions.

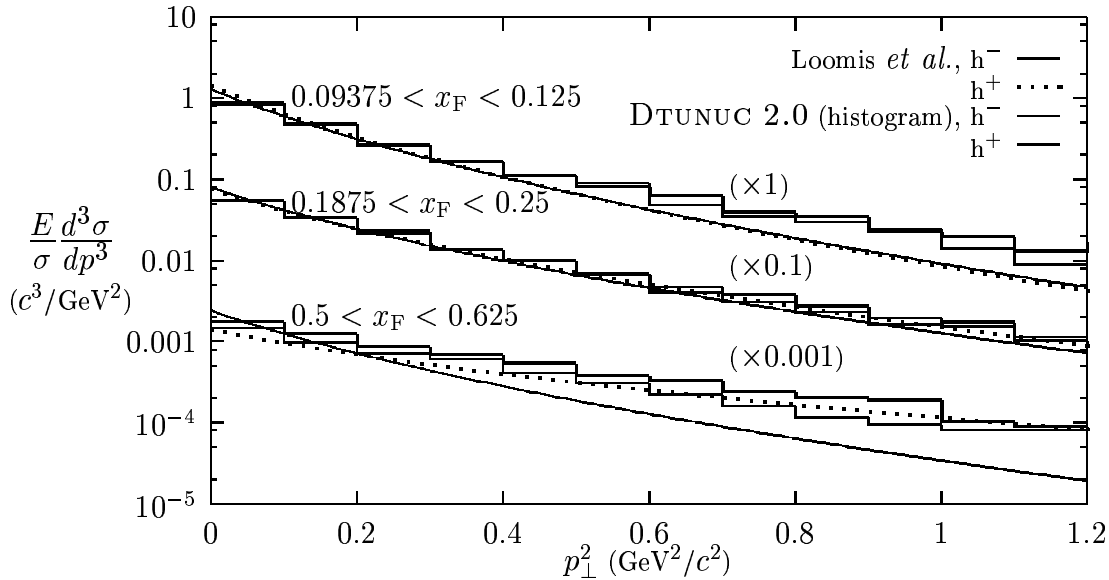


Figure 2.36: Transverse momentum distributions of charged hadrons from muon–deuterium interactions at 147 GeV. Model results (histograms) for different Feynman- $x$  bins are shown together with fits to data as given in [148].

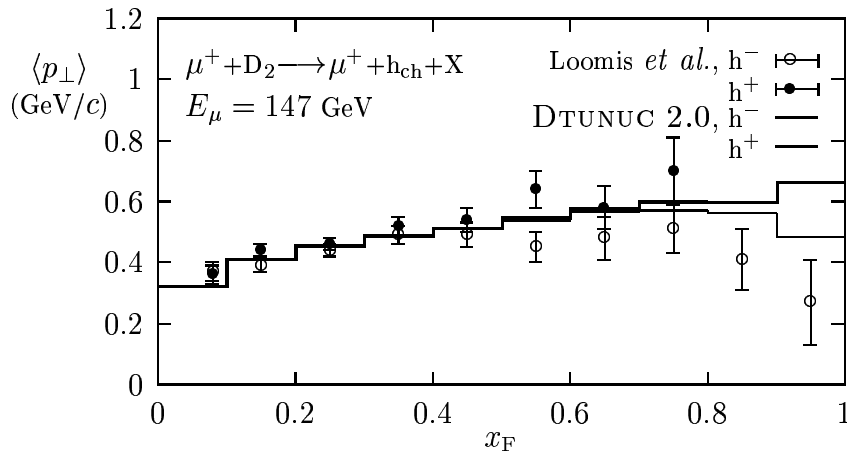


Figure 2.37:  $x_F$ -dependence of the average transverse momenta of positive and negative hadrons in muon–deuterium interactions at 147 GeV. Model results are compared to data [148].

### The nuclear dependence of particle production

In order to study the dependence of particle production on the mass number  $A$  of the nuclear target, inclusive single particle cross sections, like pseudorapidity ( $d\sigma/d\eta$ ), transverse momentum ( $d\sigma/dp_{\perp}^2$ ), or Feynman- $x$  distributions ( $d\sigma/dx_F$ ), are usually fitted to a  $A^{\alpha}$ -behavior. In the fragmentation region of the target nucleus  $\alpha$  can exceed the value of one due to the formation zone intranuclear cascade. In the projectile fragmentation region of photon–nucleus collisions  $\alpha$  can be expected to approach unity (i) for small  $q\bar{q}$ -nucleon cross sections, such as at low energies or for  $Q^2 > 0$ , (ii) for point-like photon interactions at high energies and (iii) at large transverse momenta due to hard interactions. In order to outline differences between the nuclear dependence for hadron and photon induced collisions the discussion is restricted to the projectile fragmentation region.

In the following fits to calculated distributions for interactions of protons, real photons

and virtual photons ( $Q^2 = 1 \text{ GeV}^2$ ) with carbon, aluminum, copper, silver, xenon and gold are discussed. Only charged hadrons with  $\beta > 0.7$  (shower particles) are taken into consideration.

In Fig. 2.38,  $\alpha(\eta)$  is shown for the three interaction channels and a laboratory energy of 250 GeV. In addition data from proton–nucleus interactions [158,159] are plotted. For

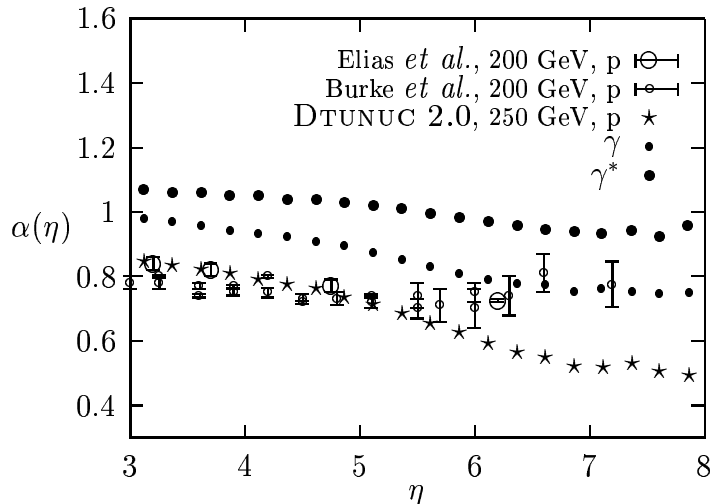


Figure 2.38: Nuclear dependence of the pseudorapidity distributions of charged particles:  $d\sigma/d\eta \sim A^{\alpha(\eta)}$ . Model predictions for proton-, real photon- and virtual ( $Q^2 = 1 \text{ GeV}^2$ ) photon–nucleus collisions are plotted together with measurements of proton–nucleus interactions [158,159].

$\eta > 5.5$  the model underestimates the measured nuclear dependence. At all  $\eta$ -values,  $\alpha$  is larger for photon- than for proton-projectiles. This reflects a stronger  $A$ -dependence of the cross sections (less shadowing) which is due to the smaller  $q\bar{q}$ -nucleon cross sections as compared to proton–nucleon cross sections.

Unfortunately, experimental information on the  $p_{\perp}$ -dependence of  $\alpha$  in proton–nucleus collisions exists, up to our knowledge, only for secondaries with large angles in the laboratory frame. Since with the model a strong dependence of the  $\alpha$ -values on this kinematic cut is found and, on the other hand, any kinematic restriction requires an enormous amount of simulated events in order to obtain the same statistics as without cuts, a conclusive comparison is difficult. In Fig. 2.39a the nuclear dependence is studied in proton–nucleus interactions at 250 GeV. From the calculated events only those final state particles with  $x_F > 0$  enter the analysis which have polar angles in the proton–nucleon c.m. frame of  $\theta_{\text{cms}} > 70^\circ$ . In addition the following measurements are plotted: charged pions from proton–nucleus interactions at 250 GeV [160] and 400 GeV [142], and positively and negatively charged hadrons from 400 GeV protons–nucleus collisions [161]. The calculated  $\alpha$ -values show the same  $p_{\perp}$ -behavior as the the measured ones: Below  $p_{\perp} \approx 0.3 \text{ GeV}/c$   $\alpha$  decreases slightly becoming  $p_{\perp}$ -independent up to  $p_{\perp} \approx 0.7 \text{ GeV}/c$  where  $\alpha$  starts to increase. Within the model, the high- $p_{\perp}$  behavior can be explained (i) by the Cronin effect which is treated by applying multiple scattering to the partons at the chain ends taking into account their path lengths inside nuclear matter [31,145] and (ii) by the fact that hard interactions mostly occur in events where the projectile interacts with one nucleon only (non-shadowing behavior). In Fig. 2.39b again model predictions for the three channels are compared to each other. Now, all charged final state hadrons with  $x_F > 0$  have been included.

Finally, in Fig. 2.40  $\alpha$  is plotted as function of the Feynman- $x$  variable together with experimental results [153] obtained from secondaries with  $p_{\perp} \approx 0.3 \text{ GeV}/c$ . In order to obtain reasonable statistics within the calculations all charged hadrons regardless of their

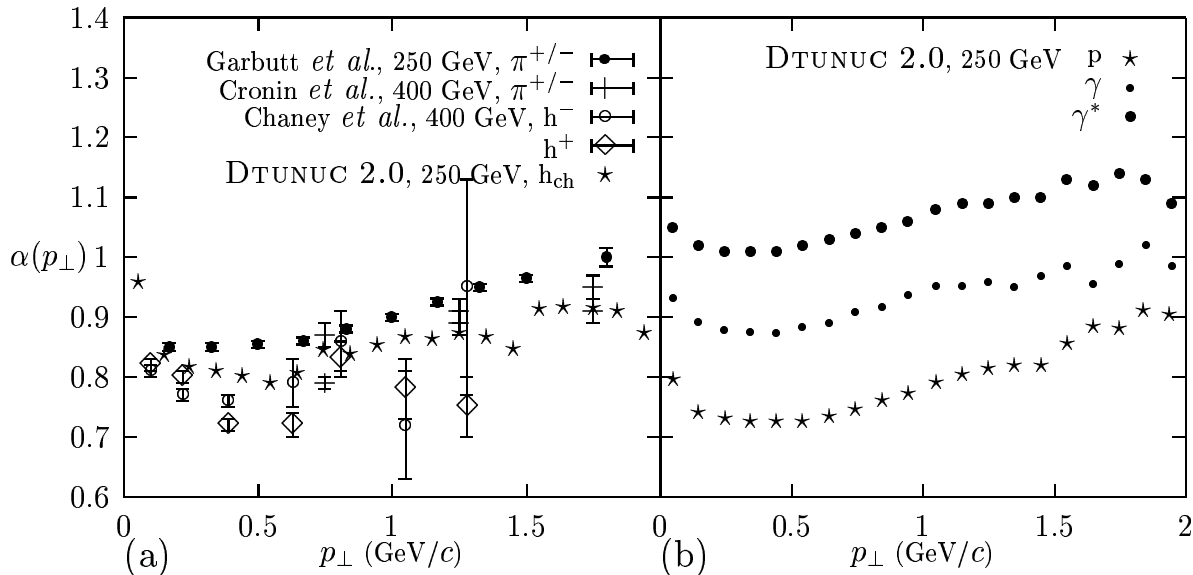


Figure 2.39: Nuclear dependence of the transverse momentum distributions of charged particles:  $d\sigma/dp_{\perp}^2 \sim A^{\alpha(p_{\perp})}$ . In a) DTUNUC results for proton–nucleus collisions are compared to several measurements [160,142,161]. From the calculated final state only forward charged hadrons with polar angles in the proton–nucleon c.m. system larger than  $70^\circ$  are included. In b) model predictions for proton–, real photon– and virtual ( $Q^2 = 1 \text{ GeV}^2$ ) photon–nucleus collisions and positive Feynman- $x$  are given.

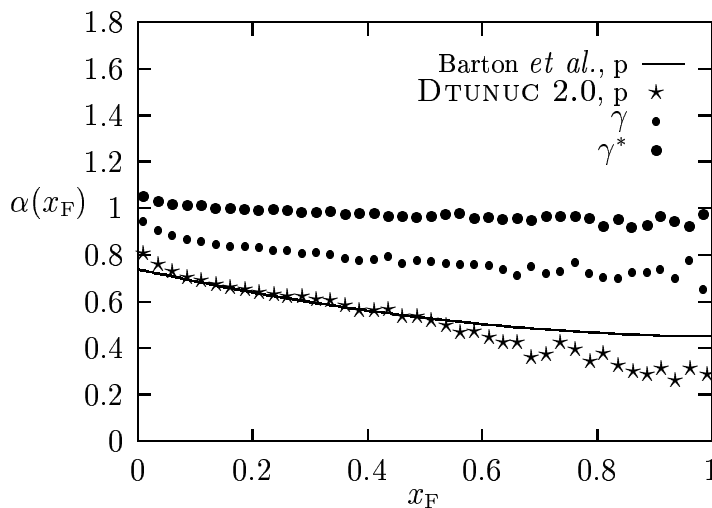


Figure 2.40: Nuclear dependence of the Feynman- $x$  distributions of charged particles:  $d\sigma/dx_F \sim A^{\alpha(x_F)}$ . Model predictions for proton–, real photon– and virtual ( $Q^2 = 1 \text{ GeV}^2$ ) photon–nucleus collisions are shown together with a fit to experimental data [153].

transverse momenta have been taken into consideration. An agreement with the data is found up to  $x_F \approx 0.5$ . At larger  $x_F$  the calculated  $\alpha$ -values are smaller. For photons  $\alpha$  is larger throughout the whole  $x_F$ -region; it decreases only weakly with increasing  $x_F$  for real photons and remains even constant at about  $\alpha(x_F) = 1$  for weakly virtual photons.

## 2.7 Jet Photoproduction off Nuclei at HERA-Energies

In the following properties of hadronic jets produced in interactions of real photons with nuclei are studied at energies which might be reached with nuclear beams at HERA.

Assuming nuclei with equal numbers of protons and neutrons the nuclear beam will have an energy per nucleon of 410 GeV [59]. With an average photon energy of about half of the electron energy (27.6 GeV) the photon–nucleon c.m. energy will be about 150 GeV.

As it has been shown in the analysis of data from HERA on photon–proton collisions [20] the study of jet production may confirm for the subdivision into direct and resolved photon interactions. Therefore it can be expected that differences between hadron–nucleus and photon–nucleus collisions and characteristic features of point-like photon interactions emerge most clearly in a study of jet production. In the following all observables used refer to the photon–nucleon c.m. system. Jets are defined according to the Snowmass-convention [162]. In the plane of pseudorapidity  $\eta$  and azimuthal angle  $\phi$  a jet is defined as a collection of particles contained in a cone of radius  $R = 1$  ( $\sqrt{(\Delta\eta)^2 + (\Delta\phi)^2} < 1$ , with  $\Delta\eta$  and  $\Delta\phi$  being the pseudorapidity and polar angle of a secondary with respect to the jet axis). The transverse energy  $E_{\perp}^{\text{jet}}$  of a jet is defined to be the sum of the particle transverse energies inside the cone. The jet pseudorapidity  $\eta^{\text{jet}}$  is calculated as  $E_{\perp}$ -weighted average over the pseudorapidities of the particles belonging to the jet.

In Fig. 2.41a the transverse energy distributions of jets from proton– and photon–carbon interactions are compared. Similar to proton/photon–proton interactions [33], the  $E_{\perp}^{\text{jet}}$  distribution extends to higher transverse energies for photon–nucleus collisions as compared to proton–nucleus collisions. It can be explained (i) by the ability of the photon to enter the hard interaction directly and (ii) by the properties of the photon

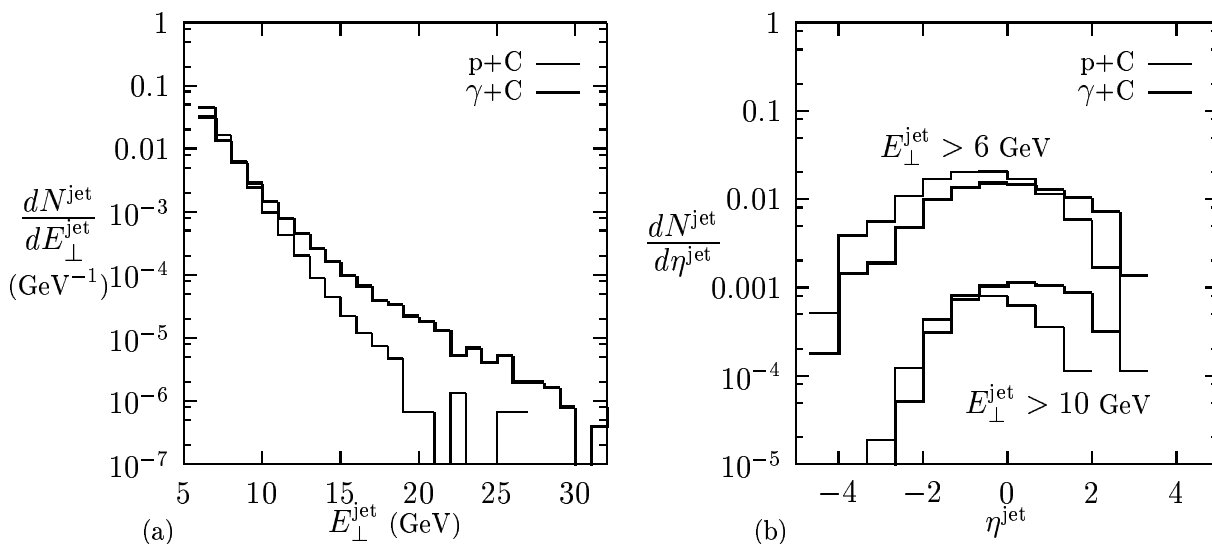


Figure 2.41: In a) transverse energy distributions are shown for hadronic jets from proton–carbon and real photon–carbon interactions at an energy of 150 GeV in the proton/photon–nucleon c.m. system. In b) the pseudorapidity distributions of the jet axes are shown for two lower cuts in transverse energy.

PDFs which are “harder” as compared to the proton PDFs. Both facts account also for the differences between the two channels in the pseudorapidity distributions of the jet axes in forward direction ( $\eta^{\text{jet}} > 0$ ). In backward direction the soft underlying event, being more pronounced for proton projectiles, is responsible for a higher jet rate. The

pseudorapidity distributions are shown in Fig. 2.41b for jets with transverse energies above 6 GeV and 10 GeV.

Jets originating from direct and resolved photon interactions might be separated if jet production is analyzed as function of

$$x^{\text{obs}} = \frac{E_{\perp}^{\text{jet1}} e^{\eta^{\text{jet1}}} + E_{\perp}^{\text{jet2}} e^{\eta^{\text{jet2}}}}{2E_{\gamma}} \quad (2.87)$$

where  $E_{\gamma}$  denotes the photon energy.  $x^{\text{obs}}$  can be considered as an estimate for the fraction of the projectile momentum entering the hard scattering [126,124]. In Fig. 2.42a  $x^{\text{obs}}$ -distributions are shown for proton-carbon, photon-carbon and photon-sulfur interactions. Point-like photon interactions contribute almost exclusively to the region  $x^{\text{obs}} > 0.6$ . The

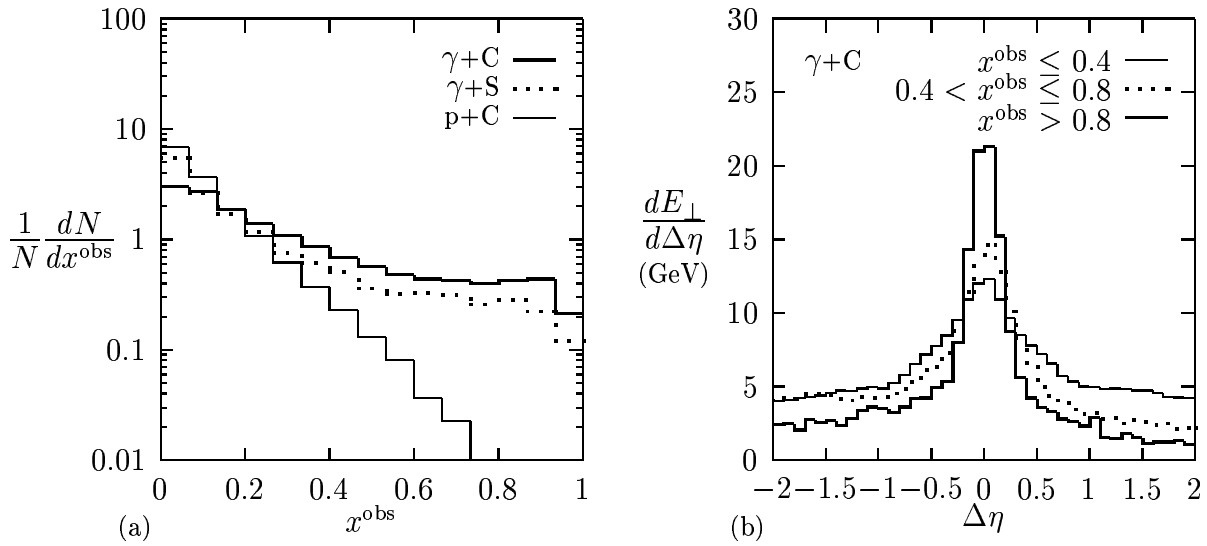


Figure 2.42: Dependence of jet production on  $x^{\text{obs}}$  at a proton/photon-nucleon c.m. energy of 150 GeV: In a) the  $x^{\text{obs}}$ -distributions for interactions with carbon and sulfur targets are plotted. In b) jet profiles are shown as function of the distance in pseudorapidity from the jet axis for different  $x^{\text{obs}}$ -bins.

specific properties of jets and of the underlying event are usually studied in terms of jet profiles. This is shown for photon-carbon interactions and different  $x^{\text{obs}}$ -bins in Fig. 2.42b where the average transverse energy is plotted as a function of the distance in pseudorapidity from the jet axis. Since in direct photon interactions there is no photon remnant which could contribute to the jet pedestal, the transverse energy outside the jets is decreasing with increasing  $x^{\text{obs}}$ .

## Chapter 3

# Aspects of Single Diffractive Interactions

Diffractive hadronic collisions are peripheral processes which typically exhibit multiparticle final states with “rapidity gaps”, i.e. rapidity regions with strongly suppressed particle density. Experimentally, these rapidity gaps are often used to identify this class of processes. Single diffractive interactions are characterized, for instance, by a quasi-elastically scattered projectile at large rapidities, a rapidity gap and a multiparticle final state of a certain invariant mass  $M_D$  in the target rapidity region. They are present with significant cross sections in hadron–hadron as well as hadron–nucleus collisions.

As initially mentioned the treatment of diffractive interactions in cascade calculations might be important, especially if secondary particles at large depths in material (like the atmosphere) have to be studied. For instance, the inclusion of target diffraction dissociation, i.e. processes in which the projectile keeps almost all of its momentum, into cosmic ray cascade calculations may result in higher fluxes predicted for vertical single hadrons at sea level [17,18]. Due to the rapidly dropping primary energy spectrum these fluxes are sensitive to those cosmic ray showers where the primary proton has either undergone much fewer interactions than on average or mostly peripheral interactions [18].

In this chapter two aspects of high-energy single diffractive processes are discussed, single diffraction dissociation in hadron–nucleus collisions [48] and single hard diffraction [49]. Sec. 3.1 describes the treatment of single diffractive hadron–nucleus collisions in the framework of the DPM. In particular, nucleus diffraction dissociation is considered in comparison with data on cross sections and multiparticle production [38]. Hadronic cross section fluctuations are introduced into the Gribov–Glauber approximation and their influence on diffractive cross sections is studied. In Sec. 3.2 hard diffractive interactions are discussed. The production of particles with large transverse momenta is approximated by  $2 \rightarrow 2$  scattering processes between partons in the pomeron and partons in the hadron. This requires suitable assumptions for pomeron parton distributions. Here, pomeron PDFs are obtained from a parametrization of the deuteron structure function which is motivated by Regge theory and by applying Regge-factorization [112,163]. Finally, model results on hard diffractive particle production in proton–antiproton and photon–proton collisions are compared to data [164,165].

### 3.1 Single Diffractive Hadron–Nucleus Interactions

Usually, coherent and non-coherent single diffraction dissociation is distinguished. Whereas in the former the projectile interacts diffractively with the nucleus as a whole [45] the latter is based on interactions of the projectile with single nucleons. In the following non-coherent processes are considered. Particular emphasis is put on diffractive nucleus decay since for this channel detailed experimental data exist.

In general, the projectile nucleon may scatter diffractively off several target nucleons. However, target diffraction dissociation involving more than one nucleon is assumed to be suppressed. In this study single diffraction dissociation in hadron–nucleus collisions is therefore approximated by single diffractive interactions of the projectile with only one target nucleon. All results discussed throughout this section are published in [48].

#### 3.1.1 Single Diffractive Cross Sections

The cross section for single diffractive nucleus decay can be estimated as follows. It is equal to the partial Gribov–Glauber cross section for the inelastic interaction of the hadron with one nucleon  $\sigma_{hA,1}^{\text{inel}}$  multiplied by the ratio of the (one-vertex) single diffractive to the inelastic hadron–nucleon cross sections

$$\sigma_{hA}^{\text{sd}} = \frac{\sigma_{hN}^{\text{sd}}}{\sigma_{hN}^{\text{inel}}} \sigma_{hA,1}^{\text{inel}}. \quad (3.1)$$

The calculation of  $\sigma_{hN}^{\text{inel}}$  and  $\sigma_{hN}^{\text{sd}}$  within the two-component DPM has been described in [28,47]. The cross section  $\sigma_{hA,1}^{\text{inel}}$  is obtained on the basis of a MC algorithm sampling inelastic events. It follows from the inelastic Gribov–Glauber cross section by multiplying it with the fraction of events where only one target nucleon is selected. The realization of the Gribov–Glauber formalism for hadron–nucleus collisions is similar to the one for  $q\bar{q}$ –nucleus interactions discussed in Sec. 2.4.3 except for different parameters entering the hadron–nucleon scattering amplitude [129,55].

In Fig. 3.1 results are shown for different target nuclei and  $E_{\text{Lab}} = 450$  GeV (open dots) together with data for beryllium, aluminum and tungsten [38]. The calculations sig-

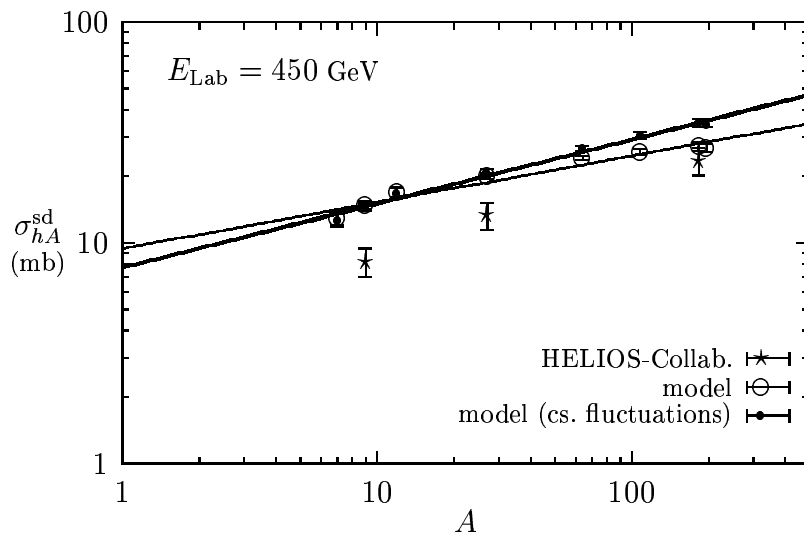


Figure 3.1: *Single diffractive hadron–nucleus cross sections calculated within the model are compared to data [38]. Model results obtained including cross section fluctuations (solid dots) and neglecting fluctuations (open dots) are given together with fits to these values (straight lines). Errorbars indicate the statistical uncertainties of the calculations.*

nificantly overestimate the measured values. This deviation might be caused by kinematic cuts applied to the data. The mass number-dependence of the cross sections can be studied by fitting an  $A^\alpha$ -behavior to the cross section values. A fit to the model results yields  $\alpha = 0.21 \pm 0.03$  which has to be compared to the experimental value of  $\alpha = 0.35 \pm 0.02$ .

A way to resolve this discrepancy is to introduce cross section fluctuations. Due to their substructure hadrons may interact in varying internal configurations (the cross section eigenstates of the interaction). A necessary condition for a hadron of momentum  $p_{\text{Lab}}$  and mass  $m$  to be “frozen” in a certain configuration during the time of passage through a target nucleus follows from the uncertainty relation [166]:

$$2R \lesssim \frac{1}{\Delta E} \approx \frac{2p_{\text{Lab}}}{M^2 - m^2}. \quad (3.2)$$

Here,  $R$  is a typical nuclear size and  $M$  is the mass of the inelastic cross section eigenstate.

This aspect of high-energy hadron–nucleus interactions can be taken into account by incorporating the concept of hadronic cross section fluctuations (see [167] and references therein). According to this concept the cross section of the considered scattering process is obtained by calculating first the cross section for a particular internal configuration and then integrating over all possible configurations weighted with their probabilities. For baryons the following cross section distribution  $P$  is assumed [167] (see Fig. 3.2)

$$P(\sigma) \sim \frac{\sigma/\sigma_0}{\sigma/\sigma_0 + a} \exp \left\{ - \left( \frac{\sigma - \sigma_0}{\Omega\sigma_0} \right)^n \right\} \quad (3.3)$$

with  $a = 0.1$ ,  $\sigma_0/\langle\sigma\rangle = 0.893$ ,  $\Omega = 1.1$  and  $n = 6$ .

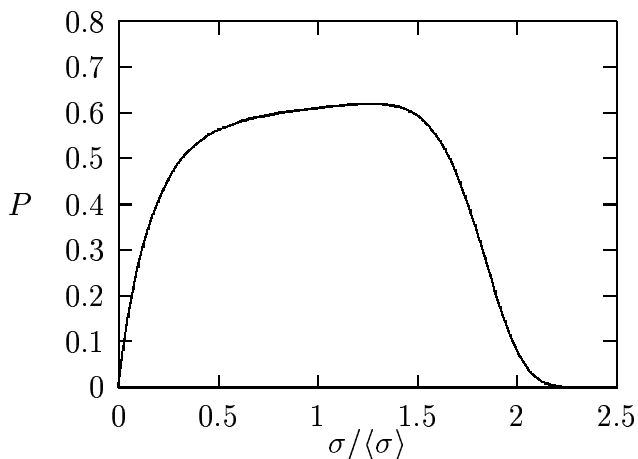


Figure 3.2: Cross section distribution around the average value  $\langle\sigma\rangle$ .

At small  $\sigma$  (configurations with small transverse size) this distribution is motivated by quark-counting rules which imply a  $\sigma^{N_q-2}$ -behavior with  $N_q$  being the number of valence quarks. Further constraints on the shape of  $P(\sigma)$  are imposed by considering the variance and the cubic moment. For instance, the variance can be related to nuclear shadowing and, therefore, to data on diffraction and elastic scattering [167].

Introducing cross section fluctuations according to Eq.(3.3) into the Gribov–Glauber formalism the fraction of events with only one wounded nucleon and therefore  $\sigma_{hA,1}^{\text{inel}}$  increase. Consequently, also the single diffractive hadron–nucleus cross section becomes larger, especially for heavy target nuclei as shown in Fig. 3.1. A fit of an  $A^\alpha$ -behavior to these results yields  $\alpha = 0.29 \pm 0.03$  being now consistent with the expectations for peripheral collisions, i.e.  $\alpha \approx 1/3$ .

### 3.1.2 Single Diffractive Particle Production off Nuclei

#### Single diffraction dissociation in DTUNUC

Incoherent single diffractive hadron–nucleus interactions have been implemented into the event generator DTUNUC 1.04 [145,146] in the approximation of single diffractive hadron–nucleon collisions as follows [48].

As discussed in Sec. 2.3.1, diffractive processes receive contributions from high- and low-mass components. High-mass single diffractive particle production can be related to an unitarity cut of the triple-pomeron graph (Fig. 3.3a,b). Fig. 3.3b implies that diffractive particle production might be interpreted as an “ordinary” scattering process between a

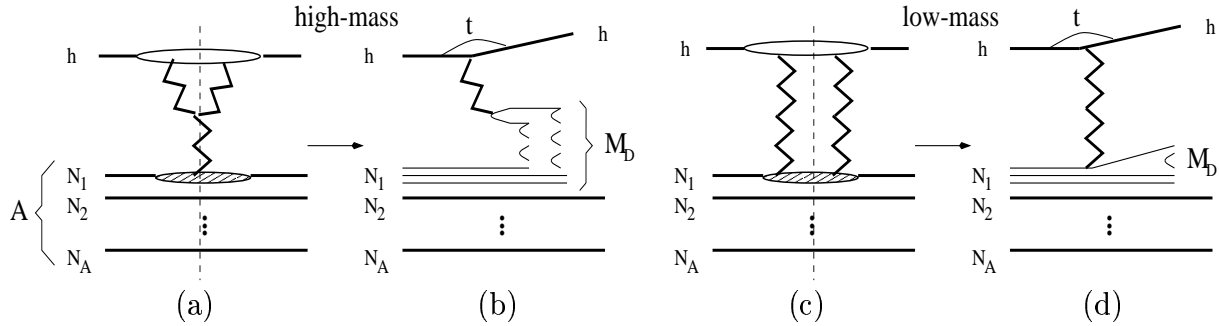


Figure 3.3: Approximation for the description of single diffractive hadron–nucleus interactions: The hadron interacts diffractively with only one target nucleon. Whereas the hadron is quasi-elastically scattered (momentum transfer  $t$ ) the nucleon turns into an excited state of mass  $M_D$  and decays diffractively. In terms of the DPM, diffractive particle production is described by diffractive unitarity cuts of the two-pomeron exchange graph subdivided into a) high-mass and c) low-mass contributions. In the present realization of the model these cuts correspond to two (b) and one chains of particles (d).

purely theoretical object (the pomeron) and a nucleon at an energy corresponding to the diffractive mass  $M_D$ . Particle production in the target rapidity region is dominated by two strings of total invariant mass  $M_D$  which connect a quark-antiquark pair of the pomeron with the valence partons of a nucleon (Fig. 3.3b). In each event the kinematic variables  $M_D$  and  $t$  are calculated according to the differential cross section for high-mass diffractive nucleon dissociation in the triple-pomeron approximation ( $s \gg M_D^2 \gg s_0$ ,  $M_D^2 \gg |t|$ , c.f. also the integrated cross section Eq.(2.30))

$$\frac{d^2\sigma_{\text{TP},N}}{dt dM_D^2} = \frac{1}{16\pi} (g_{h\mathbb{P}}^0)^2 g_{N\mathbb{P}}^0 g_{3\mathbb{P}}^0 \left(\frac{s}{s_0}\right)^{2\Delta_{\mathbb{P}}} \left(\frac{s_0}{M_D^2}\right)^{1+\Delta_{\mathbb{P}}} \exp(b_{hN}^{\text{sd}} t) \quad (3.4)$$

where  $s$  denotes the squared hadron–nucleon c.m. energy and the slope  $b_{hN}^{\text{sd}}$  is given by

$$b_{hN}^{\text{sd}} = b_{h\mathbb{P}}^0 + b_{3\mathbb{P}}^0 + 2\alpha'_{\mathbb{P}}(0) \ln\left(\frac{s}{M_D^2}\right). \quad (3.5)$$

The diffractive masses approximately follow a  $1/M_D^2$ -distribution ( $\Delta_{\mathbb{P}} \approx 0.08$ ) and the momentum transfer is exponentially distributed. If not constrained by experimental trigger

conditions the upper limit in the  $M_D$ -selection has to obey the coherence condition [168]

$$M_D^2 \leq \frac{s}{m_p R} \quad (3.6)$$

where  $R \simeq 1/m_\pi$  is a typical hadronic interaction radius.

It should be noted that in general all three pomerons of a triple-pomeron graph have to be treated as renormalized objects representing elementary multiple pomeron exchange diagrams (see Fig. 2.5). Hence it was recently suggested to apply the complete multiple scattering formalism of the two-component DPM to pomeron-hadron scattering [91,34]. However, as shown in a study of single diffractive hadron-hadron scattering [47] and with respect to the few data available on hadron-nucleus diffraction dissociation it turns out to be sufficient for a first approach to describe the pomeron-nucleon interaction by the exchange of one soft pomeron [48]. This applies of course only if the scattering energy is not too high ( $E_{\text{cm}} \lesssim 500$  GeV in the hadron-nucleon c.m. system).

Low-mass diffractive particle production is characterized by the excitation of the nucleon to a state of small  $M_D$  which either corresponds to the mass of a nucleon resonance or is treated as one string (Fig. 3.3d).

In both cases, in low- and high-mass diffraction dissociation, strings are hadronized applying JETSET [106,107]. Finally, the particles formed in the hadronization process may undergo secondary interactions inside the target nucleus (formation zone intranuclear cascade) [54,55].

### Comparison to experimental data

Nuclear target diffraction dissociation has been studied experimentally by only a few Collaborations [38,39]. Detailed results were published by the HELIOS-Collaboration on diffractive interactions of 450 GeV protons with beryllium, aluminum and tungsten [38]. In this section results obtained within the above discussed approximation are compared to these data. In agreement with experimental trigger conditions only those calculated events are considered in which the diffractive mass and the transverse momentum of the quasi-elastically scattered proton fulfill the conditions  $M_D^2 \leq 0.075s$  and  $0.1 \leq p_\perp \leq 0.6$  GeV/c, respectively.

In Fig. 3.4 the  $x_F$ -distribution of the single diffractive cross section is shown. Here the variable  $x_F$  is defined in the proton-nucleon c.m. system (the proton is moving along the positive  $z$ -axis) and denotes the ratio of the longitudinal proton momentum after the interaction to the momentum of the incoming proton,  $x_F = (p_\parallel/p)_{\text{cms}}$ . It is related to the diffractive mass by  $M_D^2 \approx (1 - x_F)s$ . In order to compare the shapes of the calculated and measured distributions the former have been normalized to the data at  $x_F \approx 0.98$ . As expected, a  $1/M_D^2$ -dependence describes the observed behavior in most of the studied  $M_D$ -region rather well.

In Fig. 3.5 the dependence of the differential single diffractive cross section on the momentum transfer  $t$  is compared to data for the three targets. Again the calculated distributions are scaled. The slopes agree for  $|t| > 0.1$  GeV<sup>2</sup> whereas the increase of the slope towards smaller  $|t|$ -values which might be caused by a background of elastic processes is not reproduced by the calculations since they include diffractive processes only.

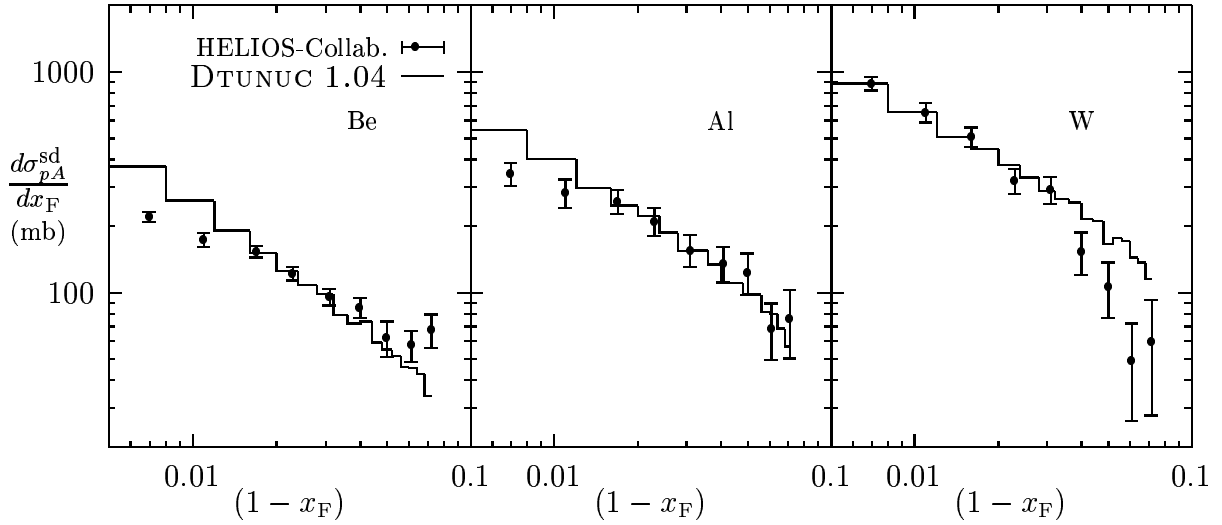


Figure 3.4: The differential single diffractive cross section  $d\sigma_{pA}^{sd}/dx_F$  is shown as function of the Feynman- $x$  of the quasi-elastically scattered proton for proton–beryllium, –aluminum and –tungsten interactions. Model results are compared to data [38].

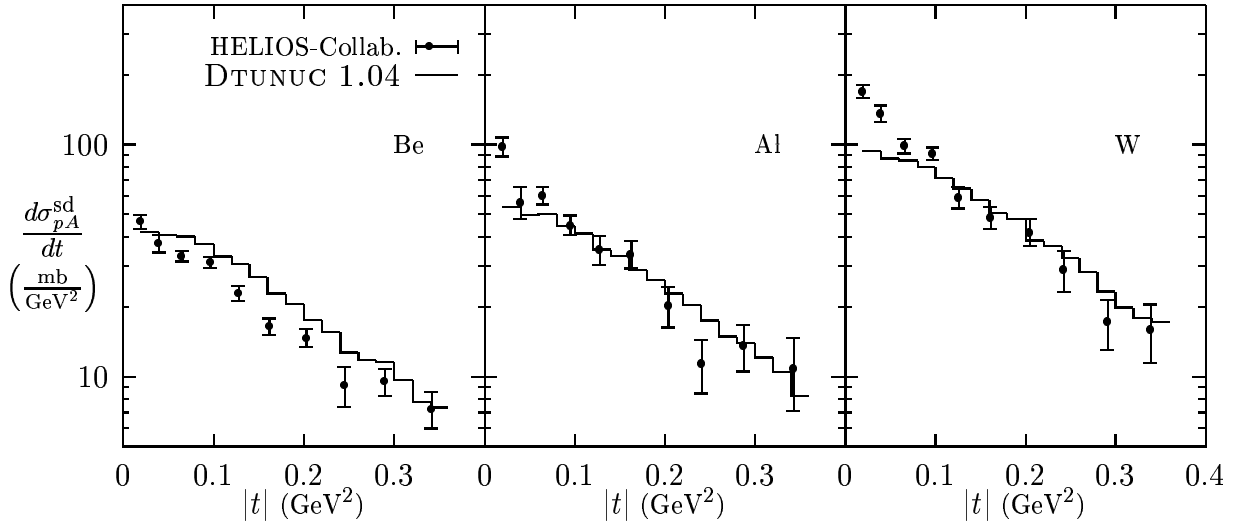


Figure 3.5: Calculated momentum transfer distributions in single diffractive proton–beryllium, –aluminum and –tungsten interactions are compared to measurements of the HELIOS-Collab. [38].

Within the model the slope  $b_{pN}^{sd}$  decreases with increasing  $M_D^2$  according to Eq.(3.5) which is in agreement to experimental results from diffractive hadron–hadron and photon–hadron scattering [168–172]. The data on diffractive nucleus decay in hadron–nucleus interactions seem to indicate the opposite behavior as given in Table 3.1 for beryllium and tungsten target. Hence the incoherent treatment might not be sufficient for large nuclei in the region of low  $t$ -values.

Furthermore the model of diffractive particle production can be tested by studying observables related to the produced particles. In Fig. 3.6a the multiplicity and in Fig. 3.6b the pseudorapidity distributions are shown for beryllium target. Though a qualita-

	Be		W	
	DTUNUC	Exp.	DTUNUC	Exp.
$0 \leq M_D^2 \leq 0.01s$	6.7	$5.3 \pm 0.5$	6.5	$6.6 \pm 0.5$
$0.02s \leq M_D^2 \leq 0.03s$	6.3	$6.5 \pm 0.5$	6.3	$8.0 \pm 0.8$
$0.05s \leq M_D^2 \leq 0.06s$	6.1	$7.0 \pm 0.5$	5.9	$8.3 \pm 0.7$

Table 3.1: *Slope parameters of the exponential  $t$ -dependence in single diffractive proton–beryllium and –tungsten collisions. Model results are compared to data [38] in different ranges of the diffractive mass. The slopes are given in units of  $\text{GeV}^{-2}$ .*

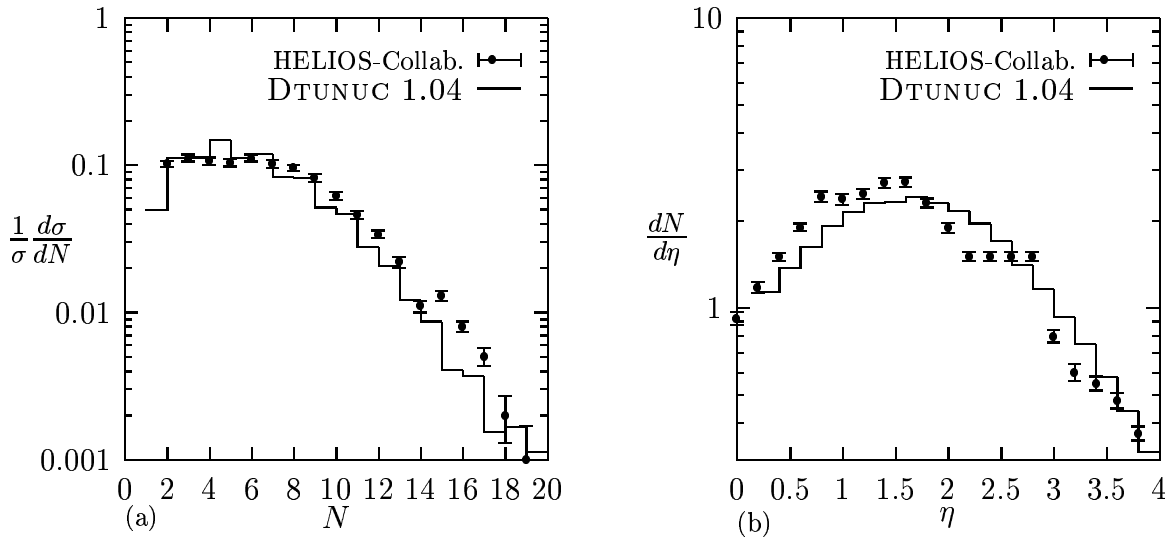


Figure 3.6: *Single diffractive proton–beryllium collisions at  $E_{\text{Lab}} = 450 \text{ GeV}$ : In a) the calculated multiplicity distribution and in b) the pseudorapidity distribution of produced particles are compared to data [38].*

tive agreement between model results and data exists uncertainties remain with respect to the experimentally considered data sample. For example, in Ref. [38] it is not mentioned whether neutral pions or their decay products are included into the experimental distributions. The calculated distributions shown in Fig. 3.6 contain the photons from  $\pi^0$ -decays.

The same uncertainty is present in the comparison of average pseudorapidities  $\langle \eta \rangle$  of diffractively produced particles shown in Fig. 3.7. Additionally, the experimental results are not corrected for limited detector acceptance. Again the model is able to reproduce the overall trend of increasing  $\langle \eta \rangle$  with increasing diffractive mass. However, further conclusions cannot be drawn until corrected data are available.

Finally, in Fig. 3.8 the dependence of the average transverse momenta of the final state particles on the diffractive mass is compared to data on proton–beryllium collisions [38]. A good agreement between model results and data is obtained.

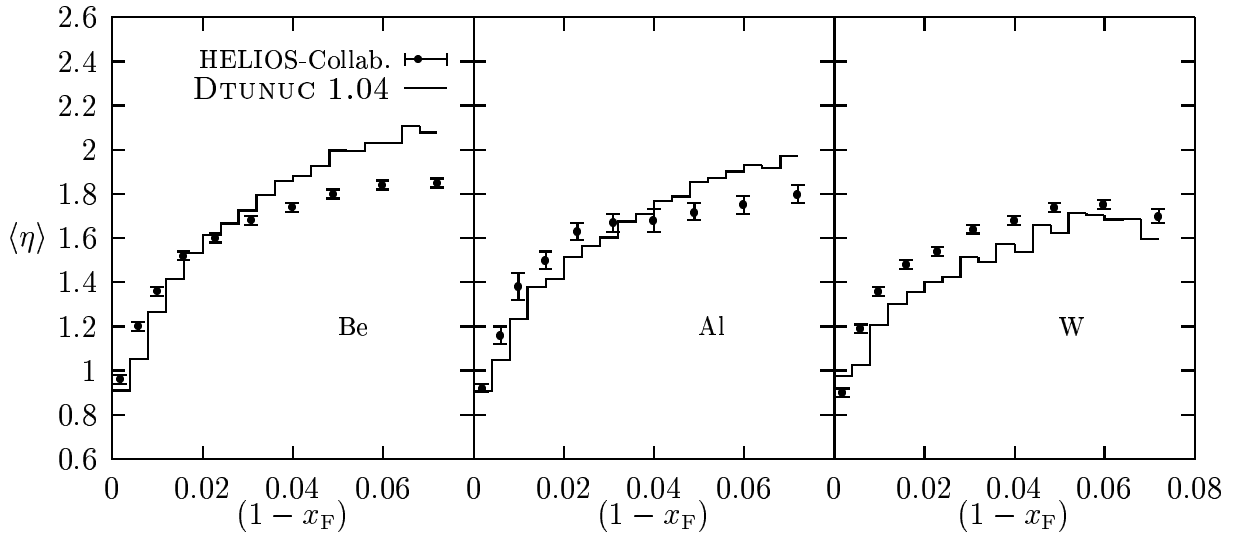


Figure 3.7: Average pseudorapidities of final state particles in single diffractive hadron–nucleus interactions are shown as function of the Feynman- $x$  of the quasi-elastically scattered proton. DTUNUC results are compared to data of the HELIOS-Collab. [38].

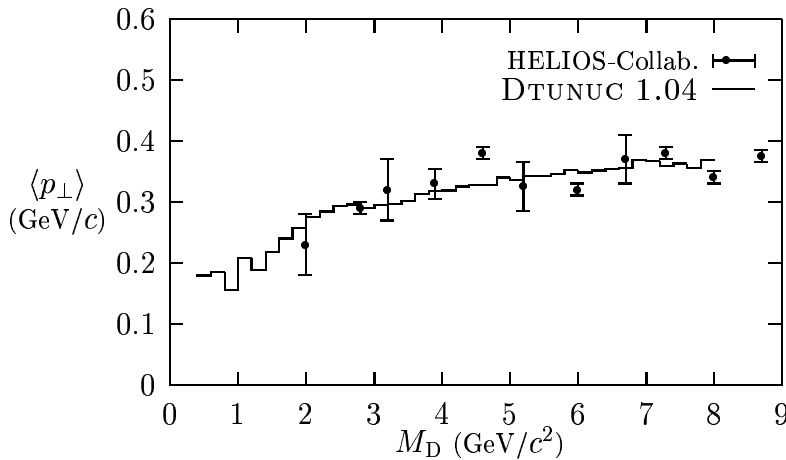


Figure 3.8: Dependence of the average transverse momenta of final state particles on the diffractive mass in proton–beryllium collisions.

## 3.2 Single Hard Diffraction

In collisions between hadrons jet production reflects partonic properties of the interacting particles. Similarly, the study of hard diffraction was proposed to provide an insight into the nature of the pomeron [173]. A partonic substructure should manifest itself in high-mass diffractive scattering through the appearance of jets. Following this suggestion first experimental evidence for jet production in single diffractive proton–antiproton [174,164,175] and photon–proton interactions [165,176] was found. The measurements indicate that, in contrast to hadrons, the pomeron is characterized by hard PDFs, i.e. a substantial fraction of the pomeron momentum may enter the 2-parton scattering process.

Beside experimental investigations the pomeron substructure has been subject to numerous theoretical studies, for example [177–185,163,186,187,49]. Unfortunately the data do not yet allow to draw definite conclusions concerning parton distributions inside the pomeron.

In the following an attempt is discussed to describe hard diffractive particle production on the basis of pomeron PDFs motivated by Regge theory together with lowest order perturbative QCD for the partonic scattering process [49]. Since inelastic hadron–hadron collisions dominate hadronic particle production in cosmic ray cascades special emphasis is put on single hard diffraction in proton–antiproton interactions.

### 3.2.1 Hard Diffractive Processes in the Triple-Pomeron Approximation

The differential cross section for high-mass single diffraction dissociation in the triple-pomeron approximation (c.f. Eq.(3.4)) can be written as a product of a “pomeron-flux” factor  $\Phi_{\mathbb{P}|h_1}$  and an effective pomeron–hadron cross section  $\sigma_{\mathbb{P}h_2}$  ( $h_1$  and  $h_2$  denote the interacting particles, such as hadrons or real photons)

$$s \frac{d^2 \sigma_{\text{TP},h_2}}{dt dM_D^2} = \Phi_{\mathbb{P}|h_1}(s, M_D^2, t) \sigma_{\mathbb{P}h_2}(M_D^2, t) \quad (3.7)$$

with

$$\Phi_{\mathbb{P}|h_1}(s, M_D^2, t) = \frac{1}{16\pi} (g_{h_1\mathbb{P}}(t))^2 \left( \frac{M_D^2}{s} \right)^{1-2\alpha_{\mathbb{P}}(t)}, \quad (3.8)$$

$$\sigma_{\mathbb{P}h_2}(M_D^2, t) = s_0 g_{h_2\mathbb{P}}^0 g_{3\mathbb{P}}(t) \left( \frac{M_D^2}{s_0} \right)^{\Delta_{\mathbb{P}}}. \quad (3.9)$$

Since the pomeron is a theoretical object only the product of pomeron-flux and pomeron–hadron cross section is an experimentally measurable quantity. The cross section  $\sigma_{\mathbb{P}h_2}$  depends of course on the definition of the pomeron-flux factor and vice versa.

Diffractive jet production rates can be estimated by substituting in Eq.(3.7)  $\sigma_{\mathbb{P}h_2}$  by the cross section  $\sigma_{\mathbb{P}h_2}^{\text{H}}$  for a single hard scattering between a parton of the pomeron and a parton of the hadron (see also Fig. 3.9)

$$s \frac{d^2 \sigma_{\text{TP},h_2}^{\text{H}}}{dt dM_D^2} = \Phi_{\mathbb{P}|h_1}(s, M_D^2, t) \sigma_{\mathbb{P}h_2}^{\text{H}}(M_D^2, t). \quad (3.10)$$

The hard cross section  $\sigma_{\mathbb{P}h_2}^{\text{H}}$  is obtained within lowest order perturbative QCD

$$\sigma_{\mathbb{P}h_2}^{\text{H}}(M_D^2, t, p_{\perp}^{\text{cut}}) = \int dx_1 dx_2 d\hat{t} \sum_{i,j,k,l} \frac{1}{1 + \delta_{k,l}} f_{i|\mathbb{P}}(x_1, Q^2, t) f_{j|h_2}(x_2, Q^2) \frac{d\hat{\sigma}_{i,j \rightarrow k,l}}{d\hat{t}} \Theta(p_{\perp} - p_{\perp}^{\text{cut}}). \quad (3.11)$$

The sum involves all possible parton configurations. A transverse momentum cutoff  $p_{\perp}^{\text{cut}}$  ensures that the integration is restricted to a kinematic region where perturbative QCD estimates can be applied. In order to calculate the cross section (3.11) the PDFs of the pomeron  $f_{i|\mathbb{P}}$  have to be specified.

Eq.(3.11) entails that the factorization property which is well-established in inclusive processes should apply also to hard diffractive processes. However, this has not been proven for any diffractive process. Moreover, effects have been discussed which may lead to a violation of factorization in hadron diffraction [178,183]. Qualitatively they give rise to an effect similar to a delta function term in the parton density of the pomeron (“super-hard” pomeron structure). However, it might be expected that the factorization assumption provides a reasonable approximation at very small  $|t|$  [183].

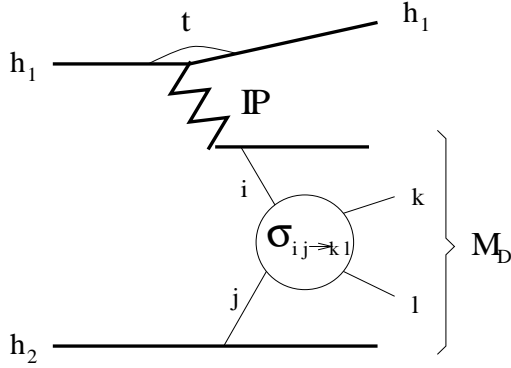


Figure 3.9: *Hard interaction in single diffraction dissociation of hadron  $h_2$ . The partonic  $2 \rightarrow 2$  scattering process between parton  $i$  of the pomeron and parton  $j$  of the hadron is described in lowest order perturbative QCD.*

### 3.2.2 Parton Distributions in the Pomeron

Pomeron PDFs are obtained following an approach proposed by Capella *et al.* [112,163] (CKMT-model) which relates the pomeron structure function  $F_2^{\mathbb{P}}$  to the structure function of the deuteron  $F_2^d$ . At moderate  $Q^2$ -values ( $Q^2 \lesssim 5 \text{ GeV}^2$ ) the deuteron structure function is derived from Regge-arguments as

$$F_2^d(x, Q^2) = A(Q^2)x^{-\Delta(Q^2)}(1-x)^{n(Q^2)+4} + B(Q^2)x^{1-\alpha_R}(1-x)^{n(Q^2)} \quad (3.12)$$

with

$$A(Q^2) = A \left( \frac{Q^2}{Q^2 + a} \right)^{1+\Delta(Q^2)}, \quad B(Q^2) = B \left( \frac{Q^2}{Q^2 + b} \right)^{\alpha_R}, \quad (3.13)$$

$$\Delta(Q^2) = \Delta_0 \left( 1 + \frac{2Q^2}{Q^2 + d} \right), \quad n(Q^2) = \frac{3}{2} \left( 1 + \frac{Q^2}{Q^2 + c} \right). \quad (3.14)$$

The first term in Eq.(3.12) is associated with the pomeron contribution determining the low- $x$  behavior of sea-quark distribution functions. The second term is parameterized according to secondary reggeon contributions governing the valence-quark distribution function of the deuteron. Details on the parameters entering the expressions (3.12–3.14) can be found in [112].

At small  $x$ -values, moderate photon virtualities and assuming Regge-factorization the ratio of the total cross sections of pomeron–photon and deuteron–photon scattering can be approximated by the ratio of the triple-pomeron to the deuteron–pomeron coupling constants (Fig. 3.10). Hence the pomeron structure function is calculated from  $F_2^d$  applying the following substitutions [163]

$$A(Q^2) \longrightarrow r_s(t)A(Q^2), \quad B(Q^2) \longrightarrow r_v(t)B(Q^2), \quad n(Q^2) \longrightarrow n(Q^2) - 2 \quad (3.15)$$

where  $r_s$  and  $r_v$  are coupling constant ratios. Here,  $r_s(0) = 3r_v(0) = 0.1$  is used [163] together with an exponential  $t$ -dependence of the triple-pomeron coupling (Eq.(2.29)). The latter substitution in (3.15) is motivated by dimensional counting rules since with respect to “valence” quarks the pomeron is similar to a meson. Then the pomeron structure function reads

$$F_2^{\mathbb{P}}(x, Q^2, t) = \sum_q e_q^2 x [f_{q|\mathbb{P}}(x, Q^2, t) + f_{\bar{q}|\mathbb{P}}(x, Q^2, t)] \quad (3.16)$$

$$= S(x, Q^2, t) + V(x, Q^2, t) \quad (3.17)$$

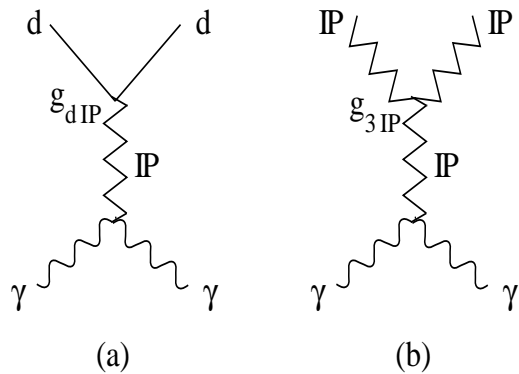


Figure 3.10: Pomeron exchange diagrams for the deuteron structure function (a) and the pomeron structure function (b). Regge factorization relates the latter to the deuteron structure function by the ratio of the couplings  $g_{3|P}$  and  $g_{d|P}$ .

with

$$S(x, Q^2, t) = r_s(t) A(Q^2) x^{-\Delta(Q^2)} (1-x)^{n(Q^2)+2}, \quad (3.18)$$

$$V(x, Q^2, t) = r_v(t) B(Q^2) x^{1-\alpha_R} (1-x)^{n(Q^2)-2}. \quad (3.19)$$

The sum in Eq.(3.16) includes all quark flavors and defines quark distribution functions of the pomeron. Note that the pomeron, being an object with quantum numbers of the vacuum, has charge parity  $C = 1$  and is isoscalar. The former property implies that  $f_{q|P} = f_{\bar{q}|P}$  for any quark  $q$  and the latter that  $f_{u|P} = f_{d|P}$ . Furthermore a SU(3)-symmetric sea of light quarks is assumed. Hence for the quark-densities in the pomeron one obtains

$$x f_{i|P}(x, Q^2, t) = \frac{3}{4} S(x, Q^2, t) + \frac{9}{10} V(x, Q^2, t), \quad i = u, \bar{u}, d, \bar{d} \quad (3.20)$$

$$x f_{s|P}(x, Q^2, t) = x f_{\bar{s}|P}(x, Q^2, t) = \frac{3}{4} S(x, Q^2, t). \quad (3.21)$$

The contribution from charm-quarks to the pomeron structure function is suppressed at the  $Q^2$ -values considered so far.

Experimental observations favor a relatively hard gluon distribution for the pomeron [164,176]. Due to the lack of detailed experimental information a rather simple ansatz of the form  $x(1-x)$  has been proposed in [173] and successfully applied in the following by many authors (see for instance [164,176,182,184]). Therefore this behavior is also assumed for the gluon density at small  $Q^2$  in the present study. It should be noted that, as recently discussed in [186], data on diffractive structure functions seem to indicate an even harder gluon density of the form  $(1-x)^{-0.5}$  for  $x \rightarrow 1$ . However, the qualitative features of hard diffractive particle production which are subject to this investigation turn out to be less sensitive to the exact shape of the ansatz for the hard gluon distribution<sup>1</sup>. Since there is no momentum sum rule for the pomeron parton densities the normalization of the gluon density cannot be determined in the same way as in the case of hadrons [178–180]. Here the gluon distribution is assumed to scale with the same factor  $r_s(t)$  as the sea quark contribution Eq.(3.18) [49].

<sup>1</sup>For example, in the work of Engel *et al.* [49] predictions on jet production in diffractive  $\gamma p$  collisions obtained with  $f_{g|P} \sim x(1-x)$  were presented. These calculations have been repeated with the gluon density of Capella *et al.* [186] and results are given in the thesis of Engel [34]

The distribution functions discussed so far approximate the parton content of the pomeron at small  $Q^2$ . In order to calculate PDFs at higher  $Q^2$ -values a QCD evolution in leading logarithmic approximation is performed by applying the code of Refs. [188,189] with  $Q_0^2 = 2 \text{ GeV}^2$ . The input distribution at  $Q_0^2$  and the resulting PDFs at higher  $Q^2$ -values are shown in Figs. 3.11 and 3.12. Note that the hardness of the  $u$ - and  $d$ -quark

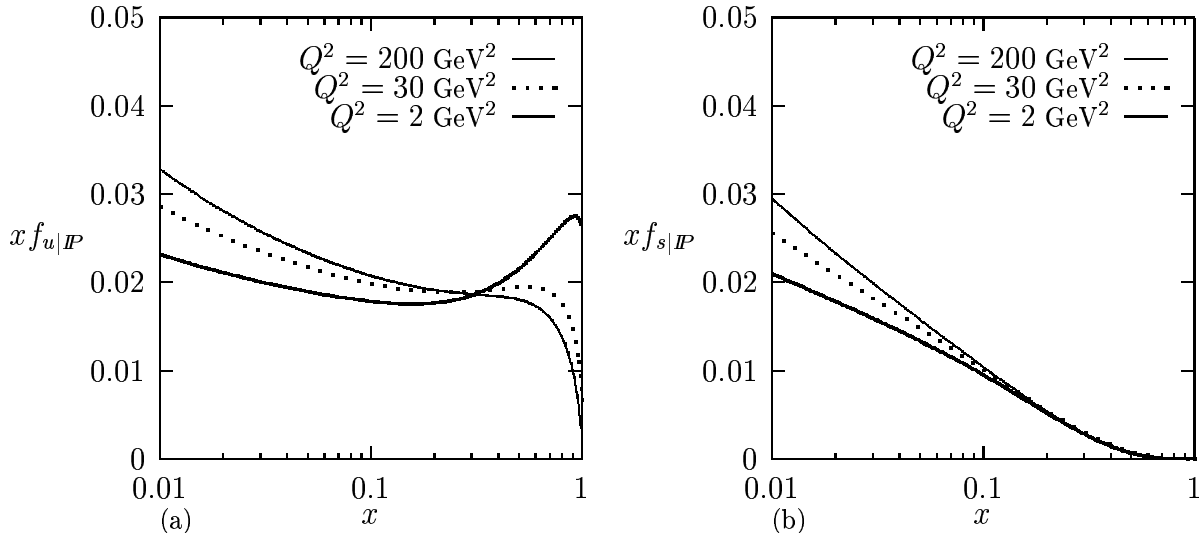


Figure 3.11: Distributions of  $u$ -quarks (a) and  $s$ -quarks (b) in the pomeron at  $t = 0$ . The initial distribution of the QCD evolution ( $Q^2 = 2 \text{ GeV}^2$ ) is shown together with results for higher  $Q^2$ -values.

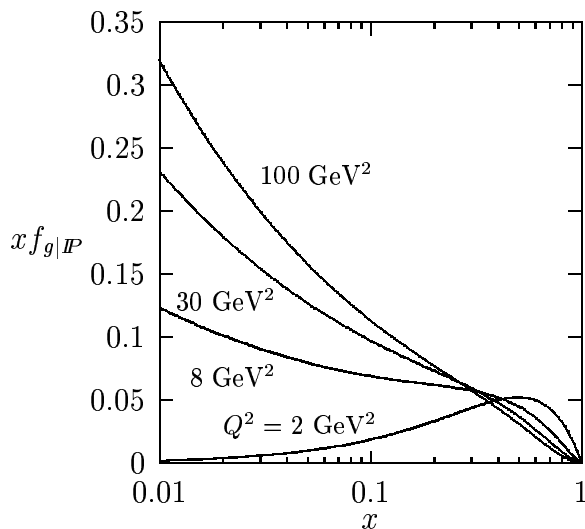


Figure 3.12: The gluon density in the pomeron at  $t = 0$  is shown for different  $Q^2$ -values.

distributions at small  $Q^2$  is governed by  $V(x, Q^2, t)$  which is parameterized according to secondary reggeon contributions.

### 3.2.3 Particle Production

Hard diffractive particle production in the approximation of a single hard scattering has been studied with the event generator PHOJET [49]. For each high-mass diffractive event

a mass  $M_D$  and a momentum transfer  $t$  are calculated according to the triple-pomeron approximation Eq.(3.7). According to the cross section (3.10), a hard scattering is then generated at a c.m. energy  $M_D$  using the pomeron PDFs discussed above and conventional PDFs for hadrons and photons [190,103,191]. Initial state radiation is taken into consideration since it may significantly modify the multiparticle final state of interactions involving large transverse momenta. Furthermore in case of hard diffraction dissociation of photons direct photon interactions are included. All possible color flow configurations of the hard subprocess [101,192] are considered during string formation. Finally, the strings hadronize according to the JETSET-model [106,107].

### Hard diffractive proton–antiproton interactions

Experimental evidence for jet production in single diffractive  $p\bar{p}$  collisions at  $\sqrt{s} = 630$  GeV has been found by the UA8-Collaboration [164]. These data are not corrected for detector acceptance effects and cannot be directly compared to results of the model. On the other hand, they provide the most detailed experimental information on single hard diffraction in hadron–hadron interactions being presently available. Therefore it might be worthwhile to discuss predictions of the model which are obtained with the same kinematic cuts as the data.

The distributions on jet production shown in the following refer to diffractively decaying protons moving along the negative  $z$ -axis. They include only those diffractive events which have  $1 < |t| < 2$  GeV<sup>2</sup>, a Feynman- $x$  of the quasi-elastically scattered antiproton in the range  $0.9 < x_F < 0.96$  and a total transverse energy of the particles produced in the pseudorapidity region  $|\eta| < 3$  exceeding 22 GeV. The restrictions on  $x_F$  ensure that the Regge-limit  $s \gg M_D^2 \gg |t|$  is satisfied although the momentum transfer  $|t|$  is rather large. Jets are identified using a cone algorithm in the  $\eta - \phi$ -plane similar to the one applied in Sec. 2.7. Only jets with  $|\eta^{\text{jet}}| < 2$  and  $E_{\perp}^{\text{jet}} > 8$  GeV (jet radius  $R = 1$ ) are considered.

An observable being sensitive to the partonic structure of the pomeron is  $x^{\text{jet}}$  [164]. It is defined as the momentum component of a jet in the pomeron–proton c.m. system along the pomeron–proton axis normalized to its maximum value,  $x^{\text{jet}} = 2p_{\parallel}^{\text{jet}}/M_D$ . Fig. 3.13a shows the prediction of the model on the  $x^{\text{jet}}$ -distribution, whereas the corresponding measured distribution [164] is plotted in b). The data were obtained with essentially full acceptance at positive  $x^{\text{jet}}$ -values [164]. Therefore the model results should be in qualitative agreement with the uncorrected data in this region.

The distribution of a variable related to  $x^{\text{jet}}$ , the pseudorapidity  $\eta^{\text{jet}}$  of the jet axis in the  $p\bar{p}$  c.m. system, is shown in Fig. 3.14. Again model results and UA8-data [164] are plotted separately. The large- $x$  behavior of the pomeron PDFs strongly influences the tail at positive  $\eta^{\text{jet}}$ -values. Assuming the acceptance corrections in the pomeron (forward) hemisphere to be small the data seem to indicate harder parton distributions than used in the model.

The longitudinal momentum of a 2-jet system along the pomeron–proton axis more directly reflects the differences between the parton distributions in the pomeron and in the proton. In particular, it should be sensitive to a super-hard contribution to the pomeron structure function which can be expected, for instance, from the factorization-breaking effects discussed in [183]. In analogy to  $x^{\text{jet}}$ , a variable  $x^{2\text{-jet}}$  is defined as the longitudinal momentum of a 2-jet system normalized to  $M_D/2$ , i.e.  $x^{2\text{-jet}} = x^{\text{jet}1} + x^{\text{jet}2}$ . In Fig. 3.15a the

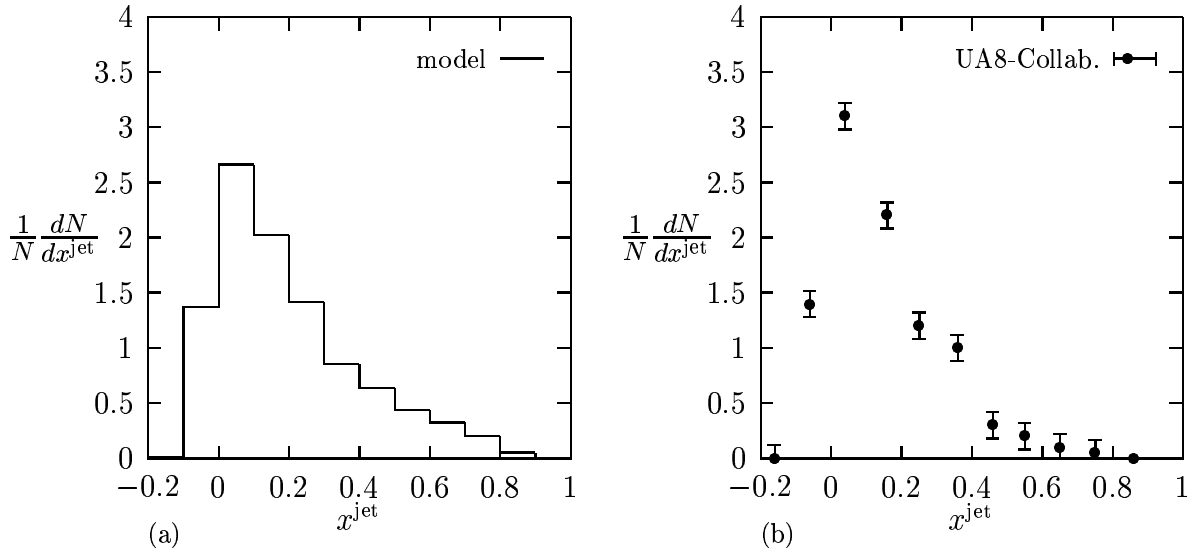


Figure 3.13: In a) the calculated distribution of jet momenta in single diffractive  $p\bar{p}$  collisions at  $\sqrt{s} = 630$  GeV is shown. The quantity  $x^{\text{jet}}$  is defined as the ratio of the longitudinal jet momentum and its maximum value in the pomeron-proton c.m. system. The diffractive mass is restricted to the range  $0.06s < M_D^2 < 0.08s$ . In b) uncorrected data of the UA8-Collab. [164] are plotted.

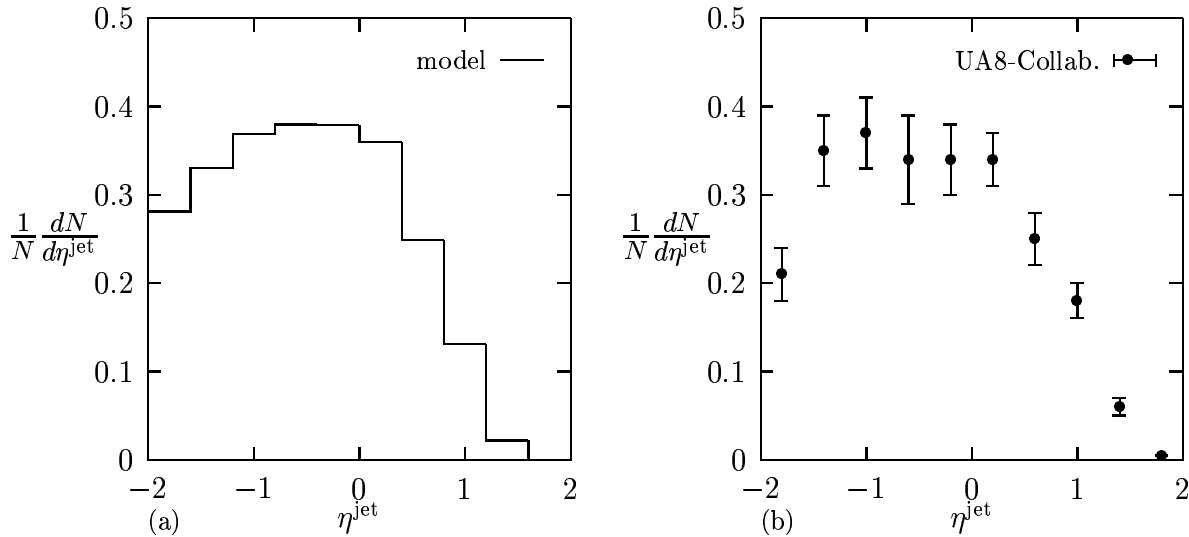


Figure 3.14: In a) the distribution of jet pseudorapidities in the  $p\bar{p}$  c.m. system as calculated within the model is shown. In b) the corresponding uncorrected data [164] are plotted. Both distributions include events with diffractive masses in the range  $0.06s < M_D^2 < 0.08s$ .

distribution of  $x^{2\text{-jet}}$  as calculated with the model is shown. The contributions of gluons and quarks in the pomeron to the  $x^{2\text{-jet}}$ -distribution are given in addition. From the model a significant fraction of events with  $x^{2\text{-jet}} \gtrsim 0.7$  is obtained. They arise mostly because of the hard shape of the valence-quark distribution (see Fig. 3.11a). The corresponding UA8-data [164] are plotted in Fig. 3.15b. Both, the calculated and measured distributions are very similar in shape. The contribution at  $x^{2\text{-jet}} > 0.9$  in the data is attributed to a

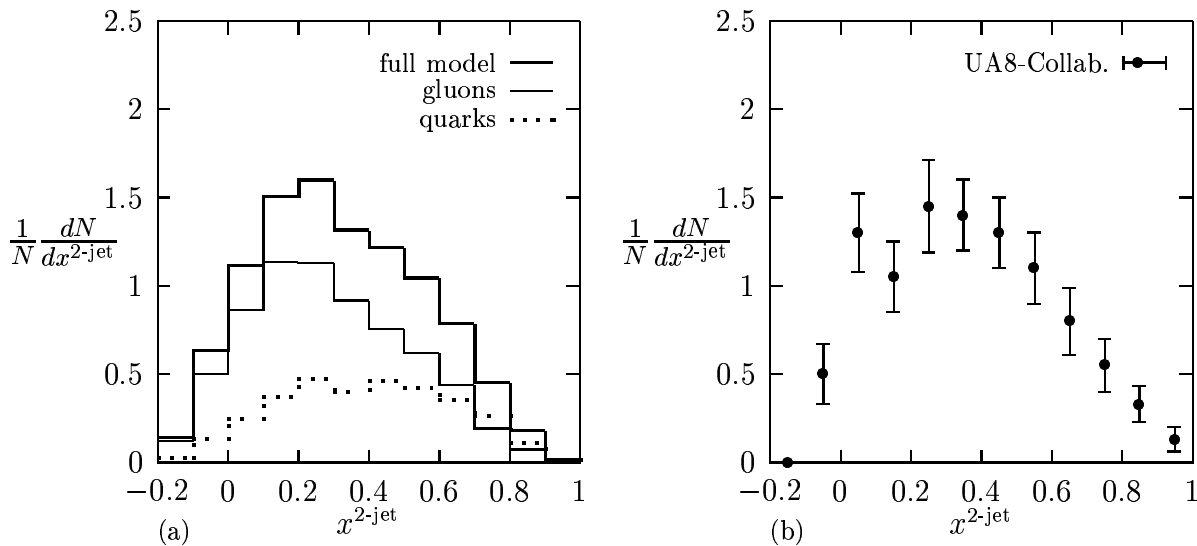


Figure 3.15: Longitudinal momentum distribution of 2-jet systems in diffractive  $p\bar{p}$  collisions at  $\sqrt{s} = 630$  GeV. In a) the the model prediction is shown together with the contributions from gluons and quarks in the pomeron. In b) the corresponding uncorrected UA8-data [164] are given. Only events with  $0.04s < M_D^2 < 0.1s$  are considered.

super-hard pomeron structure [164]. In the calculated distribution which does not contain a super-hard component no effect is seen.

In summary it can be concluded that, apart from a contribution of a possible super-hard component in the pomeron structure, the model might be able to describe the UA8-data. However, no definite conclusions can be drawn before corrected data become available.

### Hard diffractive photoproduction

First experimental information on rapidity gap events indicating features of hard diffraction has been obtained in  $\gamma p$  collisions at HERA [165,176]. In the following only one example is discussed which should illustrate that particle production in hard diffractive photon-proton interactions is well described within the model. Further examples are given in [49].

The presence of hard processes in single diffractive  $\gamma p$  scattering is clearly visible in the inclusive charged particle cross section at large transverse momenta. Model results for diffractive photoproduction at HERA are shown in Fig. 3.16. Complete hadronic final states of minimum bias electron-proton collisions have been generated (i.e. soft and hard diffractive processes are included) taking the kinematic cuts of the experiment into account. The cross sections refer to  $ep$  collisions. The flux of quasi-real photons is calculated according to the EPA (see Eq.(2.75)) applying the photoproduction selection criteria  $0.25 < y < 0.7$  and  $Q^2 \leq 0.01$  GeV<sup>2</sup>. The distribution is averaged over the pseudorapidity range  $-1.5 < \eta_{\text{Lab}} < 1.5$ . In addition uncorrected data of the H1-Collaboration on charged tracks are shown [165]. In order to compare the shapes of the calculated and measured distributions, the latter are scaled. The systematic difference between the model results and the data at low transverse momenta ( $p_{\perp} \lesssim 1$  GeV/c) can be qualita-

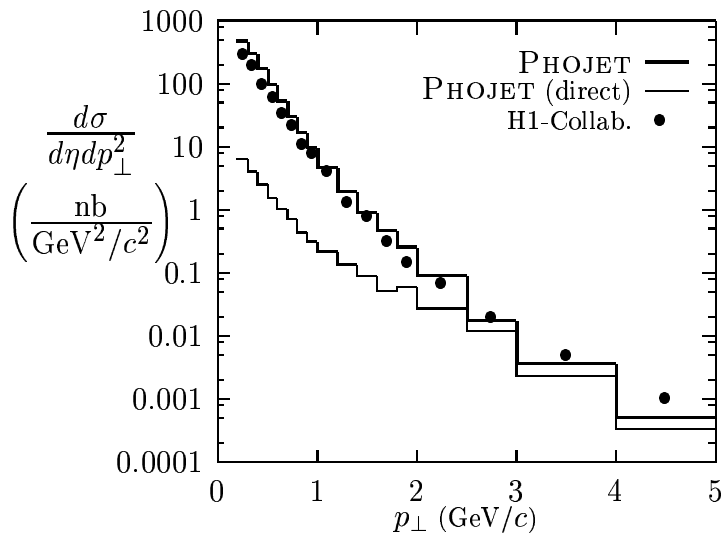


Figure 3.16: *Inclusive charged particle cross section for rapidity gap events in photoproduction at HERA (photon dissociation). The results from the full model (thick line) and the contribution from direct photon-pomeron interactions (thin line) are shown together with scaled data [165].*

tively explained by the  $p_{\perp}$ -dependent experimental acceptance in this region. The tail of the calculated distribution at large  $p_{\perp}$  which arises from hard diffraction is in reasonable agreement with the data. In addition the contribution from direct photon processes is shown. They account for the majority of the cross section at large  $p_{\perp}$ .

## Chapter 4

# Projectile and Target Associated Particle Production

Many properties of particle cascades induced by high-energetic nuclei in matter depend on the particular features of particle and fragment production in the fragmentation region of the incident nucleus. These particles and fragments appear in the very forward direction of the cascade and influence their characteristics, especially at large depths in the material. Cosmic ray cascades in the atmosphere are only one example where an adequate description of these projectile (or target) associated processes can be important.

An appropriate treatment of projectile and target associated particle production has been implemented in the event generators DPMJET-II [31,15,193] and DTUNUC 2.0. It is expected to be valid in peripheral nucleus–nucleus collisions and, in asymmetric collisions, in the fragmentation region of the heavier nucleus.

Projectile associated particle production<sup>1</sup> in peripheral nucleus–nucleus collisions is commonly described as a two-step process [194]:

1. Particles produced in the interaction of the target with projectile nucleons may propagate and reinteract in the part of the projectile nucleus which was not involved in the primary interaction (*spectator nucleus*). These processes are called **intranuclear cascade**. At the end of the intranuclear cascade the spectator nucleus is often assumed to be left in an equilibrium state (in the following called *prefragment*), in which the excitation energy is shared by a large number of nucleons. The prefragment is characterized by its mass, charge and excitation energy with no further memory of the steps which led to its formation.
2. The excited prefragment may disintegrate in a second step into nucleons and fragments by **evaporation** and **fragmentation** processes. The disintegration of a fragment stops if its nuclear excitation energy becomes lower than any separation energy. This residual excitation energy is then dissipated through emission of photons ( $\gamma$  **de-excitation**). Throughout this chapter the stable fragment with the highest mass number is called *residual nucleus*.

In the following sections models for intranuclear cascades, evaporation, fragmentation of light prefragments, high-energy fission, and  $\gamma$  de-excitation and their MC implementa-

---

<sup>1</sup>The description of target associated particle production is identical

tions are discussed. In Sec. 4.1 the basic assumptions of the formation zone intranuclear cascade model are summarized and an extension to nucleus–nucleus collisions is presented. Based on this treatment of intranuclear cascade processes the excitation energies of prefragments are calculated in Sec. 4.2. In order to describe the further disintegration and de-excitation of these prefragments existing MC models for evaporation, fragmentation and  $\gamma$  de-excitation are applied. The basic ideas underlying these models are summarized in Sec. 4.3. In a detailed comparison in Sec. 4.4 of model results and data on hadron–nucleus and nucleus–nucleus collisions it is demonstrated that combining these models a reasonable description of most of the experimental results on projectile and target associated particle production can be obtained. Finally in Sec. 4.5 applications to cosmic ray cascades in the atmosphere are discussed.

All results presented in this chapter are published in [56–58].

## 4.1 Intranuclear Cascade

### 4.1.1 Basic Assumptions

The model for intranuclear cascade processes discussed in this chapter is based on the following assumptions:

- A nucleus is treated as a cold Fermi-gas of nucleons moving in a potential well.
- Hadrons propagate in the nuclear medium between subsequent interactions like free particles on straight trajectories.
- Primary and secondary hadrons may interact with nucleons in elastic and inelastic scattering processes according to the local nuclear density and vacuum cross sections. The interactions occur incoherently and uncorrelated.
- Only scattering processes of stable hadrons with nucleons are considered.
- The nucleons obey Pauli’s principle.

In general, interactions of resonances with nucleons would have to be considered. However, the corresponding cross sections are less well-known. Therefore the resonances are assumed to decay at the spatial position of their production and only the decay products are taken into account for further cascade processes. The effects of this approximation are compensated for by the choice of the formation time parameter (see following section).

### 4.1.2 The Formation Zone Intranuclear Cascade Model

The application of an intranuclear cascade model based only on the previously given assumptions to high-energy nuclear collisions would result in an overestimation of measured particle multiplicities in the fragmentation region of the corresponding nucleus. For instance, in experiments using nuclear target emulsions it has been observed that multiplicities of slow particles saturate at laboratory energies of about 10–30 GeV and remain roughly constant as the energy increases further (see [195] and references therein). A

physical mechanism describing the suppression of the intranuclear cascade at high energies is the “formation zone” concept. It has been introduced by Stodolsky [196] in analogy to the Landau–Pomeranchuk effect.

The Landau–Pomeranchuk effect [197,198] explains the observation that the energy loss due to bremsstrahlung suffered by an electron undergoing multiple scattering in a material is damped at high energies, i.e. the electron becomes more penetrating. The energy radiated by the electron along its path can be written as

$$\frac{d^3 I}{dk^3} \sim \left| \int d^3 x dt j(\vec{x}, t) e^{i(\vec{k} \cdot \vec{x} - \omega t)} \right|^2, \quad (4.1)$$

with  $j$  being the current density of the electron and  $k = (\omega, \vec{k})$  the photon 4-momentum. As long as interference effects from different collisions are small, the radiation emitted along the path of the electron can be estimated by the average radiation emitted in one collision multiplied by the number of collisions. This is possible if the exponent in Eq.(4.1) varies sufficiently which causes random relative phase factors in subsequent collisions. Assuming the path to be a series of straight segments and  $j \sim (m/E)\delta(\vec{x} - \vec{v}t)$  the integral becomes

$$\frac{d^3 I}{dk^3} \sim \left| \int_{\text{path}} dt e^{-it/\tau} \right|^2. \quad (4.2)$$

The quantity

$$\tau = \frac{1}{\omega - \vec{k} \cdot \vec{v}} = \frac{E}{k \cdot p} = \frac{E}{m \omega_e} \quad (4.3)$$

is called “formation zone” or “formation time” [196]. Here,  $p$ ,  $E$ , and  $m$  are the 4-momentum, energy and mass of the electron, resp.  $\omega_e$  denotes the frequency of the photon in the rest frame of the electron.  $\tau$  represents a minimum characteristic time or distance necessary to define the photon.

The translation of the formation zone concept to hadron–nucleus collisions has been discussed in detail in [196,54–56]. Here its application to nucleus–nucleus collisions is introduced [57].

Within the quark model the states being formed in the primary nucleon–nucleon interaction can be understood as being built up of valence quarks only, i.e. without the full system of sea quarks, antiquarks and gluons. They therefore interact inside the spectator parts of the colliding nuclei with reduced probabilities [199]. This is approximated by assigning formation times to the produced hadrons, i.e. within its formation time a hadron is not able to reinteract with nucleons of the spectators. In the following the 4-momenta of the projectile hadron  $p_p$  and the secondary hadron  $p_s$  in the rest frame of the considered nucleus are denoted by

$$p_p = (E_p, 0, 0, \sqrt{E_p^2 - m_p^2}), \quad p_s = (E_s, \vec{p}_{s\perp}, \sqrt{E_s^2 - m_s^2 - \vec{p}_{s\perp}^2}). \quad (4.4)$$

Replacing the electron 4-momentum in Eq.(4.3) by  $p_p$  and the photon 4-momentum by  $p_s$  the formation zone  $\tau$  of the secondary hadron reads for  $E_p \gg m_p$  [196]

$$\tau = \frac{2E_s}{(m_p x)^2 + m_s^2 + \vec{p}_{s\perp}^2}, \quad x = \frac{E_s}{E_p}. \quad (4.5)$$

For the majority of secondaries the term  $(m_p x)^2$  is small and can be neglected. In the rest frame of the secondary hadron an average time  $\tau_s$  for the formation of a complete hadronic state is defined as [54,199]

$$\tau \approx \frac{E_s}{m_s} \tau_s, \quad \tau_s = \tau_0 \frac{m_s^2}{m_s^2 + \vec{p}_{s\perp}^2}. \quad (4.6)$$

$\tau_0$  is a model parameter which has to be determined by comparing particle production within the model to experimental data. Typical values are of the order of 1–10 fm/c [55,31]. In the following a value of  $\tau_0 = 4.5$  fm/c is used [58]. It differs slightly from the values reported in [56,57] due to an updated treatment of nuclear evaporation as compared to the version of the code used in [56,57]. For each secondary hadron a formation time in its rest frame is sampled from an exponential distribution [200] with the average value  $\tau_s$ .

In the model the full space–time history of the collision is known. In any particular Lorentz frame the trajectories of the secondaries formed in the hadronization of the strings can be traced in space and time. After having assigned a formation time to a secondary hadron an intranuclear cascade step is considered first in the rest frame of one of the spectator nuclei (chosen at random). Due to relativistic time dilatation secondaries with high energies are mostly formed outside of the spectator part of this nucleus whereas those with low energies are formed inside. The latter may propagate in the spectator nucleus and initiate intranuclear cascade processes. The treatment of elastic and inelastic interactions with spectator nucleons is based on measured cross sections and interaction channels as they are implemented in the MC model HADRIN [201] for energies below  $E_{\text{Lab}} = 5$  GeV. Here, HADRIN is applied to hadron–nucleon interactions up to 9 GeV and those at higher energies are neglected. Reinteractions at energies above 5 GeV occur much less frequently than reinteractions below 5 GeV and a more detailed treatment would not change the results discussed in this chapter [57]. Furthermore the annihilation of antiprotons and the absorption of low-energy mesons by interactions with two nucleons is taken into account. For pion absorption the cross section parametrization given in [202] is used. If the secondary hadron did not reinteract, in a second attempt a cascade step in the rest frame of the other spectator nucleus is considered. Likewise, this formalism is also applied to all particles produced in intranuclear cascade processes.

Note that the proposed scheme is not Lorentz invariant. The dependence of the results on the choice of the particular Lorentz frame however is assumed to be small. A generally possible but technically cumbersome Lorentz invariant formulation of the intranuclear cascade is therefore avoided within the present approach [57].

## 4.2 Calculation of Nuclear Excitation Energies

It is assumed that nucleons of a nucleus with mass number  $A$  and charge  $Z$  move in a flat effective nuclear potential  $V_i$  ( $i$ =proton,neutron) defined by a Fermi-energy and a binding energy contribution [56,57]

$$V_i(A, Z) = \frac{[p_i^{\text{F}}(A, Z)]^2}{2m_i} + E_i^{\text{bind}}(A, Z), \quad (4.7)$$

with

$$\begin{aligned}
p_i^{\text{F}}(A, Z) &= \alpha_{\text{mod}}^{\text{F}} \left[ \frac{3\pi^2 N_i}{\Phi_A} \right]^{\frac{1}{3}}, \\
E_p^{\text{bind}}(A, Z) &= E_{\text{bind}}(A, Z) - E_{\text{bind}}(A-1, Z-1), \\
E_n^{\text{bind}}(A, Z) &= E_{\text{bind}}(A, Z) - E_{\text{bind}}(A-1, Z),
\end{aligned} \tag{4.8}$$

and  $N_p = Z$ ,  $N_n = A - Z$ .  $\Phi_A$  approximates the volume of the nucleus using a nuclear radius  $R_A = r_0 A^{1/3}$ ,  $r_0 = 1.29$  fm. The total nuclear binding energy is denoted by  $E_{\text{bind}}$ . Deviations of this approximation from the actual nuclear potential which arise by, for instance, neglecting nuclear skin effects are taken into account by the factor  $\alpha_{\text{mod}}^{\text{F}}$ . This factor influences indirectly black particle production. It is adjusted by comparing the results of the model with data (see Sec. 4.4.1) and is fixed at 0.65. The Coulomb-barrier acting on charged particles is given by

$$V_{\text{C}}(A, Z) = \frac{e^2}{4\pi\epsilon_0 r_0} \frac{Z}{(1 + A^{1/3})} \tag{4.9}$$

where  $e$  is the elementary charge.

Due to the primary nucleon–nucleon interactions according to the Glauber–Gribov formalism and due to intranuclear cascade processes the colliding nuclei lose a part of their nucleons. These nucleons and those secondary hadrons which were formed inside one of the nuclei eventually leave the corresponding effective nuclear potential and lose a fraction of their energy. Within the assumed simplified approach the precise nuclear potential of a spectator nucleus during or after the primary or secondary interactions cannot be predicted. For baryons<sup>2</sup> the potential is approximated by Eqs.(4.7) and (4.8) at a mass number  $A_{\text{pre}}$  and charge  $Z_{\text{pre}}$  of the corresponding prefragment. To account for the deformation of the prefragments a modification factor  $\tilde{\alpha}_{\text{mod}}^{\text{F}} = \alpha_{\text{mod}}^{\text{F}} + 0.1$  is used instead of  $\alpha_{\text{mod}}^{\text{F}}$  in Eq.(4.8). In case of mesons a flat effective potential of 0.002 GeV is applied.

If a hadron leaves the nuclear potential of a prefragment, a recoil momentum is transferred to this prefragment. Adding up the recoil 4-momenta of all these hadrons separately for the projectile and target spectators ( $E_{\text{rcl}}, \vec{p}_{\text{rcl}}$ ) one obtains the 4-momenta of the prefragments (in the rest frame of the corresponding nucleus)

$$(E_{\text{pre}}, \vec{p}_{\text{pre}}) = (M_A, \vec{0}) - \sum_{i=1}^{\nu_w} (E_i^{\text{F}}, \vec{p}_i^{\text{F}}) + (E_{\text{rcl}}, \vec{p}_{\text{rcl}}) . \tag{4.10}$$

where  $\nu_w$  is the number of wounded nucleons in the corresponding nucleus and  $M_A$  is its mass. Indices referring the quantities to projectile and target are omitted for simplicity.

The excitation energy  $U$  of a prefragment is defined as the energy above the ground state mass  $M_0$

$$U = M_{\text{pre}} - M_0(A_{\text{pre}}, Z_{\text{pre}}) \tag{4.11}$$

---

<sup>2</sup>The fraction of baryons other than nucleons which are created inside of one of the nuclei is small. They are assumed to move in a nucleon potential

with

$$M_{\text{pre}} = \sqrt{E_{\text{pre}}^2 - \vec{p}_{\text{pre}}^2},$$

$$M_0(A_{\text{pre}}, Z_{\text{pre}}) = Z_{\text{pre}}m_p + (A_{\text{pre}} - Z_{\text{pre}})m_n - E_{\text{bind}}(A_{\text{pre}}, Z_{\text{pre}}). \quad (4.12)$$

The binding energy  $E_{\text{bind}}$  is either taken to be the experimentally determined excess mass or is obtained from mass formulas for nuclides far from the stable region.

To outline the qualitative features of the model hadron–nucleus collisions are considered first. Average excitation energies per nucleon of the target prefragments are shown in Fig. 4.1 as a function of the proton momentum for various target nuclei. Up to a mo-

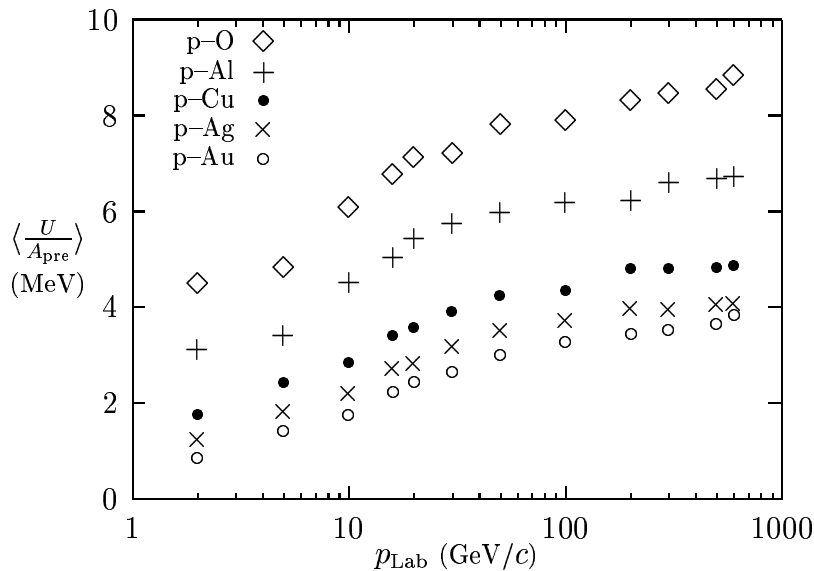


Figure 4.1: Average excitation energies per nucleon of the target prefragments are given for different laboratory momenta in proton–nucleus interactions.

mentum of about 50 GeV/c the excitation energy per nucleon increases which is mainly due to a rising number of interactions of the projectile proton with nucleons [56]. This behavior will be discussed in more detail in a later section with respect to experimental information on target associated particle production. At higher energies, the average excitation energy per nucleon becomes approximately energy-independent as it is expected from limiting fragmentation [203]. The decrease of  $\langle U/A_{\text{pre}} \rangle$  with target mass at a fixed projectile momentum can be understood from the smaller fraction of wounded nucleons to all target nucleons for heavy nuclei as compared to light nuclei.

Within the model the average excitation energy of a prefragment is correlated to the number of nucleons involved in the interaction. The more nucleons are removed from the nucleus, the higher the excitation of the spectator part becomes. In Fig. 4.2 average excitation energies of target prefragments from interactions of protons with nuclei of mass number  $A$  at 300 GeV/c are shown. In the plot different symbols correspond to different numbers of nucleons  $\Delta A$  lost by the target. At fixed  $\Delta A$  the excitation energy rises with the target mass number, since in heavy targets more cascade interactions are needed to remove a certain number of nucleons than in light targets.

In Fig. 4.3 distributions of excitation energies per nucleon of the target prefragment are shown as an example for proton–gold interactions at 300 GeV/c. Together with the distribution referring to all prefragment masses (labelled “all  $A_{\text{pre}}$ ”), two further distributions are given which correspond to different mass ranges. Again, the more nucleons are

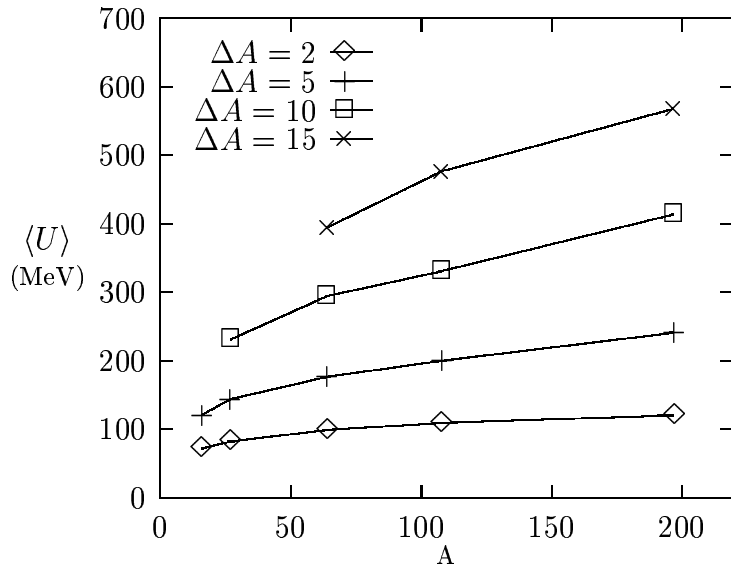


Figure 4.2: Dependence of the average excitation energies of target prefragments with mass number  $A_{pre}$  on the target mass number. Model results are shown for proton–nucleus interactions at  $p_{Lab} = 300$  GeV/c and for different  $\Delta A = A - A_{pre}$ .

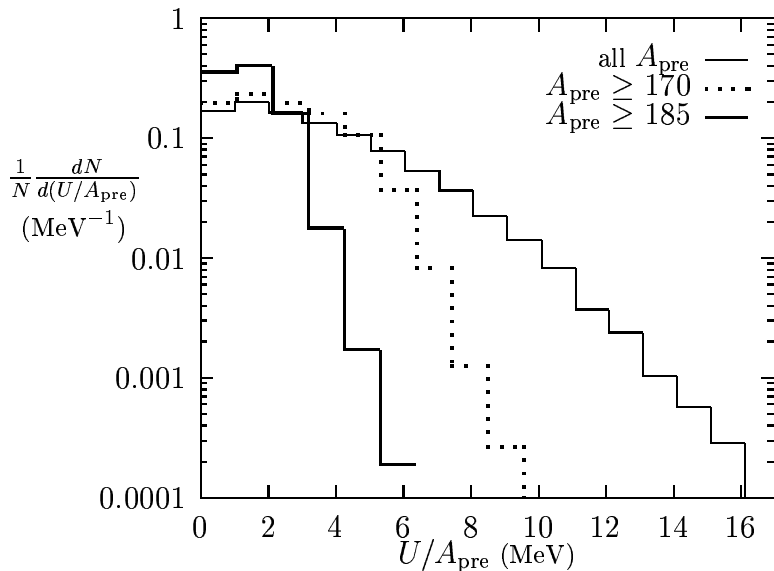


Figure 4.3: Distributions of the excitation energy per nucleon of prefragments from proton–gold interactions at  $p_{Lab} = 300$  GeV/c.

involved in the primary interaction and the intranuclear cascade the higher is the mean excitation energy and the broader is the excitation energy distribution.

Finally in Table 4.1 average excitation energies and excitation energies per nucleon of target prefragments are given for interactions of oxygen and aluminum with gold nuclei at different energies. In asymmetric nucleus–nucleus interactions the excitation energies per nucleon of the prefragments of the heavier nucleus are increasing slowly with beam energy and, at a fixed energy, with the mass number of the projectile.

## 4.3 Nuclear Disintegration of Spectator Prefragments

### 4.3.1 Evaporation and High-Energy Fission

In the model the evaporation process starts from a prefragment of mass  $A_{pre}$ , charge  $Z_{pre}$ , and excitation energy  $U$  which is assumed to be in an equilibrium state. The emission of a particle of type  $j$  is possible if the excitation energy exceeds a minimum energy  $Q_j$

$p_{\text{Lab}}$ (A GeV/c)	O-Au		Al-Au	
	$\langle U \rangle$ (MeV)	$\langle \frac{U}{A_{\text{pre}}} \rangle$ (MeV)	$\langle U \rangle$ (MeV)	$\langle \frac{U}{A_{\text{pre}}} \rangle$ (MeV)
30	554.0	5.5	537.0	6.0
50	567.0	5.6	546.0	6.2
100	567.0	5.7	573.0	6.7
500	603.0	6.4	606.0	7.1
1000	619.0	6.6	621.0	7.3
2000	653.0	6.7	652.0	7.7

Table 4.1: Average excitation energies and excitation energies per nucleon of target prefragments produced in oxygen- and aluminum-gold interactions before evaporation. The excitation energies are given for different momenta per nucleon of the projectile nucleus.

necessary for this process. Its probability can be derived applying the balance principle

$$P^{(i \rightarrow f)} \rho_i = P^{(f \rightarrow i)} \rho_f, \quad (4.13)$$

which relates the probabilities  $P$  for the transition from system  $i$  to system  $f$  and vice versa to the density of states  $\rho$  in the two systems. The probability  $P_j(E_{\text{kin}})$  for the emission of a particle  $j$ , with kinetic energy  $E_{\text{kin}}$ , mass  $m_j$  and spin  $S_j$  is given by

$$P_j(E_{\text{kin}}) dE_{\text{kin}} = \frac{(2S_j + 1)m_j}{\pi^2} \frac{\rho_f(U_f)}{\rho_i(U_i)} \sigma_{\text{inv}}(E_{\text{kin}}) E_{\text{kin}} dE_{\text{kin}}. \quad (4.14)$$

Here,  $\rho_i$ ,  $U_i \equiv U$  and  $\rho_f$ ,  $U_f = U - E_{\text{kin}} - Q_j$  are the nuclear level densities and excitation energies of the prefragment before and after the evaporation step.  $\sigma_{\text{inv}}$  denotes the cross section of the inverse process, i.e. for the capture of particle  $j$ .

Within a MC treatment of the evaporation process, Eq.(4.14) has to be implemented together with suitable expressions for the nuclear level density and the inverse cross sections. Many formulations have been suggested for both. In [204] an excitation energy dependence of the level density of the form  $\rho(U) = C \exp(2\sqrt{aU})$  with  $a = A/8$  and an analytically integrable parametrization for  $\sigma_{\text{inv}}$  are proposed which lead to an emission probability

$$P_j(E_{\text{kin}}) dE_{\text{kin}} = \frac{(2S_j + 1)m_j}{\pi^2} \frac{e^{2\sqrt{a(U - E_{\text{kin}} - Q_j)}}}{e^{2\sqrt{aU}}} \sigma_{\text{inv}}(E_{\text{kin}}) E_{\text{kin}} dE_{\text{kin}}. \quad (4.15)$$

We adopt this formulation, however, with a different choice of the level density parameter  $a$  as will be discussed further below. Then the total width for neutron emission, for instance, is obtained by integrating Eq.(4.14) between zero and the maximum possible neutron energy ( $U - Q_n$ )

$$\Gamma_n = \int_0^{(U - Q_n)} P_n(E_{\text{kin}}) dE_{\text{kin}} = \frac{(2S_n + 1)m_n}{\pi^2 \rho(U)} \int_0^{(U - Q_n)} \rho(U - E_{\text{kin}} - Q_n) \sigma_{\text{inv}}(E_{\text{kin}}) E_{\text{kin}} dE_{\text{kin}}. \quad (4.16)$$

The same applies to charged particles where the integration is performed between an energy given by the effective Coulomb barrier (defined by  $\sigma_{\text{inv}} \rightarrow 0$ ) and the maximum energy. In the MC realization the evaporation of nucleons, deuterium,  ${}^3\text{H}$ ,  ${}^3\text{He}$ , and of  $\alpha$ -particles is included.

In addition to the evaporation process fission is also considered [205]. A fraction of the excitation energy might be spent to induce a collective deformation. As the shape of the prefragment deviates from sphericity the surface energy increases but the Coulomb energy decreases. The deformation state of maximum potential energy is called ‘‘saddle point’’. The fission barrier  $B_{\text{F}}$  is defined as the difference between the potential energy at the saddle point and the ground state energy. In order to calculate the fission probability a statistical method can be used [206,207] resulting in a total fission width

$$\Gamma_{\text{F}} = \frac{1}{2\pi\rho(U)} \int_0^{(U-B_{\text{F}})} \rho_{\text{F}}(U - E_{\text{kin}} - B_{\text{F}}) dE_{\text{kin}} . \quad (4.17)$$

Here,  $\rho_{\text{F}}(U) \approx C \exp(2\sqrt{a_{\text{F}}U})$  is the level density of the prefragment at the saddle point which is different from that of the nucleus in its ground state because of deformation. The quantities entering Eq.(4.17) (except  $a_{\text{F}}$ ) are calculated according to the prescriptions given in [208]. The masses of the two fragments obey  $Z_{\text{pre}}$ - and  $U$ -dependent distributions [209]. After the fission process both fragments are treated independently, possibly being able to emit further particles themselves.

Finally for the nuclear level densities  $\rho$  and  $\rho_{\text{F}}$  the following assumptions are made: The ‘‘odd–even effect’’ is taken into account by calculating both quantities at  $U - \Delta$  instead of  $U$ , with  $\Delta$  being the pairing energy (‘‘back-shifted’’ level density). Moreover due to shell and deformation effects the level density parameters  $a$  and  $a_{\text{F}}$  depend on the mass, charge and excitation energy of the evaporating nucleus. Here the  $A_{\text{pre}}$ - and  $Z_{\text{pre}}$ -dependence as suggested in [210] together with the  $U$ -dependence of [211,212] are applied

$$a = A_{\text{pre}} (\bar{a}f(U) + \tilde{a} [1 - f(U)]) \quad (4.18)$$

with

$$\begin{aligned} \bar{a} &= a_0 + 9.17 \times 10^{-3} \cdot (S_{\text{Z}}(Z_{\text{pre}}) + S_{\text{N}}(A_{\text{pre}} - Z_{\text{pre}})), \\ \tilde{a} &= 0.154 - 6.3 \times 10^{-5} \cdot A_{\text{pre}}, \\ f(U) &= \frac{1 - \exp[-0.054 \cdot (U - \Delta)]}{0.054 \cdot (U - \Delta)} \end{aligned} \quad (4.19)$$

where, according to [210],  $a_0 = 0.142 \text{ MeV}^{-1}$  for undeformed nuclei and  $a_0 = 0.12 \text{ MeV}^{-1}$  for deformed nuclei.  $S_{\text{Z}}$  and  $S_{\text{N}}$  are shell correction terms for protons and neutrons. The unit of energy used throughout Eqs.(4.18) and (4.19) is MeV. As already mentioned the level density at the saddle point  $\rho_{\text{F}}$  is different from that of the nucleus in its ground state. From comparison to experimental data, it turned out that  $a_{\text{F}}$  is bigger than  $a$  by about 10% at low excitation energies ( $a_{\text{F}} \approx 1.08a$ ) and becomes about equal to  $a$  at high excitation energies.

### 4.3.2 The Fermi Break-up Model

For light prefragments the statistical assumptions and the sequential emission scheme underlying classical evaporation models may become invalid:

- A moderate excitation energy can already represent a substantial fraction of the (total) binding energy.
- The level structure is usually highly nucleus-specific and level spacings can be of the order of the excitation energy.
- The “evaporation” of light fragments other than protons or neutrons becomes meaningless since the mass of the “emitted” fragment can be comparable to the mass of the prefragment.

Other mechanisms describing the break-up of these light prefragments might therefore be more appropriate. In the present calculations, the so called Fermi Break-up model [213,214] is applied if  $A_{\text{pre}} \leq 17$ . In this model it is assumed that the excited prefragment disassembles in one step into two or more fragments. The probability for the break-up of a prefragment of mass  $M_{\text{pre}}$  (Eq.(4.12)) into  $n$  fragments ( $n \geq 2$ ) can be written as

$$W = \frac{g}{G} \left[ \frac{V_{\text{br}}}{(2\pi)^3} \right]^{n-1} \left( \frac{1}{M_{\text{pre}}} \prod_{i=1}^n m_i \right)^{\frac{3}{2}} \frac{(2\pi)^{\frac{3}{2}(n-1)}}{\Gamma(\frac{3}{2}(n-1))} E_{\text{kin}}^{\frac{3n-5}{2}} \quad (4.20)$$

where the spin factor  $g$  and the permutation factor  $G$  are given by ( $n_j$  is the number of identical particles of the  $j$ th kind)

$$g = \prod_{i=1}^n (2S_i + 1), \quad G = \prod_{j=1}^k n_j! \quad (4.21)$$

and  $E_{\text{kin}}$  is the total kinetic energy of all fragments at the moment of break-up.  $V_{\text{br}}$  is a volume of the order of the prefragment volume. All combinations formed by up to six fragments are considered. All stable nuclei with  $A \leq 16$  and a few known unstable isotopes, like  ${}^8\text{Be}$ , have been included. The latter are allowed to decay according to the experimentally measured branching ratios. Once a final state configuration has been selected the kinematic quantities of each fragment are chosen according to  $n$ -body phase space distributions taking Coulomb repulsion of all charged particles into account [209].

### 4.3.3 De-excitation by Photon Emission

Evaporation processes become energetically impossible when the nuclear excitation energy of a prefragment with mass number  $A$  is lower than any energy necessary for nucleon or fragment emission. The residual excitation energy is then dissipated through the emission of photons. In general photon emission occurs even during the evaporation stage but with a probability which is low in comparison to particle emission. This is therefore neglected in the model.

$\gamma$  de-excitation proceeds through consecutive photon emissions until the ground state of an isotope corresponding to the mass and charge of the prefragment is reached. It is assumed to be a statistical process as long as the excitation energy is high enough to allow the definition of a continuous nuclear level density. Below a certain threshold transitions between discrete levels determine the de-excitation process. This threshold is chosen to be equal to the pairing energy for even–even or even–odd prefragments or to be the first known (or approximated) excited level for odd–odd prefragments.

The statistical formulation of the photon emission probability is similar to the one for evaporation and fission (Eq.(4.14)) [215,216]:

$$P(E_\gamma) dE_\gamma = \frac{\rho(U_f)}{\rho(U_i)} \sum_L f(E_\gamma, L) dE_\gamma \quad (4.22)$$

where  $P(E_\gamma)$  is the probability for the emission of a photon with energy  $E_\gamma$  and  $L$  is the multipolarity of the  $\gamma$ -transition. Again  $\rho$  denotes the nuclear level density. The functions  $f(E_\gamma, L)$  can be either derived from photoabsorption cross sections or calculated from single-particle estimates of transition strengths. The former approach is more sophisticated but requires the knowledge of the resonance parameters for all isotopes. The latter approach however is sufficient for a first order estimate of the spectral photon distribution and is therefore adopted in the present formulation of the model:

$$f(E_\gamma, L) = c_L \cdot F_L(A) \cdot E_\gamma^{(2L+1)} . \quad (4.23)$$

For the coefficients  $c_L$  the single particle estimates given in [217] are used. The factors  $F_L(A)$  are included to partially account for effects which cause deviations from the single particle estimates. They represent  $A$ -dependent averages of the hindrance and enhancement factors given in [218]. Only E1, M1 and E2 transitions are considered. For the level density  $\rho$  the same expression as within the evaporation treatment (Sec. 4.3.1) is used:  $\rho(U) \propto \exp(2\sqrt{a(U - \Delta)})$ . Expanding in Eq.(4.22) the ratio of nuclear level densities  $\rho(U - E_\gamma)/\rho(U)$  at  $E_\gamma = 0$  one obtains  $\rho(U - E_\gamma)/\rho(U) \approx \exp(-E_\gamma/T)$ . The quantity  $T$  is called nuclear temperature. The expansion is equivalent to the assumption of a constant nuclear temperature at low excitation energies ( $U - \Delta = aT^2$ ) which is often used in the analysis of photon emission following neutron capture [215,219]. Thus the probability for a  $\gamma$ -transition of multipolarity  $L$  reads

$$P(L, E_\gamma) dE_\gamma = \tilde{C}_L E_\gamma^{(2L+1)} e^{-E_\gamma/T} dE_\gamma . \quad (4.24)$$

Since competition between photon and particle emission is neglected only ratios of coefficients  $\tilde{C}_L$  are of interest

$$\begin{aligned} \frac{\tilde{C}_{M1}}{\tilde{C}_{E1}} &= 0.31 A^{-\frac{2}{3}} \frac{F_{M1}(A)}{F_{E1}(A)}, \\ \frac{\tilde{C}_{E2}}{\tilde{C}_{E1}} &= 7.2 \cdot 10^{-7} A^{\frac{2}{3}} \frac{F_{E2}(A)}{F_{E1}(A)} \text{ MeV}^{-2}. \end{aligned} \quad (4.25)$$

Within the MC realization of the de-excitation process, for each photon emission (i) the character (electric or magnetic) and the multipole order of the emitted photon is sampled from integrated emission probabilities, and (ii) the emission energy is sampled according to the selected multipolarity. After emission all parameters are updated on the basis of the new excitation energy, and another statistical emission is performed until the excitation energy is lower than the above mentioned threshold value. In order to sample the discrete transitions the experimentally determined values of the first and second excited levels have been tabulated in the code for many isotopes. For other isotopes a rotational-like structure is assumed.

All photons are emitted isotropically since from the evaporation stage no information on the prefragment spin and polarization is available.

## 4.4 Comparison to Experimental Data

As discussed in Sec. 4.1.2 nucleons might be knocked out of a spectator nucleus by intranuclear cascade processes if their energies are sufficiently high to allow the escape from the nuclear potential. In the rest frame of the nucleus considered these nucleons appear as final state particles with energies of the order of 20–400 MeV. By contrast most of the nucleons and light fragments evaporated from the excited prefragment possess less energy. This fact allows to study both mechanisms of low-energy (“slow”) particle production rather independently. In the model the cascade particles contribute of course to the excitation of the prefragment and, therefore, indirectly to the total multiplicity of evaporation products.

All models on slow particle production discussed in the previous sections have been implemented into the event generators DPMJET-II and DTUNUC 2.0. In this section results obtained with DTUNUC 2.0 are compared to data from target associated particle production in hadron–nucleus and nucleus–nucleus collisions.

At present most of the experimental information on slow particle production comes from experiments using nuclear emulsions as targets. Nuclear emulsions consist of a component of light nuclei (hydrogen, carbon, nitrogen and oxygen) and a component of heavy nuclei (silver and bromine). Their quantitative composition is usually about 28.6% light and 71.4% heavy nuclei. The appearance of slow charged hadrons and nuclear fragments in the emulsions has led to their subdivision into “grey” and “black” particles. Grey and black particles roughly coincide in energy with the above mentioned cascade and evaporation particles and are sometimes grouped together as “heavy” particles. All charged hadrons with higher energies are frequently called “shower” particles. The exact definitions for the different classes of particles vary slightly between different experiments. For instance a common way to distinguish between heavy and shower particles is to apply a cut in the Lorentz- $\beta$  variable at a value of 0.7. A considerable disadvantage of emulsion experiments arises from the fact that neither final state particle nor target identification is unambiguously possible for a certain event.

### 4.4.1 Hadron–Nucleus Interactions

#### Slow particle multiplicities and correlations

In Fig. 4.4 average multiplicities of shower, grey and heavy particles in proton–emulsion interactions as obtained with DTUNUC 2.0 are compared to data at different momenta of the projectile proton. In the calculations heavy particles are defined as charged hadrons and fragments with  $\beta \leq 0.7$  and grey particles are charged hadrons with  $0.23 \leq \beta \leq 0.7$ . Whereas the average number of shower particles is increasing with rising proton momentum throughout the whole momentum range the grey and heavy particle multiplicities increase only up to about 40 GeV/ $c$  and then remain at an almost constant value for higher momenta. Within the model this constant behavior is due to (i) limiting fragmentation in each hadron–nucleon interaction [203] together with a constant formation zone intranuclear cascade and (ii) inelastic hadron–nucleus cross sections which depend only weakly on the projectile energy. The energy range of the transition between rising and almost constant heavy particle multiplicities is governed by the nuclear geometry and the nuclear potential which both are treated very roughly and by kinematical limitations

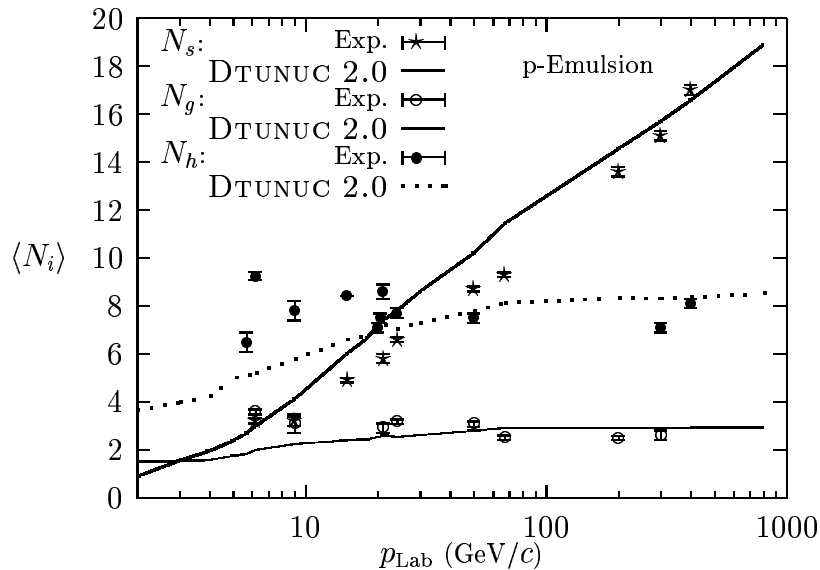


Figure 4.4: Average multiplicities of shower  $\langle N_s \rangle$ , grey  $\langle N_g \rangle$  and heavy particles  $\langle N_h \rangle$  in collisions of protons with emulsion nuclei. Data from various experiments (points, [195] and references therein) are compared to results of the model (lines).

biasing the Glauber-cascade. For instance, further shifts in energy or modifications of the shape of this transition region can be obtained by modifying the momentum fraction distributions of the sea-partons. The experimental data shown in Fig. 4.4 are taken from a compilation by Fredriksson *et al.* [195], i.e. they are from different experiments using different definitions for “grey” and “heavy”. This may partly account for the fluctuations within the data for grey and heavy particle multiplicities. The agreement between data and model results is satisfactorily for shower particle multiplicities at all considered energies and for slow particle multiplicities at momenta above about 20 GeV/c. At lower momenta the calculated values for  $\langle N_h \rangle$  and  $\langle N_g \rangle$  depart from the data which may indicate that the model does not describe the low-momentum region appropriately. However the fluctuations within the data at low energies are considerable and cannot be completely explained by differences within the definitions of “grey” and “heavy”. Based on this comparison it is therefore difficult to decide if the models in their present realizations provide an adequate description of slow particle production at low energies and which modifications could be necessary to reproduce the observed transition behavior.

More information in this respect can be expected if the interactions with the light and heavy emulsion components are studied separately. Experimentally, events are assigned to one of the two target classes by applying certain cuts to observables characterizing the final state, such as the heavy particle multiplicity. However, these additional assumptions induce further uncertainties. For instance, peripheral collisions with heavy target nuclei may have final states which are similar to those of collisions with nuclei of the light component so that the former might be misidentified as interactions with light nuclei. Results on average shower, grey and heavy particle multiplicities are shown together with data [195] for interactions with light targets in Fig. 4.5 and for interactions with the heavy component in Fig. 4.6. For some momenta several multiplicity values obtained in different experiments are given in order to illustrate the uncertainties within the experimental data. As it is clearly shown in Fig. 4.5, in collisions with light nuclei the proton interacts with only up to three target nucleons throughout the whole momentum range. Hence the typical “breakdown” of the Glauber-cascade as seen in interactions with heavy nuclei at low energies, which also manifests itself in decreasing slow particle multiplicities

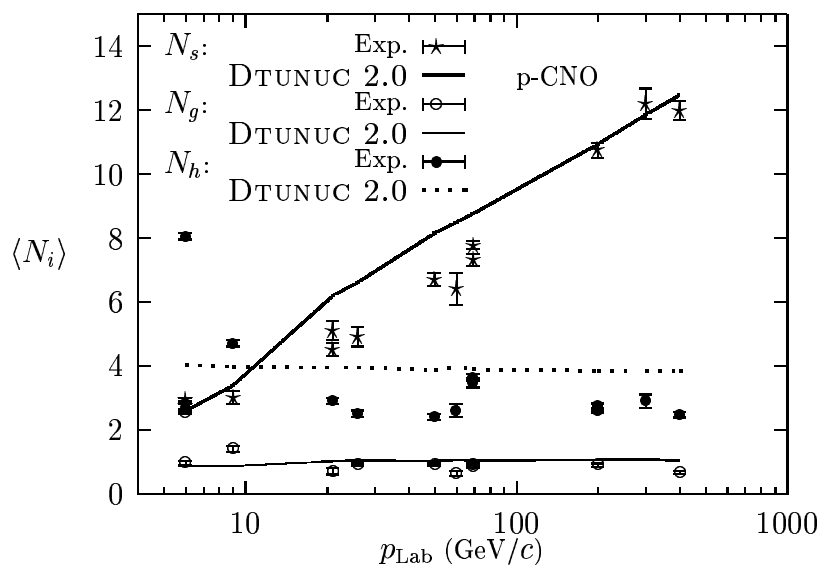


Figure 4.5: As in Fig. 4.4, here shown for the emulsion component consisting of light nuclei (C,N,O).

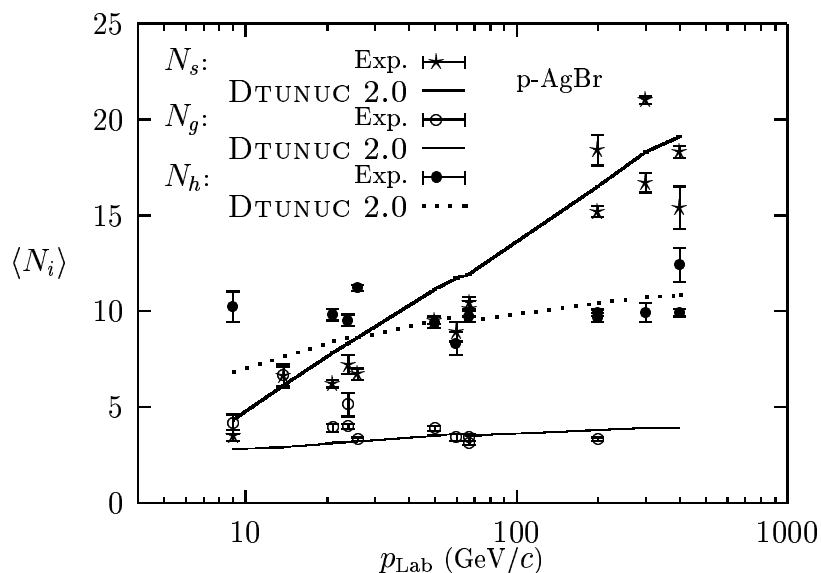


Figure 4.6: As in Fig. 4.4, here shown for the emulsion component consisting of heavy nuclei (Ag,Br).

is much less pronounced. In agreement with the measurements the calculated slow particle multiplicities are constant within the plotted momentum range. The heavy particle multiplicities in Fig. 4.5 are overestimated by the models which might be explained by the absence of nuclear skin effects in the treatment of the nuclear potential. This approximation causes an underestimation of low excitation energies and therefore an overestimation of the average number of black particles among the heavy particles. Good agreement of calculations and data is obtained for the shower and grey particle multiplicities and for the heavy particle multiplicities from p-Ag/Br collisions down to about 20 GeV/c.

A detailed experimental study of slow particle production in interactions of protons, pions and kaons with different target nuclei at 50, 100 and 150 GeV can be found in [220]. The comparison with calculated grey particle multiplicities given in Table 4.2 demonstrates that the discussed models are able to describe the experimentally observed average multiplicities and their increase with the target mass number. Here the energy range of grey particles is restricted to  $0.3 \leq \beta \leq 0.7$ .

In contrast to average quantities, grey and black particle multiplicity distributions

	$E_{\text{Lab}}=50$ GeV		$E_{\text{Lab}}=100$ GeV		$E_{\text{Lab}}=150$ GeV	
	DTUNUC	Exp.	DTUNUC	Exp.	DTUNUC	Exp.
p-C	0.74	$0.91 \pm 0.05$	0.73	$0.82 \pm 0.04$	0.77	$0.89 \pm 0.04$
p-Cu	2.2	$2.23 \pm 0.11$	2.2	$2.26 \pm 0.11$	2.3	$2.27 \pm 0.11$
p-Pb	4.6	$4.04 \pm 0.2$			4.5	$3.75 \pm 0.19$
$\pi^+$ -C	0.69	$0.85 \pm 0.04$	0.69	$0.81 \pm 0.04$	0.64	$0.84 \pm 0.04$
$\pi^+$ -Cu	1.96	$1.99 \pm 0.1$	1.98	$2.04 \pm 0.1$	1.97	$1.99 \pm 0.1$
$\pi^+$ -Pb	4.0	$3.42 \pm 0.17$	3.9	$2.89 \pm 0.14$	3.9	$3.31 \pm 0.17$
$K^+$ -C	0.65	$0.81 \pm 0.04$			0.67	$0.80 \pm 0.04$
$K^+$ -Cu	1.82	$1.92 \pm 0.1$			1.76	$1.93 \pm 0.1$
$K^+$ -Pb	3.62	$3.43 \pm 0.17$			3.77	$3.23 \pm 0.16$

Table 4.2: Calculated average grey particle multiplicities for interactions of protons, pions and kaons with nuclei at different energies are compared to data [220].

may provide a more severe check of the models. They are shown in Fig. 4.7 for proton-emulsion interactions at 200 GeV. Again, a good description of the data [221] is obtained.

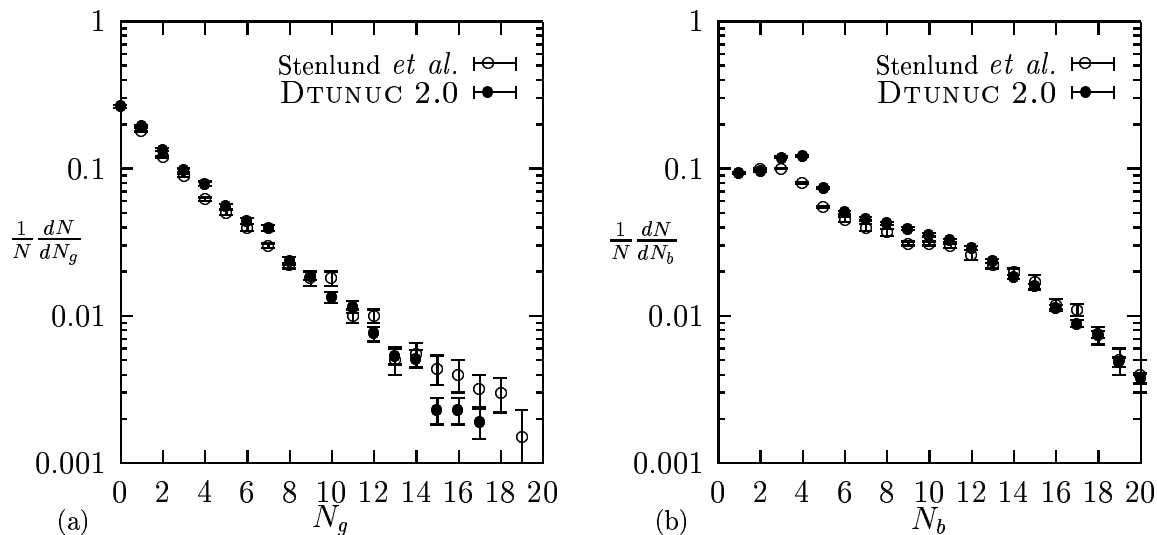


Figure 4.7: Grey (a) and black (b) particle multiplicity distributions for interactions of protons with emulsion nuclei at  $E_{\text{Lab}} = 200$  GeV. Model results are shown together with data [221].

The hump in the calculated black particle distribution (b) at  $N_b \approx 4$  is caused by protons and fragments evaporated from prefragments of the light emulsion component. It is less pronounced in the measured distribution.

So far only multiplicities of all slow charged particles were considered. A deeper insight into the intranuclear interaction mechanisms might be gained if protons, which

constitute the majority of grey particles, and slow charged pions are studied separately. As mentioned at the beginning emulsion experiments do not allow such investigations. The only experimental results available in this respect were obtained by the WA80-Collaboration which studied the production of slow protons in 200 GeV proton- and pion-nucleus interactions [222]. As an example, in Fig. 4.8 multiplicity distributions of slow protons and singly charged fragments are shown for pion-induced interactions. Cor-

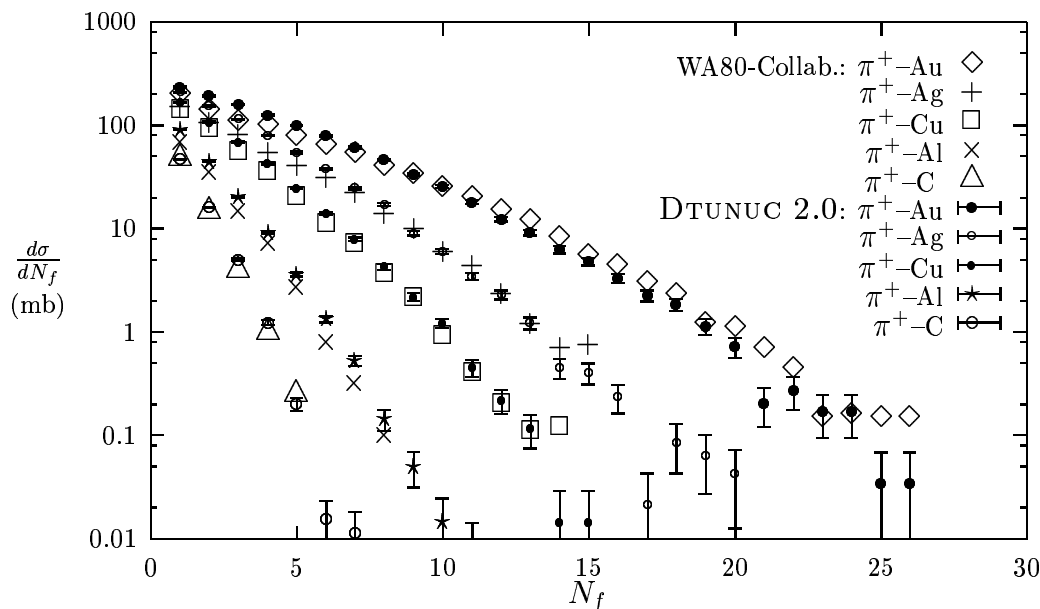


Figure 4.8: Calculated multiplicity distributions of slow protons and singly charged fragments from pion-nucleus interactions at 200 GeV are compared to results of the WA80-Collab. [222].

responding to the experimental conditions the kinematic range considered is restricted to  $30 \leq E_{\text{kin}} \leq 400$  MeV and  $-1.7 < \eta < 1.3$ . The agreement between calculations and data is satisfactorily.

The reasonable description of slow particle multiplicity distributions implies that it should be equally well possible to reproduce measured correlations between grey, black and shower particle multiplicities. This is shown in Figs. 4.9 and 4.10 in comparison with data on proton-emulsion interactions at 200 GeV [223]. A good agreement between calculated and measured correlations is obtained.

### The production of residual nuclei

Studying the mass yield of fragments produced in interactions of a high-energy hadrons with a heavy target nuclei ( $A \gtrsim 200$ ) three fragment mass regions are commonly distinguished and assigned to certain interaction or fragmentation mechanisms [194] ( $A_f$  denotes the fragment mass):

1.  $A_f \gtrsim 2/3A$ : One heavy fragment is formed which has a mass close to the target mass (*spallation* region).
2.  $50 \lesssim A_f \lesssim 2/3A$ : This region is mainly populated by fragments produced in *fission* and so-called *deep spallation* processes. Fission processes result in two heavy

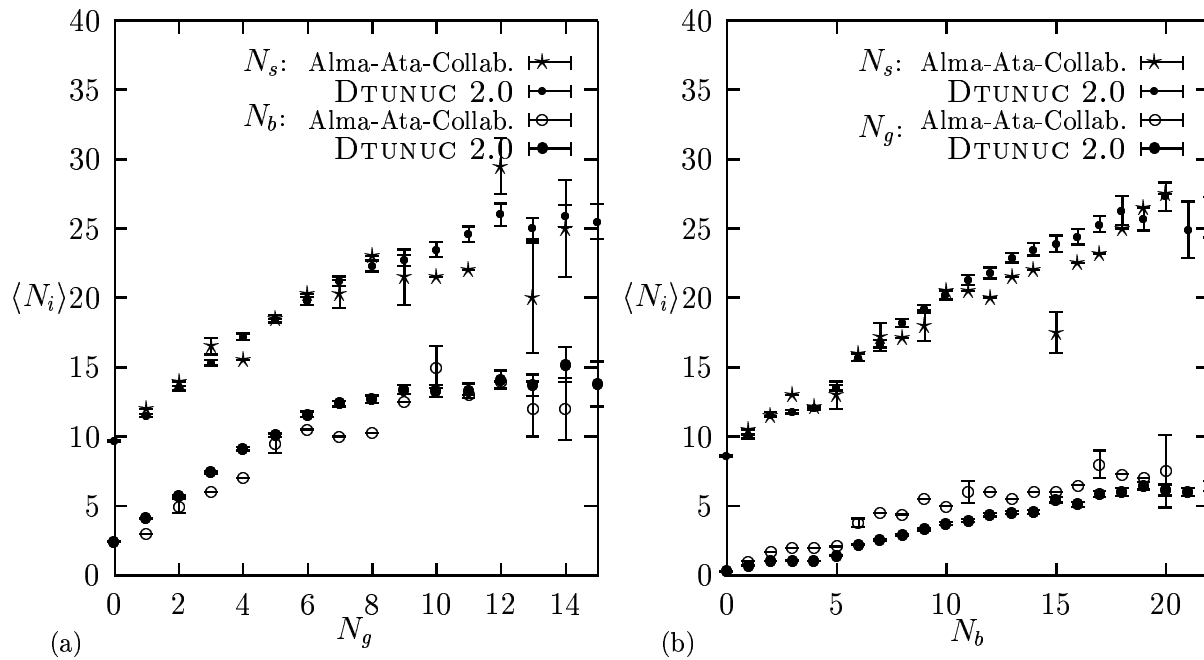


Figure 4.9: Correlations between shower ( $N_s$ ), grey ( $N_g$ ) and black ( $N_b$ ) particle multiplicities. Model predictions are compared to data from proton–emulsion interactions at 200 GeV [223].

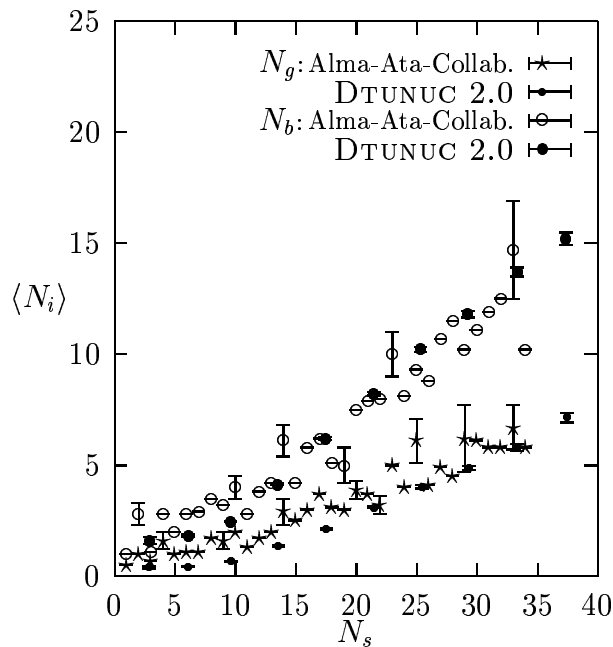


Figure 4.10: As in Fig. 4.9. Here, the dependence of the average grey and black particle multiplicities on the number of shower particles is compared to data [223].

fragments with  $A_f \approx A/2$  whereas deep spallation might be understood as a continuation of spallation towards lower fragment masses.

3.  $A_f \lesssim 50$ : During the interaction many fragments with relatively low masses are produced (*multifragmentation region*).

For smaller targets spallation and multifragmentation dominate the mass yield.

In an interaction with a high-energy hadron a heavy target nucleus loses a part of its nucleons due to the interactions of the hadron inside the nucleus and the subsequent intranuclear cascade. In the present description of prefragment disintegration the excited prefragment may then either (i) dissipate its excitation energy by evaporating nucleons and light fragments leaving a residual nucleus in the spallation or deep spallation regions 1 and 2 (depending on the impact parameter of the collision) or (ii) undergo fission and subsequent evaporation processes contributing two fragments to region 2. Taking into account that a model for multifragmentation (which mainly describes fragment production in region 3 but also modifies the yields in the other two regions) is not implemented in DTUNUC one may expect that the measured cross sections in region 1 and 2 are reproduced within a factor of two whereas no prediction can be made for region 3. This is shown in Fig. 4.11 for proton–gold interactions at 800 GeV. In order to indicate the

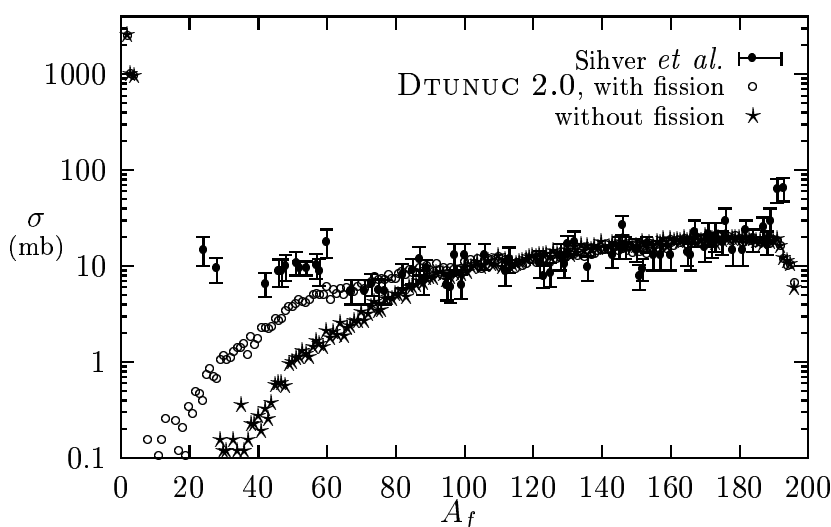


Figure 4.11: Cross sections for the production of fragments with mass number  $A_f$  in proton–gold interactions at 800 GeV. Model results obtained taking fission processes into account and neglecting fission are compared to data [224].

influence of high-energy fission on the predicted cross sections the mass yield calculated without sampling fission processes is plotted in addition. The cross sections for the production of fragments with masses in the range  $A - 5 \lesssim A_f \leq A$  are not reproduced in the model. Probable reasons are the neglect of quasi-elastic hadron–nucleus scattering and of nuclear skin effects within the nuclear potential. The latter leads to an underestimation of prefragments with very low excitation energies. In Fig. 4.12 cross sections for the production of fragments with charge  $Z_f$  in proton–gold collisions at 10.6 GeV are compared to data [225,226]. In agreement with the observation that the cross sections for fragment production remain constant above about 10 GeV projectile energy [194,227] the shapes of the measured yields in Figs. 4.11 and 4.12 are similar. In contrast the shape of the calculated yield at 10.6 GeV differs significantly from the one at 800 GeV which may suggest that the transition to energy-independent slow particle production is predicted to be at too high energies (20–30 GeV, c.f. Sec. 4.4.1). However, the description of all aspects of fragmentation (in particular also of multifragmentation) would be needed in order to draw definite conclusions.

Finally, in Fig. 4.13 average recoil momenta of residual nuclei  $\langle p_{\text{res}} \rangle$  are shown as a function of the mass difference to the target nucleus  $\Delta A = 197 - A_{\text{res}}$  together with data from proton–gold interactions at 800 GeV [224]. The behavior is qualitatively well described using the models.

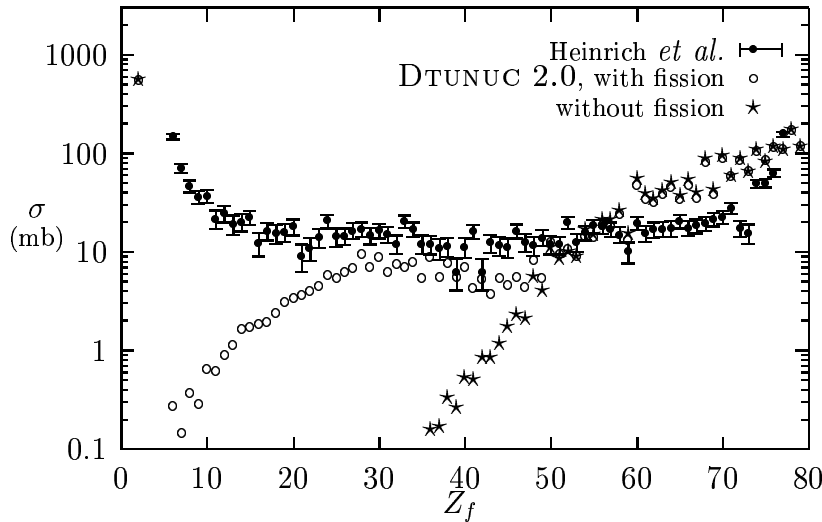


Figure 4.12: Cross sections for the production of fragments with charge  $Z_f$  in proton–gold interactions at 10.6 GeV. The influence of fission processes on the model predictions is indicated. The experimental data are from [225,226].

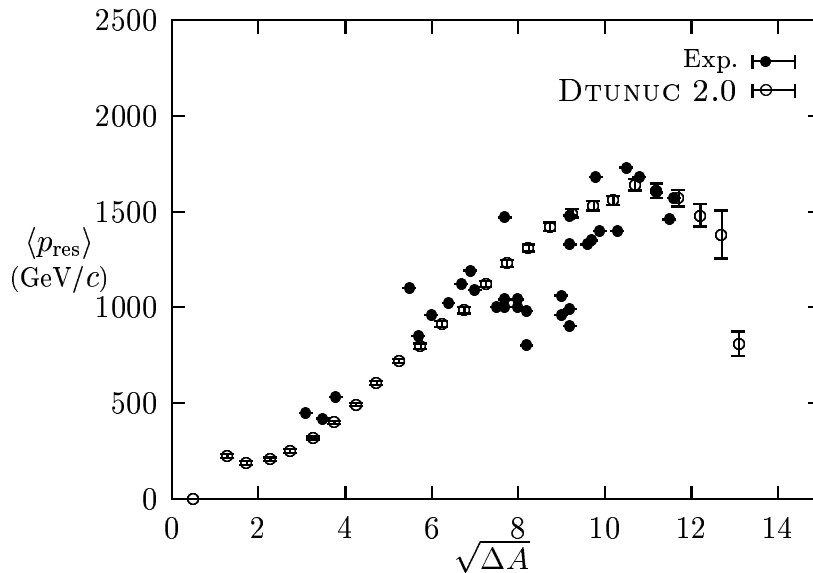


Figure 4.13: Dependence of the average total momentum of residual nuclei from  $p$ –Au interactions at 800 GeV on the number of nucleons  $\Delta A$  removed from the target in the collision. The experimental data are taken from a compilation given in [224].

#### 4.4.2 Nucleus–Nucleus Interactions

As initially mentioned the models for slow particle production discussed in this chapter are expected to work reliably only in peripheral collisions. In such a collision the spectators of the interacting nuclei can be considered as deformed, highly excited nuclei which subsequently lose their excitation energies by the above described mechanisms. In contrast in a central nucleus–nucleus collision between a light and a heavy nucleus there is probably no spectator from the former. Furthermore it is likely that the spectator of the heavy nucleus decays first into smaller droplets before the nuclear evaporation and the de-excitation start. Hence the treatments of nuclear evaporation and the formation of a stable residual nucleus become incorrect in central collisions. In spite of these problems the models are applied in minimum bias situations to all interactions, since the fraction of central collisions where they might fail is rather small.

Target associated particle production in high-energy nucleus–nucleus interactions has been experimentally investigated only by a few collaborations. Again the most detailed results were obtained with emulsion targets. In Table 4.3 average multiplicities of grey

	$E_{\text{Lab}}$ (GeV/nucleon)	$\langle N_g \rangle$		$\langle N_b \rangle$	
		DTUNUC	Exp.	DTUNUC	Exp.
O-Emul.	14.6	6.1	$5.2 \pm 0.2$	4.7	$4.8 \pm 0.2$
	60	4.3	$5.7 \pm 0.4$	4.4	$4.5 \pm 0.2$
	200	4.2	$4.3 \pm 0.3$	4.3	$4.1 \pm 0.2$
Si-Emul.	14.6	7.4	$5.4 \pm 0.3$	4.6	$4.6 \pm 0.2$
S-Emul.	200	4.4	$4.7 \pm 0.3$	4.2	$3.9 \pm 0.2$
Au-Emul.	11.6	9.7	$5.8 \pm 0.19$ [228]	3.6	$3.52 \pm 0.12$ [228]

Table 4.3: Average multiplicities of grey  $\langle N_g \rangle$  and black  $\langle N_b \rangle$  particles in interactions of nuclei with emulsions. If not explicitly indicated in the table the experimental values are taken from [229].

and black particles in interactions with oxygen, silicon, sulfur and gold projectiles at different beam energies are given. The values calculated with DTUNUC 2.0 are compared to data of the EMU01-Collab. [228,229]. According to the experiment the following definitions are applied: grey particles are protons, pions and kaons with kinetic energies between 26 and 375 MeV, 12 and 56 MeV, and 20 and 198 MeV, resp. Black particles are charged hadrons and fragments with lower energies. In the model results slow protons for example contribute about 79% and slow charged pions about 19% to the calculated grey particle multiplicity in sulfur-emulsion interactions at 200 GeV/nucleon. Whereas the grey particle multiplicities at 200 GeV/nucleon and the black particle multiplicities at all energies are well understood discrepancies exist between calculated and measured  $\langle N_g \rangle$ -values at low energies. Concerning the result for gold-emulsion collisions it should be again stressed that the models cannot be expected to work reliably for slow particle production in asymmetric collisions in the rest system of the smaller nucleus. This might explain the disagreement between the calculated grey particle multiplicity and the data.

In Fig. 4.14 multiplicity distributions of grey and black particles are shown for sulfur-emulsion interactions at 200 GeV/nucleon together with data [230–232]. At low multiplicities ( $N_{g/b} \lesssim 5$ ) the distributions are dominated by interactions with the light emulsion component whereas the tail at larger values arises from sulfur-bromine and -silver collisions. Again, within the calculations the definitions given above for “grey” and “black” of the EMU01-Collab. are applied. They also possibly explain the differences between the two data sets: the KLM-Collab. has distinguished grey and black particles by applying the cut  $\beta = 0.25$  to all heavy particles [232]. The models are able to reproduce the EMU01-results within their statistical uncertainties.

In Fig. 4.15 calculated slow particle multiplicity distributions for collisions of oxygen with different target nuclei at 200 GeV/nucleon are presented for protons and singly charged fragments only. In order to compare the model results to data obtained by the WA80-Collab. [233] the following kinematic cuts have been applied to the calculated final states: (i) an event is considered if the energy within a cone around the beam axis of  $0.3^\circ$  is less than 88% of the energy of the incident nucleus and (ii) only protons and singly

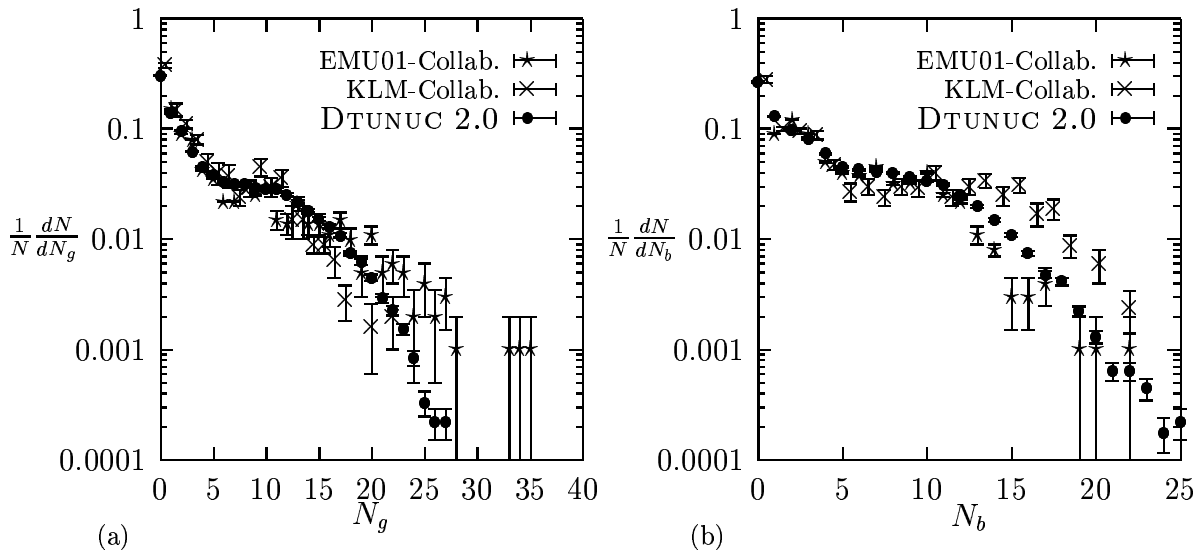


Figure 4.14: Calculated grey (a) and black (b) particle multiplicity distributions for sulfur-emulsion interactions at  $E_{Lab} = 200$  GeV/nucleon are compared to data of the EMU01- [230,231] and KLM-Collaborations [232].

charged fragments emitted with angles between  $60^\circ$  and  $160^\circ$  with respect to the collision axis and kinetic energies between 30 MeV/nucleon and 400 MeV/nucleon are taken into

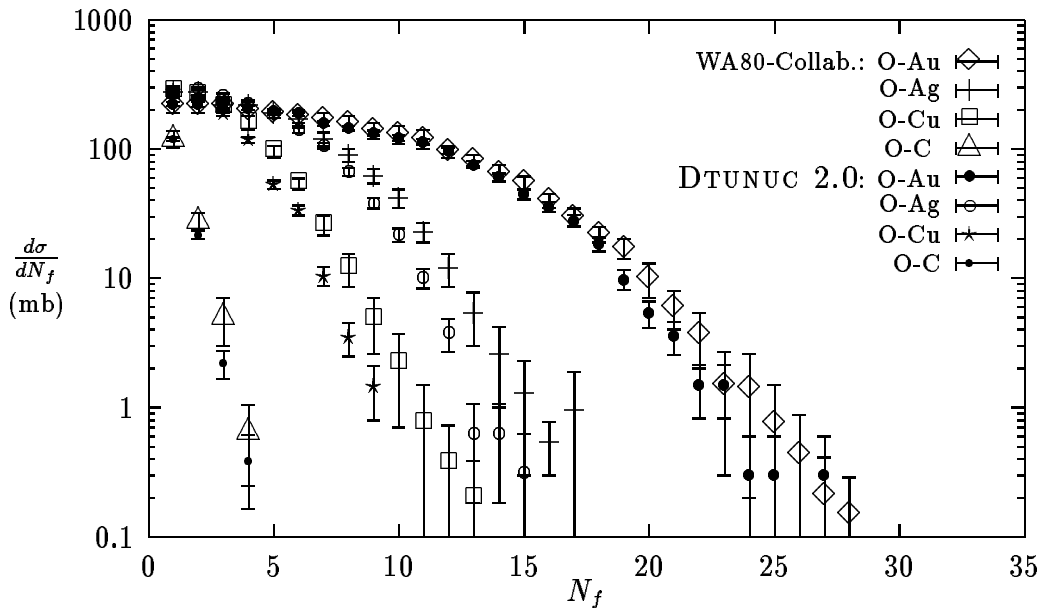


Figure 4.15: Multiplicity distributions of slow protons and singly charged fragments from oxygen-nucleus interactions at 200 GeV/nucleon. Model results are compared to data of the WA80-Collab. [233].

consideration. In addition it should be mentioned that the data are subject to detector acceptance effects [233–235] which are not taken into consideration in the calculations. The calculated distributions are therefore normalized to the data at  $N_f = 1$ .

Correlations between heavy and shower as well as between grey and black particle multiplicities are shown in Figs. 4.16 and 4.17. Taking the statistical uncertainties of the experiment into account the overall agreement with the data [230] is reasonable.

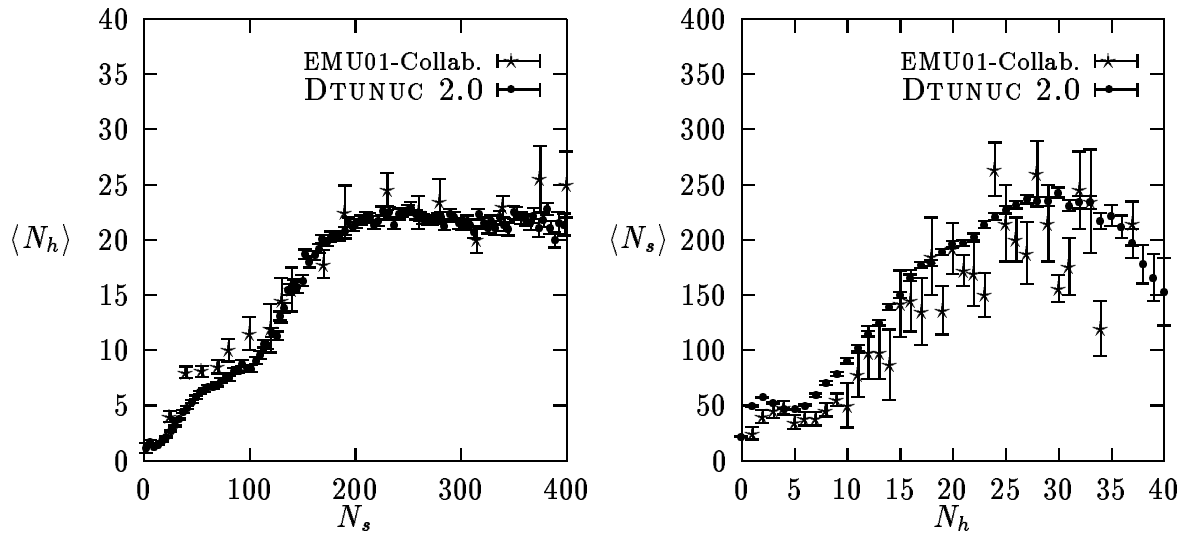


Figure 4.16: Model predictions on correlations between shower ( $N_s$ ) and heavy ( $N_h$ ) particle multiplicities in sulfur-emulsion interactions at  $E_{Lab} = 200$  GeV/nucleon are compared to experimental results [230].

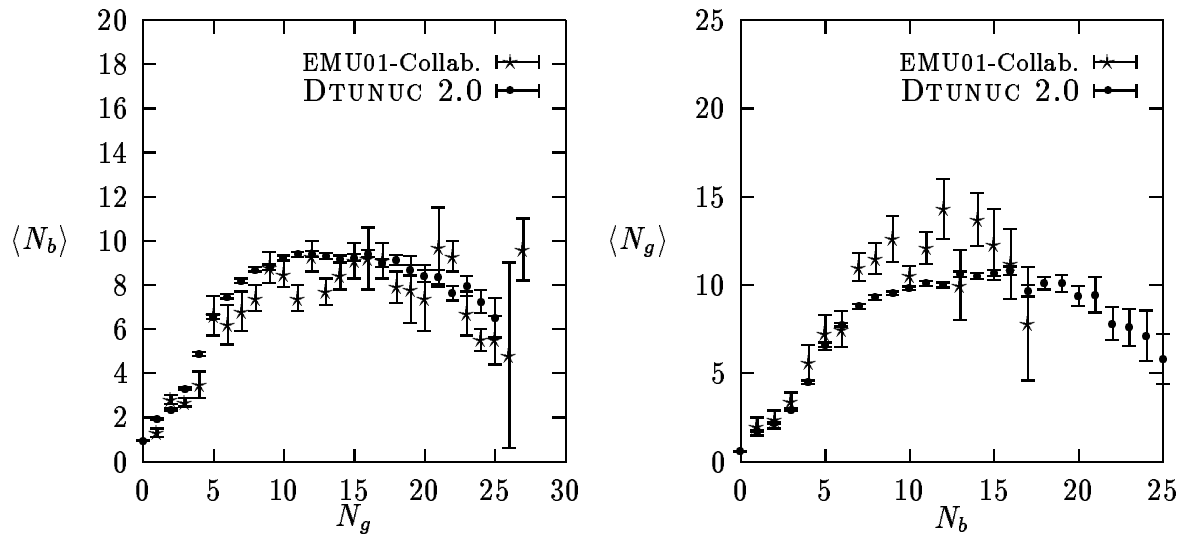


Figure 4.17: As in Fig. 4.16, here for grey ( $N_g$ ) and black ( $N_b$ ) particle multiplicities.

In order to study the kinematics in slow particle production angular distributions of grey and black particles are calculated and compared to data on sulfur-emulsion interactions at 200 GeV/nucleon [229,232] in Fig. 4.18. In the forward direction protons dominate the yield of grey particles. Pions produced in intranuclear cascade processes become additionally important in the backward direction. Parametrizing the angular distribution of grey particles by  $K \exp(b \cos \Theta_g)$  the values  $K = 0.39$  and  $b = 1.25$  are

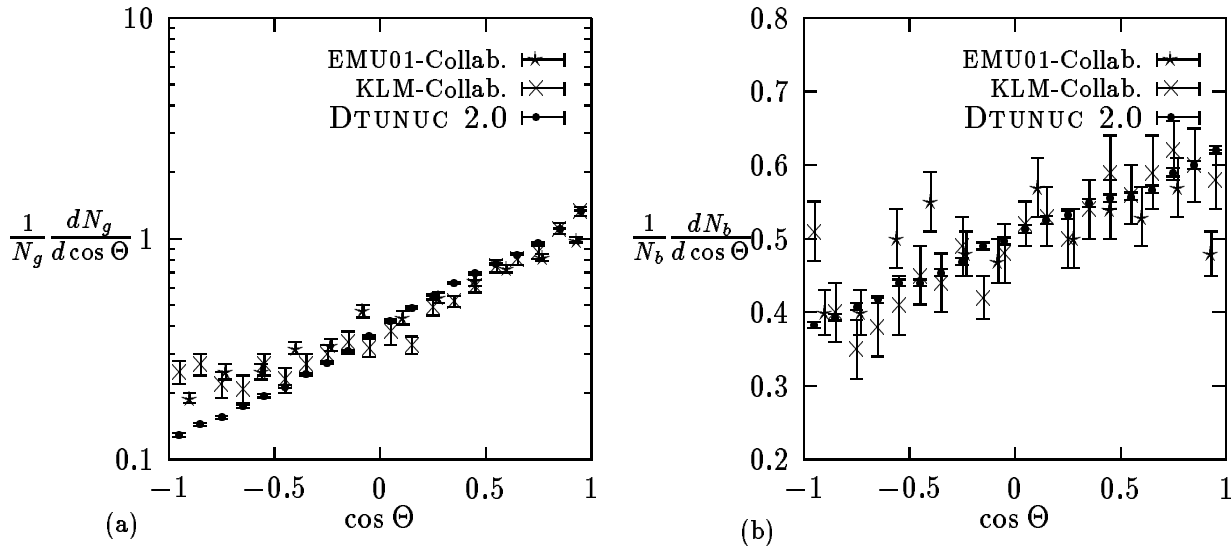


Figure 4.18: Angular distributions of grey (a) and black (b) particles in sulfur–emulsion interactions at 200 GeV/nucleon. Model results are shown together with data [229,232].

obtained for the calculated distribution. They have to be compared to the experimental values of  $K = 0.44$  and  $b = 0.92$ . The good agreement with data on the angular distributions of black particles (Fig. 4.18b) supports the conclusion that the recoil momentum transferred to the residual nucleus is well described within the models.

Finally, cross sections for the production of target fragments in carbon–silver interactions at 25.2 GeV/nucleon are given in Fig. 4.19. In most of the spallation and deep spallation regions (see Sec. 4.4.1) the measured cross sections [236] are reproduced. For  $A_f > 100$  the models underestimate the data by about a factor of two due to reasons already discussed. The calculated yields at  $A_f = 2,3,4$  represent nuclei evaporated from the prefragments.

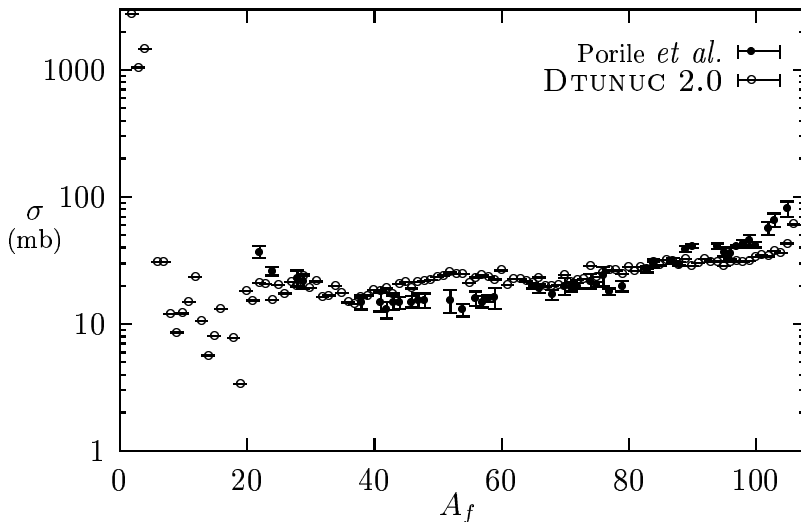


Figure 4.19: Cross sections for the production of target fragments in carbon–silver interactions at 25.2 GeV/nucleon. Model results are compared to data [236].

## 4.5 Applications to Cosmic Ray Cascades in the Atmosphere

As already outlined projectile associated particle production contributes to the very forward direction of a cosmic ray cascade. Moreover, it may even dominate the particle spectra in kinematic regions which are either not accessible by secondaries of hadron–nucleus interactions (such as the production of high-energy fragments) or which are populated with only small probabilities (such as the high-energy meson yield at projectile pseudorapidities).

In this section two examples are discussed: the production of pions in intranuclear cascade processes in the projectile spectator nucleus [58] and the production and  $\gamma$  de-excitation of residual projectile nuclei [57]. The former for instance may affect the high-energy muon component in the cascade and the de-excitation photons contribute to the electromagnetic shower.

The results presented here were obtained using the DPMJET-II and DTUNUC 2.0 event generators. It can be shown [58] that these results do not depend on the particular realization of the two-component DPM.

### 4.5.1 Projectile Associated Meson Production

The main effect of intranuclear cascades is that nucleons are knocked out of the spectator nucleus. However, as mentioned in Sec. 4.4.2 up to 20% (depending on the colliding nuclei and on the collision energy) of the grey particles are predicted by the model to be pions which are produced in inelastic reinteractions within the spectator nucleus. Direct verification of the predictions of the models concerning these pions is as yet not possible. The emulsion experiments do not allow particle identification and give only information on all slow charged particles and fragments. On the other hand the WA80-Collab. has published results on slow protons and singly charged fragments only. As demonstrated in Sections 4.4.1 and 4.4.2 the models are in reasonable agreement with results from both classes of experiments giving an indirect support for the ability to describe also pion production in intranuclear cascade processes.

#### Feynman- $x$ distributions

Feynman- $x$  distributions are most suitable in order to study particle production in the projectile and target fragmentation regions. Here the observable  $x_F$  is defined as  $x_F = p_{\parallel}/|p_{\parallel}^{\max}|$ , where  $p_{\parallel}$  and  $p_{\parallel}^{\max}$  are the longitudinal momentum of a hadron or fragment and the maximum longitudinal momentum of a hadron (disregarding Fermi-momenta) in the nucleon–nucleon c.m. system, resp. Whereas experimental data on the proton fragmentation region of proton–proton and proton–nucleus collisions is available (and has been compared to results of DPMJET-II in [31]), to the best of our knowledge no corresponding experimental information exists on the fragmentation region of the nucleus.

In Fig. 4.20 Feynman- $x$  distributions of positively charged pions are shown for helium–, oxygen–, and iron–air interactions at a laboratory energy of 500 TeV/nucleon. In order to point out the contribution from intranuclear cascade processes for each configuration two distributions are plotted: one obtained taking the formation zone cascade into account

and a second one calculated without this cascade. As the comparison clearly demonstrates

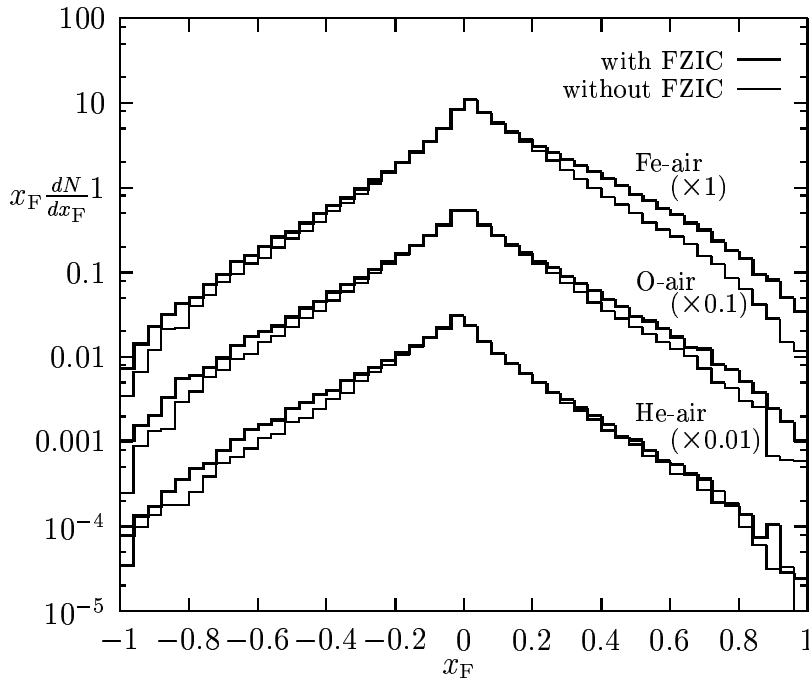


Figure 4.20: Feynman- $x$  distributions of  $\pi^+$ -mesons are shown for helium-, oxygen- and iron-air interactions at  $E_{\text{Lab}} = 500$  TeV/nucleon. Predictions are given for the model with and without formation zone intranuclear cascade (FZIC).

the intranuclear cascade significantly enhances the pion multiplicity in the two regions with  $|x_{\text{F}}| > 0.3$ . This effect is more pronounced the heavier the nucleus is and can be neglected for helium.

### Spectrum-weighted moments and energy fractions

To study properties of cosmic ray cascades it is often convenient to examine spectrum-weighted moments  $Z_i$  of inclusive cross sections for the production of particles of type  $i$  in collisions of hadrons and nuclei with air nuclei [1]. They are defined as

$$Z_i = \int_0^A dx_{\text{Lab}} (x_{\text{Lab}})^{\gamma-1} F_i(x_{\text{Lab}}) \quad \text{with} \quad F_i(x_{\text{Lab}}) = x_{\text{Lab}} \frac{dN_i}{dx_{\text{Lab}}}, \quad x_{\text{Lab}} = \frac{E_{\text{Lab}}}{E_0}. \quad (4.26)$$

$x_{\text{Lab}}$  denotes the fraction of the (laboratory) energy per nucleon  $E_0$  of the projectile carried by a secondary particle. Here  $-(\gamma+1) = -2.7$  is approximately equal to the power of the differential high-energy cosmic ray spectrum. The integration over  $x_{\text{Lab}}$  is performed up to the projectile mass number  $A$  because projectile fragments, but also secondary hadrons (due to the Fermi-momenta of nucleons), may have  $x_{\text{Lab}} > 1$ .

In proton-induced air showers ( $A = 1$ ) spectrum-weighted moments determine the uncorrelated fluxes of energetic particles in the atmosphere. Since with  $\gamma = 1.7$  the contribution to the moments from  $x_{\text{Lab}} \rightarrow 0$  vanishes the uncorrelated fluxes only depend on the behavior of the inclusive cross sections in the forward fragmentation region. The spectrum-weighted moments are about the same for all generations of the cascade and show a weak energy dependence [1].

In a cosmic ray cascade initiated by a primary nucleus the situation is different. Such a cascade contains after the first interaction mostly nucleons and hadrons. The spectrum-weighted moments can describe the average particle content in the cascade precisely only

after this interaction [58]. Nevertheless they might be used to outline differences between models. In particular, within this study they are calculated in order to prove that the superposition model<sup>3</sup> is only a rough approximation when compared to a complete treatment of nucleus–nucleus collisions within the description of the cascade.

In Table 4.4 spectrum-weighted moments of charged pions are given for different projectiles interacting with air nuclei at 500 and  $5 \cdot 10^6$  TeV/nucleon. Results of calculations

	$E_{\text{Lab}}$ (ATeV)	$\nu_p$	(1) $Z_\pi$	(2) $Z_\pi$	(3) $\nu_p Z_\pi^{\text{p-air}}$	(1) $K_\pi$	(2) $K_\pi$	(3) $\nu_p K_\pi^{\text{p-air}}$
p-air	500	1.0	-	0.0640	0.0640	-	0.350	0.350
	$5 \cdot 10^6$	1.0	-	0.0586	0.0586	-	0.370	0.370
He-air	500	2.32	0.178	0.182	0.148	0.89	0.90	0.81
	$5 \cdot 10^6$	2.60	0.180	0.175	0.152	1.01	0.99	0.96
O-air	500	5.55	0.425	0.499	0.355	2.02	2.22	1.94
	$5 \cdot 10^6$	6.22	0.462	0.522	0.364	2.43	2.56	2.30
Fe-air	500	11.9	0.912	1.27	0.762	4.05	4.81	4.17
	$5 \cdot 10^6$	13.9	1.02	1.29	0.815	4.70	5.43	5.14

Table 4.4: *Spectrum-weighted moments  $Z_\pi$  and energy fractions  $K_\pi$  of charged pions are given for the model without formation zone cascade (1), with this cascade (2) and for a model based on  $\nu_p$  independently interacting protons with air (nitrogen) nuclei (3).  $\nu_p$  is the number of projectile nucleons interacting with target nucleons.*

disregarding intranuclear cascade processes (labelled with “(1)”) and taking them into account (labelled with “(2)”) are presented. In addition the number of projectile nucleons  $\nu_p$  sampled according to the Gribov–Glauber formalism and moments corresponding to an approximation in which the nucleus–air interaction is replaced by  $\nu_p$  independent proton–air interactions (resembling the treatment of nucleus–nucleus collisions within the superposition model; labelled with “(3)”) are listed. A comparison of the three  $Z$ -values for each configuration and energy can be summarized as follows:

- The  $Z$ -values of the model without formation zone cascade (1) already differ by about 10–20% from the values given in column (3).
- Taking the formation zone cascade into account these differences become as large as 50–70% with regard to (3).
- The differences depend strongly on the mass of the projectile nucleus and are most pronounced (among the studied collisions) for Fe–air interactions.

<sup>3</sup>In the superposition model the particle cascade in the atmosphere induced by a high-energy nucleus of mass  $A$  and energy  $E$  is approximated by a superposition of  $A$  independent showers initiated by nucleons each of an energy of  $E/A$

Likewise, energy fractions  $K_i = Z_i(\gamma = 1)$  might be compared. Results are given in Table 4.4, again for the three different cases. The conclusions are essentially the same as for the  $Z$ -values, though differences between (2) and (3) are less prominent (5–10%). For Fe–air a comparison in the iron rest frame would be more appropriate [58].

## 4.5.2 Residual Nuclei and De-excitation Photons from the Projectile Spectator

So far one possible impact of a treatment of primary nuclei on the description of cosmic ray cascades has been discussed with respect to intranuclear cascade processes in the projectile spectator nucleus. In this section the disintegration and de-excitation of the projectile prefragment is considered in addition.

### Projectile fragments

As examples Table 4.5 shows average multiplicities of protons and neutrons evaporated from projectile prefragments in oxygen– and iron–air collisions for different laboratory momenta per projectile nucleon. In addition average numbers of heavy fragments are

$p_{\text{Lab}}$ (A TeV/c)	O–air				Fe–air			
	$\langle N_p \rangle$	$\langle N_n \rangle$	$\langle N_\gamma \rangle$	$\langle N_{hf} \rangle$	$\langle N_p \rangle$	$\langle N_n \rangle$	$\langle N_\gamma \rangle$	$\langle N_{hf} \rangle$
0.2	0.74	0.80	0.20	1.8	2.5	4.0	1.9	2.5
20	0.85	0.90	0.17	1.7	2.8	4.5	1.7	2.9
2000	0.91	0.95	0.14	1.7	3.2	4.9	1.4	3.2
200000	0.91	0.98	0.12	1.6	3.5	5.2	1.2	3.4

Table 4.5: Average multiplicities of protons  $\langle N_p \rangle$ , neutrons  $\langle N_n \rangle$ , and heavy fragments  $\langle N_{hf} \rangle$  evaporated from the projectile prefragment and of projectile de-excitation photons  $\langle N_\gamma \rangle$  in oxygen– and iron–air interactions are given.

shown. They include evaporated light fragments (deuterium,  $^3\text{H}$ ,  $^3\text{He}$  and  $\alpha$ ), residual nuclei and, in case of oxygen-projectiles, also heavier fragments produced according to the Fermi Break-up model.

Predictions of cross sections for projectile fragment production are shown in Fig. 4.21, again, for oxygen–(a) and iron–air interactions (b). Errorbars indicate statistical uncertainties of the calculations. Substructures apparent in the mass yields (especially for oxygen–air) are caused by specific properties of the fragmentation (Fermi Break-up) process. Even though the overall shape of the mass yields remains constant over several orders of magnitude of the projectile laboratory energy cross sections of small fragments ( $A_f \lesssim 6$ ) are slightly increasing with energy whereas those of fragments with higher masses decrease. It should be stressed again that for fragments with  $A_f > 16$  apart from evaporation no further fragmentation is treated. According to the discussion in Sec. 4.4.1 cross sections for fragments close to iron (Fig. 4.21b) are expected to be underestimated.

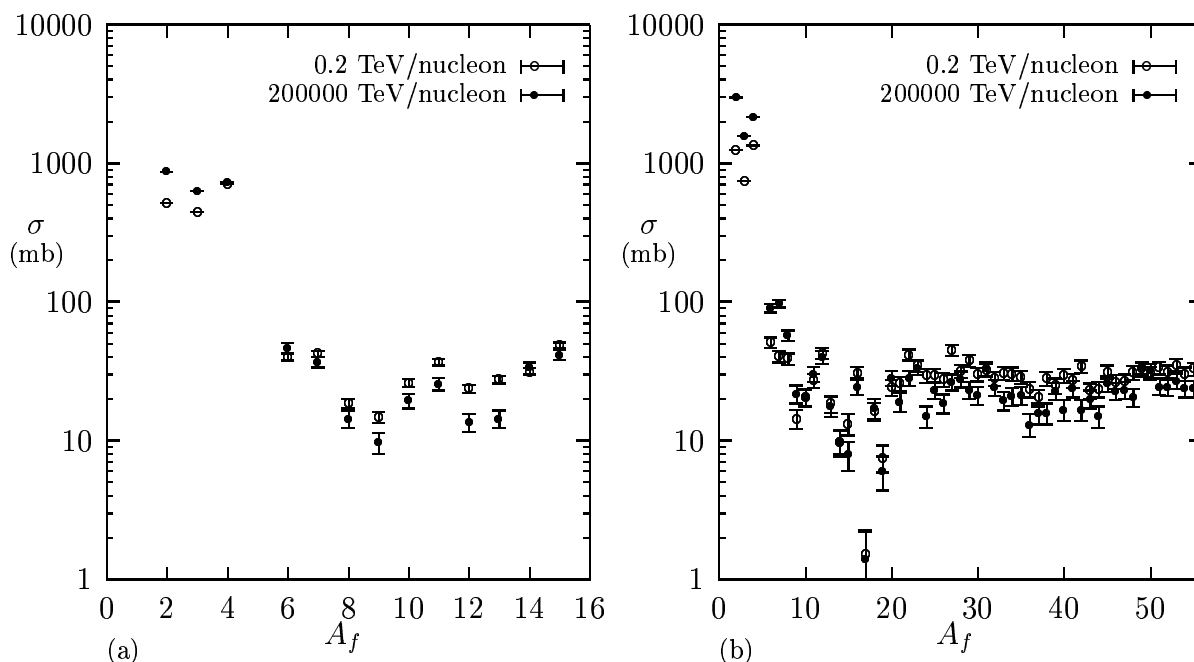


Figure 4.21: Cross sections for the production of projectile fragments in oxygen- (a) and iron-air interactions (b) at 0.2 and 200000 TeV/nucleon in the laboratory frame.

### De-excitation photons

Within the event generators there are two main mechanisms of photon production in nucleus-nucleus collisions: (i) decays of hadrons (predominantly  $\pi^0$  mesons) and (ii) nu-

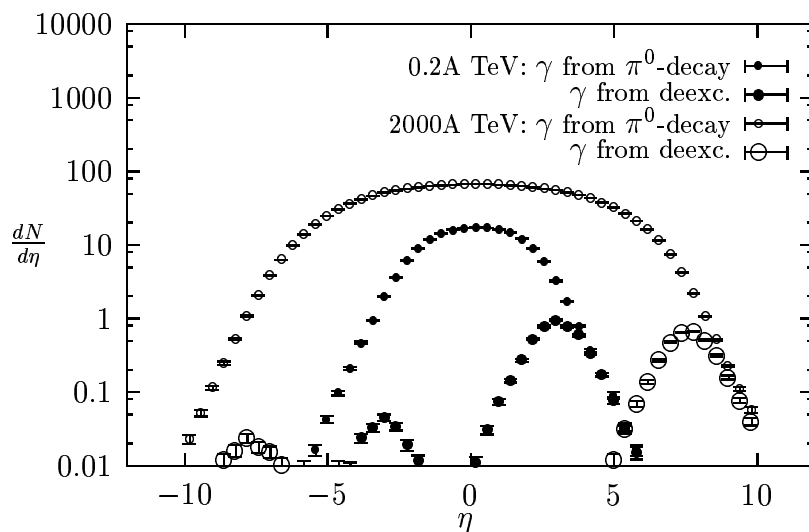


Figure 4.22: Pseudorapidity distributions of photons produced in iron-air interactions at laboratory energies of 0.2 and 2000 TeV/nucleon. Contributions of photons resulting from  $\pi^0$ -decays and from de-excitation processes of the residual nuclei are given separately. The distributions are plotted in the nucleon-nucleon c.m. frame.

clear de-excitation processes of prefragments. In order to study their relative contribution to the total photon spectrum and the kinematic regions which are affected by both mechanisms their pseudorapidity distributions are shown separately in Fig. 4.22 for iron-air collisions at 0.2 and 2000 TeV/nucleon. It is obvious that photon production by nuclear de-excitation contributes only a minor fraction to the total multiplicity in the forward and backward directions. Integrating the de-excitation photon distribution at a certain energy

over, for instance, the forward hemisphere ( $\eta > 0$ ) the average number of de-excitation photons per interaction from the projectile prefragment is obtained. It represents the residual excitation energy of this prefragment after the evaporation step. As it can be seen from the figure this average excitation energy is about constant with collision energy above 200 GeV/nucleon.

Finally in Fig. 4.23 Feynman- $x$  distributions of photons are shown in the nucleon-nucleon c.m. system, again for both sources of photons separately. It can be concluded that the contribution of de-excitation photons is small and can be neglected for most applications (mainly soft photons).

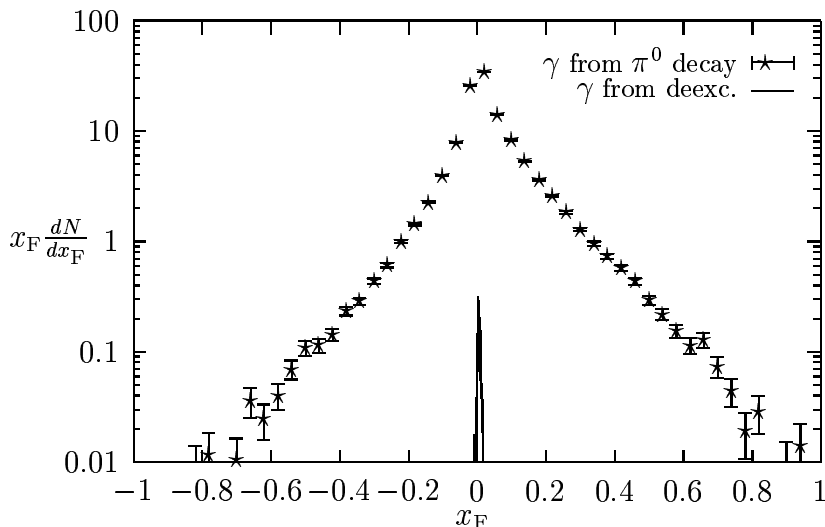


Figure 4.23: Feynman- $x$  distributions of photons produced in iron-air interactions at 200000 TeV/nucleon are shown. The contributions of photons from decays (stars) and from de-excitation processes of the projectile prefragments (line) are plotted.

## Chapter 5

# Summary and Conclusions

In the course of this work three aspects of high-energy nuclear collisions have been studied: photoproduction off nuclei, single diffractive hadron–nucleus collisions and hard diffraction, and projectile and target associated particle production.

The two-component Dual Parton Model has been applied to interactions of real and weakly virtual photons with nuclei for the first time. The description of these processes is based on the following ideas.

The photon is assumed to interact either directly (direct processes) or as a quark–antiquark fluctuation with nucleons of the target nucleus (resolved processes). The multiple scattering process of the  $q\bar{q}$ -state inside the nucleus is described in the framework of the Gribov–Glauber approximation in terms of multiple soft and hard pomeron exchange. An essential assumption imposed on this formalism concerns interactions of high-mass fluctuations, the so-called anomalous photon interactions and direct photon interactions. It is assumed that in anomalous and direct processes the photon interacts as a point-like particle with only one target nucleon. The Gribov–Glauber cascade is suppressed at high energies due to point-like processes and at very low energies due to the limited coherence length of the hadronic fluctuation.

Within this description total cross sections are predicted up to TeV-energies:

- Comparisons of calculated cross sections and nuclear shadowing behavior with data on photoproduction as well as on virtual photon–nucleus interactions show a reasonable agreement.
- The presence of point-like photon interactions becomes visible in the total cross sections and the shadowing behavior of real photon–nucleus collisions at high energies. These interactions lead to a stronger increase of the cross sections with energy and may result in decreasing nuclear shadowing at TeV-energies. This effect is most strongly pronounced for heavy target nuclei.

Using the PHOJET-model for photon–nucleon collisions, a MC formulation of the two-component DPM for photoproduction off nuclei has been developed and implemented into the event generator DTUNUC. The extension from photon–hadron and hadron–nucleus collisions to multiparticle photoproduction off nuclei contains no further free parameters and is therefore a severe test of the approach. The following results on multiparticle production are obtained within this model:

- The good agreement of calculated multiparticle production with data on photon–hadron, hadron–nucleus, and nucleus–nucleus collisions demonstrates the consistency of the model. Similar to the behavior of cross sections also particle production off nuclei clearly shows decreasing shadowing with increasing photon virtuality. At energies of present fixed target experiments inclusive particle cross sections are approximately proportional to  $A^1$  already at  $Q^2 > 1 \text{ GeV}^2$ . This is caused by the decrease of the  $q\bar{q}$ –nucleon cross sections with increasing  $Q^2$ .
- In analogy to observations in photon–proton collisions at HERA, the model predicts that also in photoproduction off nuclei the dual nature of the photon may show up most clearly in hadronic jet production. Jet profiles in photon–nucleus collisions reveal a strong dependence of the underlying event on the fraction of the photon momentum contributing to the jets.

Furthermore diffractive interactions have been studied. In the model, incoherent single diffractive hadron–nucleus collisions are approximated by diffractive interactions of projectile hadrons with single target nucleons. Cross sections are calculated taking fluctuations in total hadron–nucleon cross sections into consideration. High-mass diffractive particle production is described by a cut triple-pomeron graph resulting in two chains of particles. The model for single diffractive hadron–nucleus collisions has been implemented into the event generator DTUNUC.

From a study of nucleus diffraction dissociation in proton–beryllium, –aluminum, and –tungsten interactions the following conclusions can be drawn:

- The dependence of the calculated cross sections on the target mass number shows the peripheral character of the process and is in agreement with cross section data of the HELIOS-Collaboration. Model predictions on single diffractive proton–nucleus cross sections overestimate the data which deserves further theoretical investigations, especially as soon as more detailed experimental information is available.
- Many features of particle production within the model, such as the  $M_D$ - and  $t$ -dependence of inclusive cross sections, are in reasonable agreement with first experimental observations.

The description of hard diffractive particle production in hadron–hadron and photon–hadron interactions is based on the assumption that the pomeron can be considered as a partonic object. Consequently, jets in single diffractive final states originate from hard processes between partons of a pomeron and partons of one of the scattering hadrons. PDFs of the pomeron have been developed which are motivated by Regge theory. Using these PDFs together with lowest order perturbative QCD for the hard partonic subprocess hard diffractive particle production in hadron–hadron and photon–hadron collisions is calculated.

Data on diffractive photoproduction from HERA are qualitatively well described within the model if a hard component is included into the description of diffraction. Furthermore, model predictions on hard diffractive particle production in proton–antiproton collisions show features which are similar to those of first, uncorrected data of the UA8-Collaboration.

The description of projectile and target associated particle production discussed in this work is based on models for the following interaction mechanisms: intranuclear cascades, evaporation of nucleons and light fragments, nuclear fragmentation processes and de-excitation of fragments by photon emission.

Here, the formation zone intranuclear cascade model has been extended from hadron–nucleus to nucleus–nucleus collisions. For both channels a method to calculate excitation energies of prefragments in peripheral collisions is proposed. These excitation energies serve as input for a description of further prefragment disintegration. This disintegration is treated by applying models for evaporation of nucleons and fragments with masses up to helium, for high-energy fission and by employing the Fermi Break-up model for the fragmentation of light prefragments. A small part of the excitation energy might also be spent in photon emission processes which are taken into account using an appropriate formulation.

All these aspects have been implemented into the DPMJET-II and DTUNUC realizations of the two-component DPM and the obtained results can be summarized as follows:

- The calculations on target associated particle production are in reasonable agreement with a large amount of experimental data from hadron–nucleus and nucleus–nucleus collisions.
- Calculated cross sections for the production of residual nuclei in the spallation and deep spallation regions agree with data within a factor of two, as expected, since multifragmentation is not treated.

A first application to interactions of cosmic ray nuclei in the atmosphere shows that a description of projectile associated particle production could lead to relevant quantitative effects in the simulation of cosmic ray cascades. Model predictions on both, spectrum weighted moments and energy fractions of mesons increase if these processes are taken into account. In a cosmic ray cascade calculation this would cause smaller depths of the shower maximum and therefore a smaller electromagnetic size of the shower at mountain or sea level. Furthermore projectile associated mesons might affect the muon content in a shower. Cross sections for the production of projectile fragments in oxygen– and iron–air collisions are predicted. The shape of the mass yields is approximately energy-independent in the TeV-energy region. In high-energy nucleus–air interactions photons from the de-excitation of projectile prefragments are predicted to play a minor role as compared to photons produced by particle decays.



# Bibliography

- [1] T. K. Gaisser: *Cosmic Rays and Particle Physics*, Cambridge University Press, Cambridge 1990
- [2] J. H. Adams, Jr.: *Cosmic Ray Effects on Microelectronics*, Part IV, NRL Memorandum Report 5901, 1986
- [3] M. A. Shea, D. F. Smart and J. R. McCall: *Can. J. Phys.* 46 (1988) S1098
- [4] W. Heinrich and A. Spill: *J. Geophys. Res.* 84 (1979) 4401
- [5] S. Yoshida et al.: *Astropart. Phys.* 3 (1995) 105
- [6] M. Ichimura et al.: *Phys. Rev.* D48 (1993) 1949
- [7] O. C. Allkofer and P. K. F. Grieder: *Physics Data: Cosmic Rays on Earth* Fachinformationszentrum Energie - Physik - Mathematik GmbH, Karlsruhe 1984
- [8] H. G. Paretzke and W. Heinrich: *Radiation Protection Dosimetry* 48 (1993) 33
- [9] S. Roesler, W. Heinrich and H. Schraube: *Calculation of radiation fields in the atmosphere and comparison to experimental data*, preprint SI 96-11, 1996
- [10] T. W. Armstrong, K. C. Chandler and J. Barish: *J. Geophys. Res.* 78 (1973) 2715
- [11] M. Merker: *Health Physics* 25 (1973) 524
- [12] C. Forti et al.: *Phys. Rev.* D42 (1990) 3668
- [13] G. Battistoni: Monte Carlo simulations in high-energy cosmic ray physics, in *Proceedings of the IVth International Conference on Calorimetry in High Energy Physics*, La Biodola (Elba), Italy, 1993, ed. by A. Menzione and A. Scribano, World Scientific, Singapore, p. 503, 1993
- [14] R. S. Fletcher, T. K. Gaisser, P. Lipari and T. Stanev: *Phys. Rev.* D50 (1994) 5710
- [15] G. Battistoni, C. Forti and J. Ranft: *Astropart. Phys.* 3 (1995) 157
- [16] P. Lipari and T. Stanev: *Phys. Rev.* D44 (1991) 3543
- [17] J. Bellandi, R. J. M. Covolan, A. L. Godoi and J. Montanha: *J. Phys. G* 23 (1997) 125
- [18] H. H. Mielke, M. Föller, J. Engler and J. Knapp: *J. Phys. G* 20 (1994) 637
- [19] J. Ranft and W. R. Nelson: *Nucl. Inst. and Meth.* A257 (1987) 177
- [20] M. Erdmann: *The Partonic Structure of the Photon: Photoproduction at the Lepton-Proton Collider HERA*, preprint DESY 96-090, 1996
- [21] M. Drees and R. M. Godbole: *Resolved photon processes*, report MADPH-95-898, BU-TH-95/2, (hep-ph/9508221), 1995
- [22] M. Arneodo: *Phys. Rep.* 240 (1994) 301
- [23] G. Piller, W. Ratzka and W. Weise: *Z. Phys.* A352 (1995) 427
- [24] A. Capella, U. Sukhatme, C. I. Tan and J. Trân Thanh Vân: *Phys. Rep.* 236 (1994) 225
- [25] A. Capella, J. Trân Thanh Vân and J. Kwieciński: *Phys. Rev. Lett.* 58 (1987) 2015
- [26] K. Hahn and J. Ranft: *Phys. Rev.* D41 (1990) 1463

- [27] F. W. Bopp, A. Capella, J. Ranft and J. Trần Thanh Vân: Z. Phys. C51 (1991) 99
- [28] P. Aurenche, F. W. Bopp, A. Capella, J. Kwieciński, M. Maire, J. Ranft and J. Trần Thanh Vân: Phys. Rev. D45 (1992) 92
- [29] F. W. Bopp, D. Pertermann and J. Ranft: Z. Phys. C54 (1992) 683
- [30] F. W. Bopp, R. Engel, D. Pertermann and J. Ranft: Phys. Rev. D49 (1994) 3236
- [31] J. Ranft: Phys. Rev. D51 (1995) 64
- [32] R. Engel: Z. Phys. C66 (1995) 203
- [33] R. Engel and J. Ranft: Phys. Rev. D54 (1996) 4244
- [34] R. Engel: *Hadronic interactions of photons at high energies*, PhD thesis Universität Siegen, 1997
- [35] I. Kawrakow, H. J. Möhring and J. Ranft: Phys. Rev. D47 (1993) 3849
- [36] R. Engel, J. Ranft and S. Roesler: Photoproduction off nuclei and point-like photon interactions, Part I: Cross sections and nuclear shadowing, preprint SI 96-09, US-FT/42-96, (hep-ph/9610281), 1996
- [37] S. Roesler, R. Engel and J. Ranft: Photoproduction off nuclei and point-like photon interactions, Part II: Particle production, preprint SI 96-14, US-FT/45-96, (hep-ph/9611379), 1996
- [38] HELIOS Collab.: T. Åkesson et al.: Z. Phys. C49 (1991) 355
- [39] EHS/NA22 Collab.: N. M. Agababyan et al.: Z. Phys. C72 (1996) 65
- [40] G. Alberi and G. Goggi: Phys. Rep. 74 (1981) 1
- [41] V. V. Anisovich, V. M. Braun, Y. M. Shabelski and V. M. Shekhter: Sov. J. Nucl. Phys. 36 (1982) 428
- [42] V. R. Zoller: Z. Phys. C51 (1991) 659
- [43] N. Armesto, M. Braun and C. Pajares: Phys. Rev. D48 (1993) 162
- [44] M. A. Faessler: Z. Phys. C58 (1993) 567
- [45] L. Frankfurt, G. A. Miller and M. Strikman: Phys. Rev. Lett. 71 (1993) 2859
- [46] R. Engel, M. A. Braun, C. Pajares and J. Ranft: Diffraction dissociation, an important background to photon-photon collisions via heavy ion beams at LHC, preprint SI 96-04, US-FT/18-96, (hep-ph/9605227) Z. Phys. C, in print, 1996
- [47] S. Roesler, R. Engel and J. Ranft: Z. Phys. C59 (1993) 481
- [48] J. Ranft and S. Roesler: Z. Phys. C62 (1994) 329
- [49] R. Engel, J. Ranft and S. Roesler: Phys. Rev. D52 (1995) 1459
- [50] J. Engel, T. K. Gaisser, P. Lipari and T. Stanev: Phys. Rev. D46 (1992) 5013
- [51] J. N. Capdevielle et al.: The Karlsruhe extensive air shower simulation code CORSIKA, preprint KfK-4998, 1992
- [52] K. Werner: Phys. Rep. 232 (1993) 87
- [53] N. N. Kalmykov and S. S. Ostapchenko: Phys. At. Nucl. 56 (1993) 346
- [54] J. Ranft: Z. Phys. C43 (1989) 439
- [55] H.-J. Möhring and J. Ranft: Z. Phys. C52 (1991) 643
- [56] A. Ferrari, J. Ranft, S. Roesler and P. R. Sala: Z. Phys. C70 (1996) 413
- [57] A. Ferrari, J. Ranft, S. Roesler and P. R. Sala: Z. Phys. C71 (1996) 75
- [58] G. Battistoni, C. Forti, J. Ranft and S. Roesler: Deviations from the superposition model in a Dual Parton Model with formation zone cascade in both projectile and target nuclei, preprint US-FT/29-96, (hep-ph/9606485), to appear in Astroparticle Phys., 1996
- [59] M. Arneodo, A. Bialas, M. W. Krasny, T. Sloan and M. Strikman: Nuclear beams

- in HERA, in Proceedings of the Workshop Future Physics at HERA 1995/96, ed. by G. Ingelman, A. De Roeck and R. Klanner, p. 887, 1996
- [60] N. V. Mokhov and R. J. Noble:  $2 \times 2$  TeV  $\mu^+\mu^-$  Collider, preprint Fermilab-Conf-96/368, to appear in Proceedings of the XV Conference on Charged Particle Accelerators, Protvino, Russia, 1996
- [61] N. V. Mokhov: Radiation Issues of a  $\mu^+\mu^-$  Collider, preprint Fermilab-Conf-96/367, in Proceedings of the 1996 DPF/DPB Summer Study on New Directions for High Energy Physics (Snowmass '96), Snowmass (Colorado), U.S.A., 1996
- [62] European Muon Collab.: J. J. Aubert et al.: Phys. Lett. B123 (1983) 275
- [63] L. L. Frankfurt and M. I. Strikman: Phys. Rep. 160 (1988) 235
- [64] R. J. Glauber: Phys. Rev. 100 (1955) 242
- [65] V. N. Gribov: Sov. Phys. JETP 30 (1970) 709
- [66] L. Bertochi: Il Nuovo Cimento 11A (1972) 45
- [67] S. J. Brodsky and H. J. Lu: Phys. Rev. Lett. 64 (1990) 1342
- [68] E665-Collab.: M. R. Adams et al.: Z. Phys. C67 (1995) 403
- [69] New Muon Collab.: P. Amaudruz et al.: Nucl. Phys. B441 (1995) 3
- [70] SLAC E139-Collab.: R. G. Arnold et al.: Phys. Rev. Lett. 52 (1984) 727
- [71] T. H. Bauer, R. D. Spital and D. R. Yennie: Rev. Mod. Phys. 50 (1978) 261
- [72] A. Donnachie and G. Shaw: *Generalized Vector Dominance*, Plenum Press, New York, 1978 in: Electromagnetic Interactions of Hadrons, Volume 2, ed. by A. Donnachie and G. Shaw
- [73] B. L. Ioffe, V. A. Khoze and L. N. Lipatov: *Hard Processes, Volume 1: Phenomenology Quark-Parton Model*, North-Holland Physics Publishing, Amsterdam 1984
- [74] V. M. Budnev, I. F. Ginzburg, G. V. Meledin and V. G. Serbo: Phys. Rep. 15C (1975) 181
- [75] J. J. Sakurai and D. Schildknecht: Phys. Lett. 40B (1972) 121
- [76] G. Grammer, Jr. and D. Sullivan: *Nuclear Shadowing of Electromagnetic Processes*, Plenum Press, New York, 1978 in: Electromagnetic Interactions of Hadrons, Volume 2, ed. by A. Donnachie and G. Shaw
- [77] B. Gorczyca and D. Schildknecht: Phys. Lett. 47B (1973) 71
- [78] G. 't Hooft: Nucl. Phys. B72 (1974) 461
- [79] G. Veneziano: Nucl. Phys. B74 (1974) 365
- [80] E. Witten: Nucl. Phys. B160 (1979) 57
- [81] H.-M. Chan, J. E. Paton and S. T. Tsou: Nucl. Phys. B86 (1975) 479
- [82] G. F. Chew and C. Rosenzweig: Nucl. Phys. B104 (1976) 290
- [83] G. F. Chew and C. Rosenzweig: Phys. Rep. 41 (1978) 263
- [84] T. Regge: Il Nuovo Cimento 14 (1959) 951
- [85] P. D. B. Collins: *An Introduction to Regge Theorie & High Energy Physics*, Cambridge University Press, Cambridge 1977
- [86] V. N. Gribov: Sov. Phys. JETP 26 (1968) 414
- [87] M. Baker and K. A. Ter-Martirosyan: Phys. Rep. 28C (1976) 1
- [88] M. Ciafaloni, G. Marchesini and G. Veneziano: Nucl. Phys. B98 (1975) 472
- [89] J. Kwieciński: Z. Phys. C29 (1985) 147
- [90] V. Innocente, A. Capella and J. Trân Thanh Vân: Phys. Lett. B213 (1988) 81
- [91] R. Engel and J. Ranft: Hadron production in high-mass single-diffraction and central double-diffraction, to appear in Proceedings of the XXVI International Symposium

- on Multiparticle Dynamics, Faro, Portugal, 1996
- [92] A. B. Kaidalov, L. A. Ponomarev and K. A. Ter-Martirosyan: Sov. J. Nucl. Phys. 44 (1986) 468
  - [93] A. Capella and J. Kaplan: Phys. Lett. B52 (1974) 448
  - [94] V. A. Abramovski, V. N. Gribov and O. V. Kancheli: Sov. J. Nucl. Phys. 18 (1974) 308
  - [95] G. Veneziano: Nucl. Phys. B117 (1976) 519
  - [96] A. Capella, U. Sukhatme and J. Trân Thanh Vân: Z. Phys. C3 (1980) 329
  - [97] A. Capella, U. Sukhatme, C. I. Tan and J. Trân Thanh Vân: Z. Phys. C10 (1980) 249
  - [98] A. B. Kaidalov: Phys. Lett. B116 (1982) 459
  - [99] A. B. Kaidalov and K. A. Ter-Martirosyan: Phys. Lett. B117 (1982) 247
  - [100] S. Ritter and J. Ranft: Acta Phys. Polon. B11 (1980) 259
  - [101] B. L. Combridge, J. Kripfganz and J. Ranft: Phys. Lett. B70 (1977) 234
  - [102] D. W. Duke and J. F. Owens: Phys. Rev. D26 (1982) 1600
  - [103] M. Glück, E. Reya and A. Vogt: Phys. Rev. D46 (1992) 1973
  - [104] M. Glück, E. Reya and A. Vogt: Phys. Rev. D45 (1992) 3986
  - [105] M. Glück, E. Reya and A. Vogt: Z. Phys. C53 (1992) 127
  - [106] T. Sjöstrand: Comp. Phys. Commun. 39 (1986) 347
  - [107] T. Sjöstrand and M. Bengtsson: Comp. Phys. Commun. 43 (1987) 367
  - [108] I. F. Ginzburg and V. G. Serbo: Phys. Lett. 109B (1982) 231
  - [109] F. Borzumati and G. A. Schuler: Z. Phys. C58 (1993) 139
  - [110] P. Aurenche, J. P. Guillet, M. Fontannaz, Y. Shimizu and K. Kato: Prog. Theor. Phys. 92 (1994) 175
  - [111] M. Drees and R. M. Godbole: Phys. Rev. D50 (1994) 3124
  - [112] A. Capella, A. Kaidalov, C. Merino and J. Trân Thanh Vân: Phys. Lett. B337 (1994) 358
  - [113] H. Abramowicz, E. M. Levin, A. Levy and U. Maor: Phys. Lett. B269 (1991) 465
  - [114] B. Badelek and J. Kwieciński: Phys. Lett. B295 (1992) 263
  - [115] S. I. Alekhin et al.: Compilation of cross sections 4, CERN-HERA 87-01, 1987
  - [116] ZEUS Collab.: M. Derrick et al.: Z. Phys. C63 (1994) 391
  - [117] H1 Collab.: S. Aid et al.: Z. Phys. C69 (1995) 27
  - [118] H. Abramowicz, K. Charchula, M. Krawczyk, A. Levy and U. Maor: Int. J. Mod. Phys. A8 (1993) 1005
  - [119] E. Witten: Nucl. Phys. B120 (1977) 189
  - [120] H1 Collab.: S. Aid et al.: Nucl. Phys. B470 (1996) 3
  - [121] ZEUS Collab.: M. Derrick et al.: Measurement of the  $F_2$  structure function in deep inelastic  $e^+p$  scattering using 1994 data from the ZEUS detector at HERA, DESY-96-076, (hep-ex/9607002), 1996
  - [122] CTEQ-Collab.: H. L. Lai et al.: Phys. Rev. D55 (1997) 1280
  - [123] A. D. Martin, R. G. Roberts and W. J. Stirling: Phys. Lett. B387 (1996) 419
  - [124] H1 Collab.: T. Ahmed et al.: Nucl. Phys. B445 (1995) 195
  - [125] G. A. Schuler and T. Sjöstrand: Z. Phys. C68 (1995) 607
  - [126] H1 Collab.: S. Aid et al.: Z. Phys. C70 (1995) 17
  - [127] J. Kwieciński: Phys. Lett. B184 (1987) 386
  - [128] E. Segré: *Nuclei and particles*, Reading Mass, Benjamin, 1977

- [129] S. Y. Shmakov, V. V. Uzhinskii and A. M. Zadoroshny: *Comp. Phys. Commun.* 54 (1989) 125
- [130] J. Formánek: *Nucl. Phys.* B12 (1969) 441
- [131] L. P. A. Haakman, A. Kaidalov and J. H. Koch: *Phys. Lett.* B365 (1996) 411
- [132] B. Kopeliovich: *Soft Component of Hard Reactions and Nuclear Shadowing*, (hep-ph/9609385), in *Proceedings of the Workshop Hirscheegg'95: Dynamical Properties of Hadrons in Nuclear Matter*, Hirscheegg, 1995, ed. by H. Feldmeier and W. Nörenberg, Darmstadt, p. 102, 1996
- [133] E. A. Arakelyan et al.: *Phys. Lett.* 79B (1978) 143
- [134] G. R. Brookes et al.: *Phys. Rev.* D8 (1973) 2826
- [135] D. O. Caldwell et al.: *Phys. Rev.* D7 (1973) 1362
- [136] D. O. Caldwell et al.: *Phys. Rev. Lett.* 42 (1979) 553
- [137] New Muon Collab.: P. Amaudruz et al.: *Z. Phys.* C51 (1991) 387
- [138] New Muon Collab.: M. Arneodo et al.: *Nucl. Phys.* B441 (1995) 12
- [139] K. Geiger: *Phys. Rev.* D47 (1993) 133
- [140] B. Kopeliovich and B. Povh: *Z. Phys.* A356 (1997) 467
- [141] New Muon Collab.: M. Arneodo et al.: *Nucl. Phys.* B429 (1994) 503
- [142] J. W. Cronin et al.: *Phys. Rev.* D11 (1975) 3105
- [143] H.-J. Möhring, J. Ranft, A. Capella and J. Trân Thanh Vân: *Phys. Rev.* D47 (1993) 4146
- [144] H.-J. Möhring, J. Ranft, C. Merino and C. Pajares: *Phys. Rev.* D47 (1993) 4142
- [145] J. Ranft, A. Capella and J. Trân Thanh Vân: *Phys. Lett.* B320 (1994) 346
- [146] J. Ranft, A. Capella and J. Trân Thanh Vân: *Nucl. Phys.* A566 (1994) 511c
- [147] OMEGA Photon Collab.: R. J. Apsimon et al.: *Z. Phys.* C43 (1989) 63
- [148] W. A. Loomis et al.: *Phys. Rev.* D19 (1979) 2543
- [149] K. Braune et al.: *Z. Phys.* C17 (1983) 105
- [150] M. L. Cherry et al.: *Phys. Rev.* D50 (1994) 4272
- [151] WA80 Collab.: R. Albrecht et al.: *Z. Phys.* C47 (1990) 367
- [152] HELIOS Collab.: T. Åkesson et al.: *Z. Phys.* C46 (1990) 361
- [153] D. S. Barton et al.: *Phys. Rev.* D27 (1983) 2580
- [154] L. Hand et al.: *Acta Phys. Pol.* B 9 (1978) 1087
- [155] E665-Collab.: M. R. Adams et al.: *Z. Phys.* C61 (1994) 179
- [156] J. Babecki et al.: *Acta Physica Polonica* B9 (1978) 495
- [157] E665-Collab.: M. R. Adams et al.: *Phys. Rev.* D50 (1994) 1836
- [158] J. E. Elias et al.: *Phys. Rev.* D22 (1980) 13
- [159] D. L. Burke, H. L. Gustafson, L. W. Jones, M. J. Longo and R. E. Stockwell: *Phys. Rev.* D19 (1979) 1616
- [160] D. A. Garbutt et al.: *Phys. Lett.* 67B (1977) 355
- [161] D. Chaney et al.: *Phys. Rev.* D19 (1979) 3210
- [162] J. E. Huth et al.: *Towards a standardization of jet definitions*, preprint FERMILAB-Conf-90/249-E, in *Proceedings of the 1990 PDF Summer Study on High Energy Physics*, Snowmass, Colorado, 1990, ed. by E. L. Berger, World Scientific, Singapore, p. 134, 1992
- [163] A. Capella, A. Kaidalov, C. Merino and J. Trân Thanh Vân: *Phys. Lett.* B343 (1995) 403
- [164] UA8 Collab.: A. Brandt et al.: *Phys. Lett.* B297 (1992) 417

- [165] H1 Collab.: T. Ahmed et al.: Nucl. Phys. B435 (1995) 3
- [166] L. L. Frankfurt and M. I. Strikman: Nucl. Phys. B250 (1985) 143
- [167] B. Blättel, G. Baym, L. L. Frankfurt, H. Heiselberg and M. Strikman: Phys. Rev. D47 (1993) 2761
- [168] K. Goulianos: Phys. Rep. 101 (1983) 169
- [169] CHLM Collab.: M. G. Albrow et al.: Nucl. Phys. B108 (1976) 1
- [170] T. J. Chapin et al.: Phys. Rev. D31 (1985) 17
- [171] ABCDHW Collab.: A. Breakstone et al.: Nucl. Phys. B248 (1984) 253
- [172] NA22 Collab.: M. Adamus et al.: Z. Phys. C39 (1988) 301
- [173] G. Ingelman and P. E. Schlein: Phys. Lett. B152 (1985) 256
- [174] UA8 Collab.: R. Bonino et al.: Phys. Lett. B211 (1988) 239
- [175] CDF Collab.: P. L. Mélése et al.: Hard Diffraction at CDF, in Proceedings of the XIth Topical Workshop on  $p\bar{p}$  Collider Physics, Padova, Italy, 1996
- [176] ZEUS Collab.: M. Derrick et al.: Phys. Lett. B356 (1995) 129
- [177] A. Donnachie and P. V. Landshoff: Nucl. Phys. B244 (1984) 322
- [178] E. L. Berger, J. C. Collins, D. E. Soper and G. Sterman: Nucl. Phys. B286 (1987) 704
- [179] A. Donnachie and P. V. Landshoff: Phys. Lett. B191 (1987) 309
- [180] A. Donnachie and P. V. Landshoff: Nucl. Phys. B303 (1988) 634
- [181] N. N. Nikolaev and B. G. Zakharov: Z. Phys. C53 (1992) 331
- [182] G. Ingelman and K. Prytz: Z. Phys. C58 (1993) 285
- [183] J. Collins, L. Frankfurt and M. Strikman: Phys. Lett. B307 (1993) 161
- [184] B. Kniehl, H.-G. Kohrs and G. Kramer: Z. Phys. C65 (1995) 657
- [185] J. C. Collins, J. Huston, J. Pumplin, H. Weerts and J. J. Whitmore: Phys. Rev. D51 (1995) 3182
- [186] A. Capella, A. Kaidalov, C. Merino, D. Pertermann and J. Trân Thanh Vân: Phys. Rev. D53 (1996) 2309
- [187] T. Gehrmann and W. J. Stirling: Z. Phys. C70 (1996) 89
- [188] A. Devoto, D. W. Duke and J. F. Owens: Phys. Rev. D27 (1983) 508
- [189] P. Aurenche, R. Baier, M. Fontannaz, M. N. Kienzle-Focacci and M. Werlen: Phys. Lett. B233 (1989) 517
- [190] A. D. Martin, R. G. Roberts and W. J. Stirling: Phys. Lett. B306 (1993) 145
- [191] H. Plochow-Besch: Comp. Phys. Commun. 75 (1993) 396
- [192] H. U. Bengtsson: Comp. Phys. Commun. 31 (1984) 323
- [193] G. Battistoni, C. Bloise, C. Forti, M. Greco, J. Ranft and A. Tanzini: Astropart. Phys. 4 (1996) 351
- [194] J. Hüfner: Phys. Rep. 125 (1985) 129
- [195] S. Fredriksson, G. Eilam, G. Berlad and L. Bergström: Phys. Rep. 144 (1987) 187
- [196] L. Stodolsky: Formation Zone Description in Multiproduction, in Proceedings of the VIth International Colloquium on Multiparticle Reactions, Oxford, U.K., p. 577, 1975
- [197] L. Landau and I. Pomeranchuk: Dokl. Akad. Nauk SSR 92 (1953) 535
- [198] L. Landau and I. Pomeranchuk: Dokl. Akad. Nauk SSR 92 (1953) 735
- [199] J. Ranft: Phys. Rev. D37 (1988) 1842
- [200] A. Bialas: Z. Phys. C26 (1984) 301
- [201] K. Hänßgen and J. Ranft: Comp. Phys. Commun. 39 (1986) 37

- [202] B. G. Ritchie: Phys. Rev. C28 (1983) 926
- [203] J. Benecke, T. T. Chou, C. N. Yang and E. Yen: Phys. Rev. 188 (1969) 2159
- [204] I. Dostrovsky, Z. Fraenkel and G. Friedlander: Phys. Rev. 116 (1959) 683
- [205] R. Vandenbosh and J. R. Huizenga: *Nuclear Fission* Academic Press New York 1973
- [206] V. F. Weisskopf: Phys. Rev. 52 (1937) 295
- [207] N. Bohr and J. A. Wheeler: Phys. Rev. 56 (1939) 426
- [208] F. Atchison: preprint Jül-conf-34, in Proceedings of the Meeting on Targets for neutron beam spallation sources, KFA Jülich, Germany, ed. by G. Bauer, 1980
- [209] A. Ferrari and P. R. Sala: Physics of Showers induced by Accelerator Beams, Lecture given at the 1995 "Frederic Joliot" Summer School in Reactor Physics, Cadarache, France, 1995
- [210] A. Gilbert and A. G. W. Cameron: Can. J. Phys. 43 (1965) 1446
- [211] A. V. Ignatyuk, G. N. Smirenkin and A. S. Tishin: Sov. J. Nucl. Phys. 21 (1975) 255
- [212] A. V. Ignatyuk et al.: Sov. J. Nucl. Phys. 21 (1975) 612
- [213] E. Fermi: Prog. Theor. Phys. 5 (1950) 1570
- [214] M. Èpherre and E. Gradsztajn: J. Physique 18 (1967) 48
- [215] G. A. Bartholomew et al.: Advances in Nuclear Physics 7 (1975) 229
- [216] I. Bergqvist and N. Starfelt: Progress in Nuclear Physics 11 (1970) 1
- [217] D. H. Wilkinson: in Nuclear Spectroscopy B, ed. by F. Ajzenberg-Selove, Academic Press, New York, 1960
- [218] P. M. Endt: Atomic Data and Nuclear Data Tables 26 (1981) 46
- [219] W. Dilg, W. Schantl and H. Vonach: Nucl. Phys. A217 (1973) 269
- [220] K. Braune et al.: Z. Phys. C13 (1982) 191
- [221] E. Stenlund and I. Otterlund: Nucl. Phys. B198 (1982) 407
- [222] WA80 Collab.: R. Albrecht et al.: Z. Phys. C57 (1993) 37
- [223] Alma-Ata-Leningrad-Moscow-Tashkent Collab.: Sov. J. Nucl. Phys. 22 (1975) 380
- [224] L. Sihver et al.: Nucl. Phys. A543 (1992) 703
- [225] W. Heinrich et al.: Radiation Measurements 25 (1995) 203
- [226] E. Winkel: private communication, 1996
- [227] S. B. Kaufman et al.: Phys. Rev. C14 (1976) 1121
- [228] EMU01 Collab.: M. I. Adamovich et al.: Phys. Lett. B363 (1995) 230
- [229] EMU01 Collab.: M. I. Adamovich et al.: Phys. Lett. B262 (1991) 369
- [230] EMU01 Collab.: M. I. Adamovich et al.: Z. Phys. C65 (1995) 421
- [231] EMU01 Collab.: M. I. Adamovich et al.: Phys. Lett. B230 (1989) 175
- [232] KLM Collab.: A. Dabrowska et al.: Phys. Rev. D47 (1993) 1751
- [233] WA80 Collab.: R. Albrecht et al.: Phys. Lett. B307 (1993) 269
- [234] A. Baden et al.: Nucl. Instrum. Methods 203 (1982) 189
- [235] H. H. Gutbrod: private communication, 1996
- [236] N. T. Porile, G. T. Cole and C. Rudy: Phys. Rev. C19 (1979) 2288



---

## Acknowledgments

Many people contributed to the successful completion of this thesis.

First, I would like to express my deep gratitude to my supervisor Prof. Johannes Ranft. I will remember his encouragement, advice and support throughout each of my projects. I am very grateful to him for the time he spent on valuable discussions and for his steady interest in the progress of my work. Also, I wish to thank him for the hospitality during my stays in Genève, Annecy and Santiago de Compostela.

I am indebted to my supervisors Prof. F. W. Bopp and Prof. W. Heinrich for giving me the opportunity to work on this thesis at the University of Siegen. This work would not have been possible without their assistance and continuous support. I highly enjoyed many interesting and stimulating discussions.

Special thanks go to Ralph Engel. Numerous fruitful and crucial discussions with him inspired me tremendously. I appreciate his collaboration on parts of this work very much. I am grateful to Ralph for reading the manuscript with critical eyes.

I would like to acknowledge the collaboration with Dr. A. Ferrari and Dr. P. R. Sala on the description of slow particle production and with Dr. G. Battistoni and Dr. C. Forti on cosmic ray cascade calculations.

I am grateful to Prof. K. O'Brien and Dr. H. Schraube for discussions on different aspects of cosmic ray physics.

I enjoyed being a member of the Heavy-Ion-Group at the University of Siegen and would like to thank all my colleagues for the pleasant working atmosphere. Special thanks go to Dr. Erich Becker and Hermann Röcher for their continuous support on all aspects of computer hardware and system management.

I wish to thank Martin C. Hooper for correcting the English of parts of the text.

Finally, I am grateful to my parents for their encouragement and support.

This work was supported by a grant of the Bundesland Nordrhein-Westfalen and by the European Commission of the European Union DGXII unter contracts FI3P-CT92-0026 and CT95-0008.



---

## Curriculum Vitae

name: Stefan Roesler  
born: April 25, 1967 in Leipzig  
marital status: single  
nationality: German  
private address: Ludwigstr. 32, 57076 Siegen

1983-1985 education at high school  
1985 Abitur  
1985-1988 military service  
1988-1993 study of physics at Universität Leipzig  
1993 Diploma in physics  
supervisor: Prof. Dr. J. Ranft, Leipzig  
topic: Single diffractive processes within the two-  
component Dual Parton Model

1993-present PhD student at Universität–Gesamthochschule Siegen and Un-  
paid Associate at CERN, Genève, Switzerland